

SEARCH FOR GRAVITATIONAL WAVE SIGNALS ASSOCIATED WITH
GAMMA-RAY BURSTS DURING LIGO'S SECOND OBSERVING RUN

by

JORDAN ROBERT PALAMOS

A DISSERTATION

Presented to the Department of Physics
and the Graduate School of the University of Oregon
in partial fulfillment of the requirements
for the degree of
Doctor of Philosophy

September 2020

DISSERTATION APPROVAL PAGE

Student: Jordan Robert Palamos

Title: Search for Gravitational Wave Signals Associated With Gamma-ray Bursts
During LIGO's Second Observing Run

This dissertation has been accepted and approved in partial fulfillment of the requirements for the Doctor of Philosophy degree in the Department of Physics by:

Eric Torrence	Chair
Ray Frey	Advisor
Robert Schofield	Core Member
Michael Kellman	Institutional Representative

and

Kate Mondloch	Interim Vice Provost and Dean of the Graduate School
---------------	---

Original approval signatures are on file with the University of Oregon Graduate School.

Degree awarded September 2020

© 2020 Jordan Robert Palamos
This work is licensed under a Creative Commons
Attribution-NonCommercial-NoDerivs (United States) License.



DISSERTATION ABSTRACT

Jordan Robert Palamos

Doctor of Philosophy

Department of Physics

September 2020

Title: Search for Gravitational Wave Signals Associated With Gamma-ray Bursts During LIGO's Second Observing Run

The advanced LIGO and Virgo detectors have recently ushered in the age of gravitational wave astronomy. In this dissertation we briefly review how gravitational waves arise from general relativity, how they are produced, and how they are detected with LIGO. We also review the connection between gravitational waves and gamma-ray bursts, and review a method used to search for gravitational waves from gamma-ray triggers. A search for gravitational wave signals associated with gamma-ray bursts during the second observing run of advanced LIGO and Virgo is presented. Of the 98 bursts considered, no significant signals were found except for GW170817 which was found with a p -value of 3.1×10^{-4} . We report lower bounds on the distance to these gamma-ray bursts (GRBs), assuming various signal morphologies. We also describe the physical environment monitor system used at the LIGO observatories and present a new wide-band RF monitor for that system.

This dissertation contains previously published co-authored material.

CURRICULUM VITAE

NAME OF AUTHOR: Jordan Robert Palamos

GRADUATE AND UNDERGRADUATE SCHOOLS ATTENDED:

University of Oregon, Eugene, OR

University of San Francisco, San Francisco, CA

DEGREES AWARDED:

Doctor of Philosophy, Physics, 2020, University of Oregon

Bachelor of Science, Physics, 2012, University of San Francisco

AREAS OF SPECIAL INTEREST:

PROFESSIONAL EXPERIENCE:

Research Assistant, University of Oregon, 2014-present

Teaching Assistant, University Oregon, *various terms* 2013-2019

Physics and Astronomy Laboratory Technician, University of San Francisco,
2012-2013

GRANTS, AWARDS AND HONORS:

Special breakthrough prize in fundamental physics, for the observation of gravitational waves, opening new horizons in astronomy and physics, *as a member of the LIGO Scientific Collaboration*, 2016

PUBLICATIONS:

Abbott, Benjamin P and Abbott, R and Abbott, TD and Abraham, S and Acernese, F and Ackley, K and Adams, C and Adhikari, RX and Adya, VB and Affeldt, C and others (2019). Search for gravitational-wave signals associated with gamma-ray bursts during the second observing run of Advanced LIGO and Advanced Virgo. *The Astrophysical Journal*, 886.1 (2019): 75.

Abbott, B. P., Abbott, R., Abbott, T. D., Acernese, F., Ackley, K., Adams, C., ... Affeldt, C. (2017). Gravitational waves and gamma-rays from a binary neutron star merger: GW170817 and GRB 170817A. *The Astrophysical Journal Letters*, 848(2), L13.

Abbott, B. P., Abbott, R., Abbott, T. D., Abernathy, M. R., Acernese, F., Ackley, K., ... Adya, V. B. (2017). Search for gravitational waves associated with gamma-ray bursts during the first Advanced LIGO observing run and implications for the origin of GRB 150906B. *The Astrophysical Journal*, 841(2), 89.

Abbott, B. P., Abbott, R., Abbott, T. D., Abernathy, M. R., Acernese, F., Ackley, K., ... Adhikari, R. X. (2016). Characterization of transient noise in Advanced LIGO relevant to gravitational wave signal GW150914. *Classical and Quantum Gravity*, 33(13), 134001.

TABLE OF CONTENTS

Chapter		Page
I.	INTRODUCTION	1
II.	GRAVITATIONAL WAVES AND LIGO	5
	2.1. General Relativity	5
	2.1.1. Linearized Theory	7
	2.2. Production and Sources of gravitational waves (GWs)	12
	2.3. Astrophysical Sources	15
	2.3.1. compact coalescing binarys (CBCs)	15
	2.3.2. Bursts	17
	2.3.3. continuous wave (CW)	19
	2.3.4. Stochastic	19
	2.4. GW Detectors	20
	2.4.1. Advanced LIGO	21
	2.4.2. Antenna Response	23
	2.4.3. Noise sources	24
III.	GAMMA-RAY BURSTS	28
	3.1. Observations	28
	3.2. Progenitor Models	33

Chapter	Page
3.3. GRB 170817A	35
3.4. GRBs as Sources of Gravitational Waves	37
IV. SEARCH FOR GRAVITATIONAL WAVES ASSOCIATED WITH GAMMA RAY BURSTS	40
4.1. Signal detection preliminaries	40
4.2. X-Pipeline	44
4.2.1. Coherent Likelihood	45
4.2.2. Consistency tests	48
4.2.3. Data-quality Vetoes	50
4.2.4. Detection Procedure	51
4.2.5. Upper Limits and Tuning	54
4.3. O2 GRB Search	56
4.3.1. GRB Sample	57
4.3.2. Fermi	57
4.3.3. Swift	58
4.3.4. IPN	59
4.3.5. GRB Classification	63
4.3.6. Running the X-pipeline search on the Caltech computing cluster	63
4.3.7. Search Results	68
4.3.8. GRB 170817A	79
4.4. O3 GRBs	82
4.4.1. Improving the search by excising glitches from the data stream (gating)	82
4.4.2. Low Latency Online Search	87

Chapter	Page
V. PHYSICAL ENVIRONMENT MONITORING	94
5.1. PEM system overview and O1 installation	95
5.2. Description of the new RF scanner system	99
5.2.1. O1-O2 Radio Receiver	101
5.2.2. O1 swept-sine RF injection	105
5.2.3. O3 Radio Receiver	106
5.3. Glitch identification and mitigation	109
5.3.1. Example of 650 Hz wandering line	109
5.4. PEM event validation	112
5.4.1. GW150914 global environment checks	116
VI. CONCLUSION	121
REFERENCES CITED	124

LIST OF FIGURES

Figure	Page
2.1. The effect of a plane gravitational wave with period T on a ring of test particles for plus (top) and cross (bottom) polarization.	12
2.2. GW strain-amplitude from GW150914. The top panel shows the estimated gravitational wave strain amplitude from GW150914 in the Hanford detector, with an inset image of numerical relativity models of the black hole horizons during coalescence. The bottom panel shows the effective black hole separation in unites of Schwarzschild radii and effective relative velocity. Figure reproduced from [1]	16
2.3. aLIGO layout with suspensions	23
2.4. The antenna response of a LIGO interferometer to a gravitational wave. The patterns are oriented such that interferometer arms live in the xy ---plane and nodes in the left panel will occur at a 45° angle between the arms and every 90° around the z axis.	25
2.5. aLIGO noise curve	26
3.1. Example GRB Light Curves.	29
3.2. Hardness versus duration for BATSE GRBs.	32
3.3. Illustration of GRB mechanism.	33
3.4. Joint GRB lightcurves and GW strain signal from the joint mulit-messenger of GRB 170817A and GW170817. Figure reproduced from [2]	36
4.1. Data projected onto f_+ , f_\times space. The projection of a data sample from a three detector network. The green plane defines the space spanned by f_+ and f_\times . Figure reproduced from Sutton et al. [3]	45
4.2. Time-frequency map of the standard likelihood for GRB 170817, where the color indicates the log of the likelihood. The BNS signal can be faintly seen chirping upwards from 50 Hz to around 250 Hz ending a little after 4 seconds. Bright pixels not on this track are from instrumental noise.	48

Figure	Page
4.3. Incoherent null energy versus null energy for an example GRB analysis. Each cross represents a particular cluster colored according to its detection statistic value. Clusters that lie below the pink dashed line are discarded. The star corresponds to the loudest surviving cluster which can be found in Figure 4.2.	50
4.4. Event rates from the analysis of GRB 170817A	54
4.5. Fraction of injections recovered louder than most significant on-source event. In this example, 600 injections were used and the signal model was a circularly polarized sine-Gaussian with central frequency of $100Hz$ and a quality factor of 9. The precise 90% upper limit was obtained by interpolation.	55
4.6. Triangulation of a GRB with the IPN network.	60
4.7. Cumulative distribution of p -values from the unmodeled search for transient GWs associated with 97 GRBs. GRB 170817A was removed. The dashed line represents the expected distribution under the no-signal hypothesis, with dotted lines indicating a 2σ deviation from this distribution. These results are consistent with the no-signal hypothesis, and have a combined p -value of 0.75 as calculated by a weighted binomial test [4, 5].	69
4.8. Cumulative histograms of the 90% confidence exclusion distances D_{90} for accretion disk instability signal model A [6, 7] and circular sine-Gaussian 150 Hz [8] model. For a given GRB and signal model this is the distance within which 90% of simulated signals inserted into off-source data are successfully recovered with a significance greater than the loudest on-source trigger. The median values for ADI-A and CSG-150 waveforms are 32 Mpc and 81 Mpc respectively.	70
4.9. New time-frequency map of the detection statistic for GRB 170817. . . .	80
4.10. Old time-frequency map of the detection statistic for GRB 170817. Pixels below the threshold have been set to white. Clusters are made by combining each pixel with any surrounding eight pixels. The loudest cluster consists of 9 pixels between 70 Hz and 80 Hz at $t = 0$	81
4.11. Time-frequency representation of the GW170817 signal from Livingston. The raw data is shown in the top panel and a large instrumental glitch is easily visible on top of the BNS signal track. The BNS coalescence falls at 0.4 s in this figure, and the glitch occurs 1.1 s before that time. The bottom panel shows the time domain data, where the glitch was	

Figure	Page
modelled so that it could be subtracted. Figure reproduced from Abbott et al. [9].	84
4.12. Time-frequency representations of two glitches from the analysis of GRB 170402. When these glitches were removed using the gating method, the recovery of injected signals with X-pipeline was improved.	86
4.13. Detection efficiency curves for ADI-D waveforms in the X-pipeline analysis of GRB 170402. The left panel shows the analysis before gating two glitches in the Hanford data, the presence of these glitches caused many injections to be rejected by coherency requirements. When the data around those glitches are zeroed out, the injections can again be recovered by the pipeline	87
4.14. Schematic of the medium latency GRB codes	90
4.15. Screenshot of medium latency test results.	93
5.1. Map showing the location of physical environment monitor sensors at the Hanford observatory. Accessed from http://pem.ligo.org/	96
5.2. The author installing an accelerometer on a vacuum chamber at LIGO-Hanford.	97
5.3. PEM injection at 45 MHz.	99
5.4. Block diagram of the RF scanner system.	101
5.5. Annotated spectra of RF activity at the LIGO-Hanford site on August 4, 2016 from 600 MHz to 1 GHz. Shown is frequency in Hz versus dBm at the radio receiver. The top and bottom panels correspond to different cellular phones in use at the time each spectrum was captured. The annotations describe the type of signal corresponding to peaks in the spectrum: peaks circled in green are from broadcast television signals, orange and yellow are from common cellular phone signals (although not the particular phones being used to test the system), the peaks highlighted in black are unknown, and red and blue circles indicate the cellular signals intentionally used during this test.	104
5.6. Swept sine RF injection. Time versus frequency plot of spectral data from the radio receiver. The start time is given in GPS time and corresponds to Oct 10 17:01:16 UTC. The color axis indicates power measured at the RF receiver in dB, normalized to the median.	106

Figure	Page
5.7. RF spectrum from the system used for the O3 run. Frequency in Hz versus time in seconds. The time axis spans 10 minutes and the start time corresponds to February 17, 2020 at 22:40:00 UTC. The frequency spans from DC to 1 GHz. Prominent steady lines in the spectrum correspond to things like FM radio and TV broadcasts.	107
5.8. Frequency versus significance for an X-pipeline analysis showing 650 Hz noise. The red crosses correspond to “dummy on-source” triggers, as described in the previous chapter, and show an abundance of significant triggers with a central frequency of 650 Hz, indicating the possibility of excess instrumental noise at that frequency.	110
5.9. aLIGO strain spectrum before and after 650 Hz line mitigation. The blue trace shows the spectrum before the fix, and has a peak near 650 Hz and that sticks up above the orange trace.	111
5.10. Omegascan of DARM and the most significant PEM channel during GW151226. Shown on the left is the omegascan of a magnetometer located at an electronics rack at the ‘end Y’ arm of the interferometer. On the right is the Hanford DARM signal.	113

LIST OF TABLES

Table	Page
4.1. GRBs localized with timing data from the IPN during O2. Of the following IPN localizations eight of them were used for a GRB analysis with X-pipeline and reported in [10]. Many of these localizations were not used because, the error region was too large, did not improve over the Fermi or Swift localization previously available, or the region was too irregularly shaped.	61
4.2. Median 90% confidence level exclusion distances, D_{90} , for the searches during the second observing run of Advanced LIGO and Advanced Virgo (O2). Modeled search results are shown for three classes of neutron star (NS) binary progenitor model, and unmodeled search results are shown for circular sine-Gaussian (CSG) [8] and accretion disk instability (ADI) [6, 7] models.	71
4.3. Information and limits on associated GW emission for each of the analyzed GRBs. The Satellite column lists the instrument whose sky localization was used for the purposes of analysis. The Network column lists the GW detector network used in the analysis of each GRB – H1 = LIGO Hanford, L1 = LIGO Livingston, V1 = Virgo. A [†] denotes cases in which the on-source window of the generic transient search is extended to cover the GRB duration ($T_{90} > 60$ s). In cases where each analysis used a different network, parentheses indicate the network used for PyGRB analysis, and detail is provided in the table footnotes. Columns 8–12 display the 90% confidence exclusion distances to the GRB (D_{90}) for several emission scenarios: BNS, generic and aligned spin neutron star-black hole (NS-BH), ADI-A, and CSG GW burst at 150 Hz with total radiated energy $E_{\text{GW}} = 10^{-2} M_{\odot} c^2$	72
5.1. Hardware used in the RF scanner system.	102
5.2. Hanford PEM channels triggered during GW151226. SNR refers to the value calculated by the Omega pipeline at time time of the GW event. ‘SNR to show’ column uses a measured coupling factor to give the SNR value at which the environmental disturbance starts induce a visible signal in DARM. ‘SNR required’ is how much SNR the PEM channel needs if environmental coupling from that sensor were to account for the signal in DARM, and the ratio in the last column describes how much bigger the PEM signal would need to be before the DARM signal could be accounted for through environmental coupling.	115

Table	Page
5.3. Global electromagnetic observations gathered at the time of GW150814. None of these observations have shown any anomalous electromagnetic events that could have affected the GW data. The full report can be found in [11].	119

CHAPTER I

INTRODUCTION

On August 17, 2017 gamma-rays and gravitational waves (GWs) were observed from a coalescing binary neutron star system in the galaxy NGC 4993. This event fulfilled the decades long promise of using joint observations from both electromagnetic and gravitational wave facilities to learn more about the universe than would be possible by either on their own. That is the promise of multi-messenger astronomy which uses measurements across all fundamental forces to explore the universe. The ability to use the gravitational force as a messenger is a recent development in astronomy that has been a century in the making.

The first step towards GW astronomy was a theoretical insight into the nature of gravity given by Albert Einstein in 1915 with his theory of general relativity [12]. In Einstein's theory, the force we experience as gravity arises from the curvature of space and time in the presence of matter. This theory was a profound conceptual revolution and offered many testable predictions that were later verified experimentally. These predictions ranged from precise corrections to orbital dynamics in the solar system, to the bending of light by massive objects, to the existence of black holes and GWs—which are ripples of curvature in spacetime that propagate through otherwise empty space at the speed of light.

Early on, there was not consensus within the physics community about the existence of GWs: Einstein himself appears to have thought that waves in general relativity were a mathematical relic that could not transmit energy or be detected in practice, although he was convinced otherwise by contemporaries. One thing, however, was clear: if GWs were to exist they would manifest as extremely small

effects on earth that would be almost impossible to merely detect—much less used as a tool for doing astronomy. For that reason, even after most theoreticians had become convinced of the physical nature of GWs (a simple ”sticky bead” argument [13] attributed to Richard Feynman in 1957 ultimately ended any debate about whether GWs could actually carry energy) it took many decades longer to detect them experimentally.

Early efforts to build a GW detector—most famously by Joseph Weber who pioneered resonant mass detectors in the 1960s [14]—never reached the required sensitivity. Although Weber’s claims of detecting GWs have not stood up, his courage laid the groundwork for later successes. Very strong evidence for GWs was discovered in 1981 when Russel Hulse and Joseph Taylor published their analysis of the binary pulsar PSR B1913+16 showing an orbital decay perfectly matching the prediction due to energy loss from the system emitting GWs [15]. Another claim of indirect detection was put forward in 2014 from observations the polarization of the cosmic microwave background, although that was retracted later that same year [16]. It wasn’t until largest experiment ever funded by the NSF turned on their second generation of detectors that GWs were finally detected.

The feat was accomplished on September 14, 2015 by the Laser Interferometer Gravitational-wave Observatory (LIGO) collaboration which used kilometer-scale laser interferometers to detect the GW signature of merging black holes [1]. That moment earned the 2017 Nobel prize in physics for Barry Barish, Kip Thorne, and Rai Weiss for “*decisive contributions to the LIGO detector and the observation of gravitational waves*” and has aptly been compared to the moment when Galileo trained a telescope skyward in 1609: a comparison that highlights the role new technologies play in revealing fundamental truths about the cosmos and our place

in it. Already, the current generation of GW detectors are catching tens of binary black hole mergers per year [17] which raises fundamental questions about the origin of these objects.

Furthermore, electromagnetic telescopes—spiritual successors to Galileo’s 1609 telescope—have observed a binary neutron star merger in concert with GW observations which together have confirmed basic facts about the universe such as the speed of gravity and how heavy metals were synthesized. These observations also placed independent constraints on the Hubble constant, H_0 , which given the tension between values derived from other methods used to calculate H_0 may eventually lead to evidence of new physics beyond the standard Lambda-CDM model of cosmology. This is all to say that the nascent field of gravitational wave astronomy, and multi-messenger astronomy using gravitational waves, has already provided important discoveries with more discoveries sure to accompany future joint detections.

This dissertation addresses contributions made to the field of GW detection and multi-messenger astronomy. It primarily contains work done as a member of the LIGO scientific collaboration to search for GWs associated with GRBs. Chapter II contains background about how GW arise from general relativity, how they are produced in an astrophysical scenario, and the method used to detect them with LIGO. Chapter III reviews the phenomena of GRBs which have an interesting history in their own right and explores the connection between GRBs and GWs. The original work contained in Chapter IV includes a search for GWs associated with GRBs during LIGO’s second observing run, an analysis that I led and was published by the LIGO and Virgo collaborations [10]. That chapter contains relevant background information about methods used to detect GWs in

the presence of instrumental noise and goes on to present the search procedure. It includes an extended discussion about the GRB 170817A search, which turns out to be the first real signal GW signal to be analyzed with this method.

The history of GW detection, briefly discussed above, reminds us how difficult it is to detect such a minute effect and highlights the importance of having a thorough understand of the measurement device and background. For GW detectors on earth, environmental noise can easily pollute the astronomical data which makes knowledge of the physical environment around GW detectors an important part of gravitational wave physics. Therefore, Chapter V discusses my own contribution to this effort within LIGO: that chapter covers environmental noise coupling in LIGO and contains original work done to develop a new environmental sensor for monitoring the radio background at the LIGO observatories. Finally, Chapter VI contains a brief summary and concluding remarks.

CHAPTER II

GRAVITATIONAL WAVES AND LIGO

On September 14, 2015 the LIGO detectors recorded the gravitational wave signature of merging black holes [1]. This marked the first direct detection of gravitational waves and ended a decades long effort by hundreds of scientists to find them, nearly a hundred years after gravitational waves were predicted by Albert Einstein and his theory of general relativity. At the same time it marked the beginning of the field of gravitational wave astronomy, which has given scientists an entirely new way of observing the universe. In this chapter I review how gravitational waves arise from Einstein's relativity, how they can be generated, and how they are detected. This chapter provides a brief overview of general relativity as it is relevant to the work done in later chapters. Still, it barely scratches the surface and a more complete description of general relativity can be found in many classic references including Misner et al. [18], Carroll [19], Hartle [20], which were consulted during this writing.

2.1. General Relativity

Einstein's theory of general relativity asserts that gravity arises from the geometry of curved spacetime. This theory is, conceptually, very different from its predecessor, Newton's law of universal gravitation, which had for the most part successfully described the gravitational interaction on earth and in the solar system for over a century. Nevertheless, general relativity offers precisely testable predictions and has gone on to become one of the most precisely tested theories in science.

In the Newtonian picture, a mass distribution ρ creates a gravitational field Φ

$$\nabla^2\Phi = 4\pi G\rho$$

which results in a force felt by massive particles

$$\vec{F} = -m\vec{\nabla}\Phi.$$

Trajectories are then calculated using Newton's law of motion.

In Einstein's picture, matter curves spacetime according to the Einstein field equations [12]

$$G_{\alpha\beta} = 8\pi GT_{\alpha\beta}. \tag{2.1}$$

Matter particles then follow geodesics in this curved geometry:

$$\frac{d^2x^\alpha}{dt^2} = -\Gamma_{\mu\nu}^\alpha \frac{dx^\mu}{dt} \frac{dx^\nu}{dt} \tag{2.2}$$

where (2.2) is the geodesic equation and the coefficients $\Gamma_{\mu\nu}^\alpha$, known as Christoffel symbols, are defined in terms of the metric and its derivatives as

$$g_{\alpha\delta}\Gamma_{\beta\gamma}^\delta = \frac{1}{2} \left(\frac{\partial g_{\alpha\beta}}{\partial x^\gamma} + \frac{\partial g_{\alpha\gamma}}{\partial x^\beta} - \frac{\partial g_{\beta\gamma}}{\partial x^\alpha} \right).$$

The metric tensor (or just *metric*), $g_{\alpha\beta}$, is the fundamental mathematical object which captures the geometric nature of spacetime and provides the notion of a line element in some coordinate system $\{x_\alpha\}$ as

$$ds^2(x) = g_{\alpha\beta}(x)dx^\alpha dx^\beta.$$

The relationship between spacetime curvature and matter energy density is given to us in Einstein's equation (2.1) which has been written in natural units (ignoring a cosmological constant). The $G_{\alpha\beta}$ term on the left hand side of Einstein's equation is known as the Einstein tensor and depends entirely on the metric, $g_{\alpha\beta}$, which determines the curvature of spacetime. On the right hand side, $T_{\alpha\beta}$ is commonly known as the *stress-energy tensor* which defines any matter energy that may be present. The proportionality constant can be determined by requiring that Newtonian gravity is recovered in the weak field, slow motion regime.

The Einstein field equations, however, are extremely difficult to solve. They relate 4x4 symmetric tensors, which means they can be considered a system of ten coupled nonlinear partial differential equations. Usually, solutions are found with the aid of symmetries, in the weak field limit, or with numerical methods. The existence of gravitational waves can be seen under the assumptions of linearized gravity, where curvature is introduced as a small perturbation to a flat background as I will show in the following section.

2.1.1. Linearized Theory

The LHS of the Einstein field equations is commonly written as

$$G_{\alpha\beta} = R_{\alpha\beta} - \frac{1}{2}g_{\alpha\beta}R \quad (2.3)$$

where $R_{\alpha\beta}$ is known as the Ricci tensor and R as the Ricci scalar. The Ricci tensor depends on the metric through the connection

$$R_{\alpha\beta} = \frac{\partial\Gamma_{\alpha\beta}^{\gamma}}{\partial x^{\gamma}} - \frac{\partial\Gamma_{\alpha\gamma}^{\beta}}{\partial x^{\gamma}} + \Gamma_{\alpha\beta}^{\gamma}\Gamma_{\gamma\delta}^{\delta} - \Gamma_{\alpha\delta}^{\gamma}\Gamma_{\beta\gamma}^{\delta}$$

and the Ricci scalar is the contraction $R = g^{\alpha\beta} R_{\alpha\beta}$.

In order to get some traction dealing with these complicated objects, one can take the spacetime metric $g_{\alpha\beta}$ to be the flat Minkowski metric $\eta_{\alpha\beta}$ plus a small perturbation $h_{\alpha\beta}$

$$g_{\alpha\beta} = \eta_{\alpha\beta} + h_{\alpha\beta}$$

and discard higher powers of $h_{\alpha\beta}$ that show up in subsequent equations. To first order in h the Christoffel symbols become

$$\Gamma_{\alpha\beta}^{\gamma} = \frac{1}{2}\eta^{\gamma\delta}\left(\frac{\partial h_{\alpha\delta}}{\partial x^{\beta}} + \frac{\partial h_{\beta\delta}}{\partial x^{\alpha}} - \frac{\partial h_{\alpha\beta}}{\partial x^{\delta}}\right).$$

We can insert that into the expression above for the Ricci tensor and after some cancellations arrive at

$$R_{\alpha\beta} = \frac{1}{2}\left(\frac{\partial^2 h_{\beta}^{\gamma}}{\partial x^{\gamma}\partial x^{\alpha}} - \eta^{\gamma\delta}\frac{\partial^2 h_{\alpha\beta}}{\partial x^{\gamma}\partial x^{\delta}} - \frac{\partial^2 h_{\gamma}^{\alpha}}{\partial x^{\beta}\partial x^{\alpha}} + \frac{\partial^2 h_{\alpha}^{\gamma}}{\partial x^{\beta}\partial x^{\gamma}}\right).$$

The Ricci scalar can be calculated from $R = g^{\alpha\beta} R_{\alpha\beta} = \eta^{\alpha\beta} R_{\alpha\beta} + O(h^2)$

$$R = \frac{\partial^2 h^{\alpha\beta}}{\partial x^{\alpha}\partial x^{\beta}} - \eta^{\alpha\beta}\frac{\partial^2 h_{\gamma}^{\alpha}}{\partial x^{\alpha}\partial x^{\beta}}.$$

With the linearized Ricci tensor and scalar in hand, we can compute the linearized Einstein tensor using equation 2.3:

$$G_{\alpha\beta} = \frac{1}{2}\left(\frac{\partial^2 h_{\beta}^{\gamma}}{\partial x^{\gamma}\partial x^{\alpha}} - \eta^{\gamma\delta}\frac{\partial^2 h_{\alpha\beta}}{\partial x^{\gamma}\partial x^{\delta}} - \frac{\partial^2 h}{\partial x^{\beta}\partial x^{\alpha}} + \frac{\partial^2 h_{\alpha}^{\gamma}}{\partial x^{\beta}\partial x^{\gamma}}\right) - \frac{1}{2}\eta_{\alpha\beta}\left(\frac{\partial^2 h^{\alpha\beta}}{\partial x^{\alpha}\partial x^{\beta}} - \eta^{\alpha\beta}\frac{\partial^2 h}{\partial x^{\alpha}\partial x^{\beta}}\right).$$

The expression can be simplified by making a clever substitution

$$\bar{h}_{\alpha\beta} := h_{\alpha\beta} - \frac{1}{2}\eta_{\alpha\beta}h,$$

where $\bar{h}_{\alpha\beta}$ is known as the trace-reversed metric perturbation since $\bar{h} = \eta^{\alpha\beta}\bar{h}_{\alpha\beta} = -h$. This way, the linearized Einstein tensor becomes

$$G_{\alpha\beta} = \frac{1}{2}\left(\frac{\partial^2\bar{h}_\beta^\gamma}{\partial x^\gamma\partial x^\alpha} - \eta^{\gamma\delta}\frac{\partial^2\bar{h}_{\alpha\beta}}{\partial x^\gamma\partial x^\delta} - \eta_{\alpha\beta}\frac{\partial^2\bar{h}^{\gamma\delta}}{\partial x^\gamma\partial x^\delta} + \frac{\partial^2\bar{h}_\alpha^\gamma}{\partial x^\beta\partial x^\gamma}\right)$$

which we can use to write the linearized Einstein field equations as

$$\frac{\partial^2\bar{h}_\beta^\gamma}{\partial x^\gamma\partial x^\alpha} - \eta^{\gamma\delta}\frac{\partial^2\bar{h}_{\alpha\beta}}{\partial x^\gamma\partial x^\delta} - \eta_{\alpha\beta}\frac{\partial^2\bar{h}^{\gamma\delta}}{\partial x^\gamma\partial x^\delta} + \frac{\partial^2\bar{h}_\alpha^\gamma}{\partial x^\beta\partial x^\gamma} = 16\pi GT_{\alpha\beta}.$$

Further simplification will come from careful choice of coordinates.

Analogously to the procedure in electromagnetism, we impose a gauge condition on the metric perturbation

$$\frac{\partial\bar{h}^{\alpha\beta}}{\partial x^\beta} = 0. \tag{2.4}$$

Equation 2.4 defines the *Lorenz gauge* and in that gauge the linearized Einstein equation takes the simple form:

$$-\square\bar{h}_{\alpha\beta} = 16\pi GT_{\alpha\beta} \tag{2.5}$$

where \square is flat-space wave operator (or d'Alembertian) and $\square\bar{h}_{\alpha\beta} = \eta^{\gamma\delta}\frac{\partial^2\bar{h}_{\alpha\beta}}{\partial x^\gamma\partial x^\delta}$ since mixed derivatives do not appear for the Minkowski metric. Equation 2.5 shows that the linearized Einstein field equations in the Lorenz gauge reduce to

a wave equation for the perturbation with the stress-energy tensor as a source:
gravitational waves!

To examine some basic properties of these gravitational waves, let us consider equation 2.5 in vacuum

$$-\square \bar{h}_{\alpha\beta} = 0 \tag{2.6}$$

which has plane wave solutions of the form $\bar{h}_{\alpha\beta} = A_{\alpha\beta} e^{ik_\gamma x^\gamma}$ where $A_{\alpha\beta}$ is known as the polarization tensor and k_γ the wave vector. For this basic solution to solve (2.6) the wave vector must satisfy

$$k_\gamma k^\gamma = 0.$$

This means, in the language of general relativity, that k_γ is a null vector and implies that gravitational waves travel at the speed of light.

Due to the Lorenz gauge condition (2.4) the constant $A_{\alpha\beta}$ must satisfy

$$A^{\alpha\beta} k_\beta = 0. \tag{2.7}$$

The tensor $A^{\alpha\beta}$ originally had ten independent components, since it is a symmetric 4×4 tensor. The condition 2.7 (which is equivalent to four equations) reduces that to six independent components. However, there is yet more coordinate freedom to exploit: arbitrary coordinate transformations of the form

$$x'^\alpha = x^\alpha + \xi^\alpha(x)$$

are still allowed provided ξ^α respects (2.4) which implies

$$\square \xi_\alpha = 0.$$

This amounts to four extra conditions which means the metric perturbation only has 2 remaining independent degrees of freedom. These final gauge conditions can be chosen in order impose the following constraints:

$$A_{\alpha\beta}x^\beta = 0$$

$$A_\alpha^\alpha = 0$$

which specify the so-called *transverse traceless* gauge (TT). As the name implies, when working in this gauge the polarization tensor is traceless and all non-zero terms are in the transverse direction. Therefore, if we were to assume a plane gravitational wave propagating in the z -direction and write the polarization tensor in matrix form it would look like:

$$\begin{pmatrix} 0 & 0 & 0 & 0 \\ 0 & A_{11} & A_{12} & 0 \\ 0 & A_{12} & -A_{11} & 0 \\ 0 & 0 & 0 & 0 \end{pmatrix}.$$

These two independent polarizations are commonly referred to as the “plus” and “cross” polarizations of gravitational radiation. To understand the what the observable consequences of these polarizations are, consider the simple case of a ring of test particles in the xy -plane. A gravitational wave in the plus polarization traveling in the z -direction will alternately stretch and compress space in the x and y directions as shown in figure 2.1. The cross polarization has a similar effect but rotated by 45° .

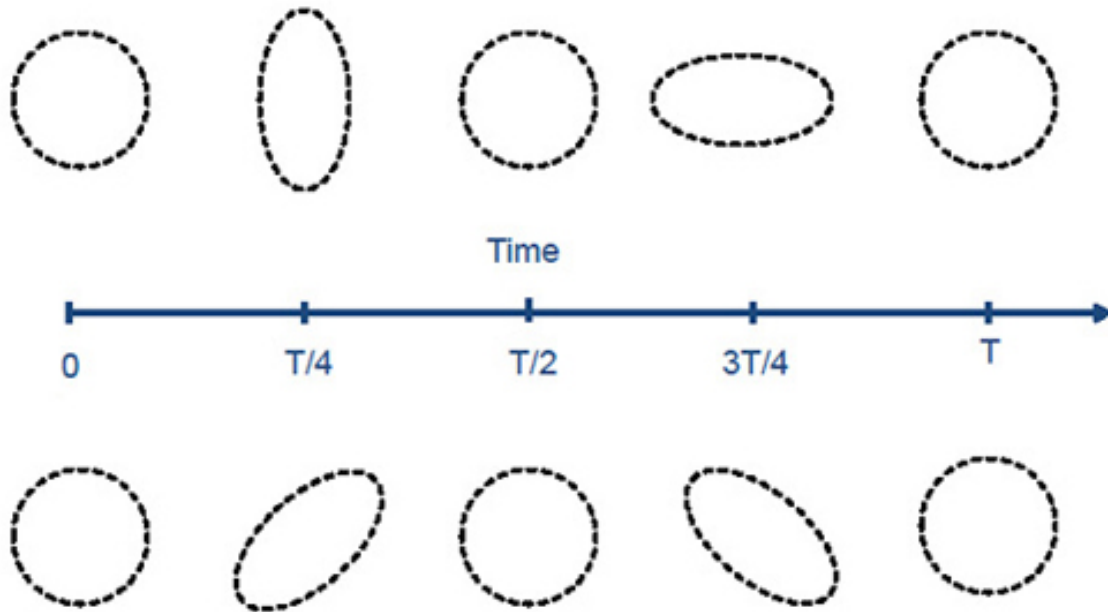


FIGURE 2.1. The effect of a plane gravitational wave with period T on a ring of test particles for plus (top) and cross (bottom) polarization.

We have shown how the existence of gravitational waves emerges from the Einstein field equations under the assumptions of linearized gravity and the basic effect of these waves which will be important when thinking about trying to detect these things. But first, I will quickly discuss how these waves can be produced.

2.2. Production and Sources of GWs

In this section we will consider how gravitational waves may be produced by astrophysical sources. In order to quickly get to an important result I will summarize an argument from Misner et al. [18] which makes an analogy between gravitational and electromagnetic radiation.

The power radiated in gravitational waves can be roughly estimated in analogy to electromagnetic radiation if one substitutes the electric charge e with the mass in the source term. The dominant term for electromagnetic radiation

is the dipole: power radiated by a source with dipole moment p is proportional to \ddot{p}^2 . The analogous term for gravitation would be a “mass dipole” moment which is $p_{mass} = \sum_n m_n x_n$. The first derivative of this quantity is the total linear momentum. Therefore, due to the conservation of momentum, the second derivative of this is zero so the dipole term cannot contribute to gravitational radiation. The next term in the electromagnetic case corresponds to the magnetic dipole. The gravitational analog to the magnetic dipole is the angular momentum which is also conserved and therefore also does not contribute to the radiated power. The electric quadrupole radiates with power

$$P_{EM} \sim \ddot{Q}_{ij} \ddot{Q}_{ij}$$

where Q_{ij} is the electric quadrupole tensor and summation is implied over the latin indicies. This time, there is no reason for the mass quadrupole to be conserved and we are led to conclude that power radiated in gravitational waves depends on the changing quadrupole moment of the source!

One can actually solve the linearized Einstein field equations with a source using the method of Green’s functions (again, similar to the electromagnetic case). When the source is moving slowly and the field is evaluated in the far field regime, the perturbation in the TT gauge turns out to be [20]

$$h_{ij}^{TT}(t, x) \simeq \frac{2G}{c^4 r} \ddot{I}_{ij}^{TT}(t - r/c) \tag{2.8}$$

where the quadrupole tensor, $I_{ij}^{TT}(t)$ is defined as:

$$I^{ij}(t) = \int x^i x^j \rho(t - r/c, x) d^3x.$$

Since the GW strain depends on a changing quadrupole moment, it is implied that no gravitational radiation can be produced, for example, by spherically symmetric expansion or axially symmetric rotation.

Using equation 2.8 for h_{ij}^{TT} we can work out an order of magnitude estimate for the strength of a GW following an argument put forward by Schutz [21]. For motion inside a highly non-spherical source, the typical component of \ddot{I}_{ij} can be approximated as

$$\ddot{I} = Mv_{\text{N.S.}}^2.$$

where $v_{\text{N.S.}}$ refers to the non-spherical part of the velocity inside the source. By the virial theorem

$$v_{\text{N.S.}} \sim \frac{GM}{2R}$$

where R is the size of the source. So the equation for the strength of a gravitational wave becomes

$$h \sim \frac{GM}{rc^2} \frac{GM}{Rc^2}.$$

Interestingly, the first term looks like the Newtonian potential of the source far away and the second term looks like the Newtonian gravitational potential at the source. If we take the parameters of the binary pulsar PSR B1913+16 (which is famous from the 1993 Nobel Prize won by Hulse and Taylor), we end up with an approximate amplitude of

$$h \sim \frac{G (2.8 m_{\odot})}{(8 \text{ kpc}) c^2} \frac{G (2.8 m_{\odot})}{(4.8 R_{\odot}) c^2} \sim 2 \times 10^{-23}.$$

While this is a rough approximation it nevertheless gives an accurate sense for the incredible level of sensitivity necessary to detect a gravitational wave on earth

(although the real signal from PSR B1913+16 lies outside of the sensitive frequency range of ground based GW detectors).

2.3. Astrophysical Sources

We now turn our attention to astrophysical sources of gravitational waves. In the context of ground based laser interferometry, which is the primary method I will discuss for detecting GWs, sources are usually divided into the following four categories: compact binary coalescences (CBCs), bursts, continuous waves (CWs), and stochastic signals.

2.3.1. CBCs

CBCs refer to compact objects such as neutron stars or black holes which lose orbital energy to gravitational waves as they spiral-in and eventually merge. The first detection, GW150914; the binary neutron star signal, GW170817; and in fact all GW events published in the first gravitational wave transient catalog, GWTC-1 [17], belong to this source class. Gravitational waveforms from CBC sources can be accurately modeled from post-Newtonian theory and simulations using numerical relativity. For example, the waveform from the first detection is shown in Figure 2.2. Accurate modeling of CBC waveforms enables the usage of the matched-filter technique for signal detection [22, 23, 24], which allows the recovery of weaker signals in the presence of detector noise.

Having a well-modelled source also opens the door to many other interesting scientific possibilities. For example, the frequency evolution of inspiraling masses

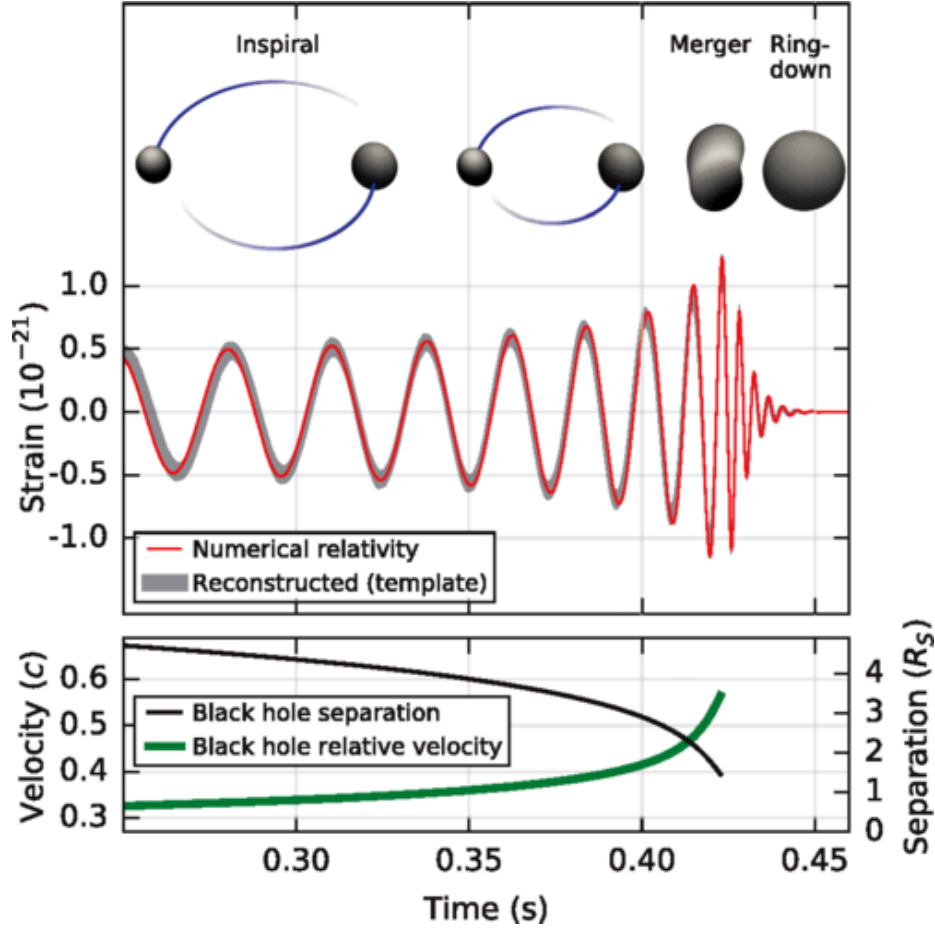


FIGURE 2.2. GW strain-amplitude from GW150914. The top panel shows the estimated gravitational wave strain amplitude from GW150914 in the Hanford detector, with an inset image of numerical relativity models of the black hole horizons during coalescence. The bottom panel shows the effective black hole separation in unites of Schwarzschild radii and effective relative velocity. Figure reproduced from [1]

depends entirely on the chirp mass [25]

$$\mathcal{M} = \frac{(m_1 m_2)^{3/5}}{(m_1 + m_2)^{1/5}} = \frac{c^3}{G} \left[\frac{5}{96} \pi^{-8/3} f^{-11/3} \dot{f} \right]^{3/5}$$

where m_1 and m_2 are the masses of each object and f is the frequency. By measuring the frequency evolution of such a system, one can infer the mass scale and therefore the intrinsic luminosity, which enables independent distance

measurements. A more sophisticated version of this general principle was used in the case of GW170817, which had an electromagnetic counterpart, to measure the Hubble constant, H_0 [26]. The result from this analysis was $70.0_{-8.0}^{+12.0}$ km s⁻¹ Mpc⁻¹ which is consistent with existing measurements.

The mergers of black holes or neutron stars can also be used to probe fundamental physics. Tests of general relativity in the strong field regime can be carried out by comparing the measured signal from CBC mergers to simulations from numerical relativity. So far, GR has passed all these tests with flying colors [27, 28]! Also, the gravitational waveform from binaries containing neutron stars is used to constrain the neutron star equation of state [29].

Finally, with many BBH signals detected and more on the way, we are beginning to learn about the population of stellar mass black holes in the universe. The merger rate of binary black holes has recently been estimated to be $R_{BBH} = 53.2_{-28.8}^{+58.5}$ Gpc⁻³yr⁻¹ [30] and studies are ongoing to explain how these objects arise in the context of normal stellar evolution—or determine if new models are needed to explain their origin.

2.3.2. Bursts

As opposed to CBC signals where we have an accurate model of the gravitational waveform, the other class of transient gravitational wave signals are commonly referred to as gravitational wave bursts (GWBs)—or simply *bursts*. Possible astrophysical scenarios that could give rise to bursts of gravitational radiation include things like the gravitational collapse of massive stars [31] or the hyperbolic encounters of compact objects [32]. Searches have been carried out under the burst umbrella for GWs from a diverse range of phenomena ranging from

pulsar glitches [33] to cosmic string cusps [34]. In fact, searches for burst signals are designed to be capable of detecting unanticipated sources. These searches typically search for excess power relative to background noise that is coherent across a network of gravitational wave detectors.

To get a rough sense of the scale of a generic GW burst at a detector on earth, consider the commonly used metric for burst amplitude, the root-sum-squared strain (h_{rss}) defined as

$$h_{rss} = \sqrt{\int_{-\infty}^{\infty} dt (|h_+(t)|^2 + |h_{\times}(t)|^2)}.$$

Assuming a source at a distance r that emits GWs isotropically in a narrow frequency range f_0 , the energy released by that source in gravitational waves is

$$E_{GW} = \frac{\pi^2 c^3}{G} r^2 f_0^2 h_{rss}^2 \quad (2.9)$$

as shown by Sutton [35]. Values of E_{GW} from simulations of astrophysical sources, usually given in units of solar mass times the speed of light squared ($m_{\odot}c^2$), range from $10^{-8} m_{\odot}c^2$ for core collapse supernova to $10^{-2} m_{\odot}c^2$ for long gamma ray bursts in very optimistic scenarios. Inverting the equation above and assuming a source 10 kpc away that isotropically emitted $10^{-8} m_{\odot}c^2$ of energy at a frequency of 100 Hz the resulting root-sum-square of strain would be

$$h_{rss} \sim 10^{-21} \text{ Hz}^{-1/2}$$

I will present a targeted burst search for GW signals associated with GRBs in greater detail in chapter IV.

2.3.3. CW

Sources of continuous gravitational waves emit over a long period of time at a nearly constant frequency. The canonical source of such radiation in the context of ground based gravitational wave detectors are galactic neutron stars (with some non-spherical deformation) spinning at a frequency in the band of the detectors. The characteristic amplitude of a gravitational wave from a pulsar scales as [36]

$$h \sim \frac{I f^2 \epsilon}{r}$$

where I is the moment of inertia, f is the gravitational wave frequency, ϵ is a measure of the deviation from asymmetry, and r is the distance to the pulsar. Targeted searches for GWs from known pulsars as well as surveys for unknown neutron stars are done with LIGO data [37].

2.3.4. Stochastic

The final category of GW source refers to a random gravitational wave background that could be detectable due to its statistical properties. The sources that could contribute to a stochastic background could be, for example, spinning neutron stars, cosmic strings, gravitational waves produced during inflation, coalescing binaries at large distances, or supernova. Stochastic searches operate by cross-correlating [38] data from a network of GW detectors and are typically divided into isotropic searches (such as in Abbott et al. [39]) or directional searches (such as in Abbott et al. [40]) that look for deviations from an isotropic background that could occur at cosmological distance or from nearby regions such as the galactic center. Although it is unlikely with current instruments, the detection of a

cosmological background of GWs from the inflationary epoch in the early universe would be a monumental discovery!

2.4. GW Detectors

By now, it is clear that GWs are predicted by general relativity, and can reasonably be produced by realistic astrophysical sources—albeit with very small strain amplitudes on earth. Next, we will turn our attention to the topic of gravitational wave detection. The exceedingly small effect of GWs has given rise to innovative techniques for detection. The only successful method of observing GW so far (other than indirect detection from measuring the orbital decay of binary pulsars) has been ground based laser interferometry. Although the idea of using laser interferometers to detect gravitational waves dates back further, the first one to lay out the technical details was Rainier Weiss in 1972 [41] who eventually received the Nobel prize for the first detection along with Kip Thorne and Barry Barish. Other methods of GW detection have been tried or are still in use: resonant mass detectors [14] pioneered by Joseph Weber drew some interest in the 1960's and 70's but ultimately proved too insensitive to detect GWs; pulsar timing arrays are currently used to search for GWs in the nHz-mHz range; and space based interferometers are planned for operation in the next decade. Here, I will focus on ground based laser-interferometers and the Advanced LIGO detectors in particular.

The Advanced LIGO detectors [42] are kilometer scale Michelson interferometers designed to reach a peak strain sensitivity of better than 10^{-23} in the sensitive frequency band. The basic idea is simple: use a beam-splitter to divert a laser beam down two orthogonal paths (or *arms*); at the end of each

arm mirrors reflect the light back to the beam-splitter where it interferes. During operation, mirrors are held so that the arm lengths differ by $\frac{\lambda}{2}$, up to an integer number wavelengths, and light from each arm destructively interferes so that the output port (see Figure 2.3) is dark. However, a relative change in each arm length (such as from a passing GW) induces a phase shift on the light and some will be transmitted out of the output port. The basic configuration of a Michelson interferometer with a 1000 nm laser and kilometer scale arms would give a strain sensitivity on the order of

$$h = \frac{\Delta l}{l} \sim \frac{10^{-6}}{10^3} = 10^{-9}. \quad (2.10)$$

Clearly, the devil is in the details when getting the interferometer sensitive enough to detect realistic gravitational waves. Although the basic idea is the same, there are many improvements from a simple Michelson interferometer used in the aLIGO detectors, as I will review briefly in the next section.

2.4.1. Advanced LIGO

The real aLIGO interferometers are more complicated than a simple Michelson interferometer, as can be seen in Figure 2.3 which shows the layout of aLIGO during the era of first detections. Each arm is a Fabry-Perot cavity, which increases the effective length of each arm by having the light traverse multiple times across the arm and increases sensitivity to gravitational wave signals. The effective arm length can be increased until approximately when the GW wavelength is reached and the technique ceases to work: this adds about a factor of 10^3 to our earlier estimate (2.10).

Equation 2.10 also assumes that we can only measure the change in optical path length if it was on the order of the wavelength of laser light. However, sensitive photo diodes allow better results: small changes in laser power at the output port can be measured corresponding to minute changes in path length. Therefore, the fundamental sensitivity of the aLIGO instruments are limited by noise sources—such as seismic, thermal and quantum noises that can either move the mirrors or affect the laser light and need to be accounted for in the design of the instrument. As Figure 2.3 also shows, all optical components are enclosed in an ultra-high vacuum system and suspended on pendulums to isolate them from seismic noise. The mirrors at the end of each arm (sometimes called *test masses*) are suspended by a system of four pendulums as in 2.3. Not shown in that diagram are the power recycling and signal recycling cavities which are coupled to the interferometer input and output ports in aLIGO and serve to reflect light back into the detector, thereby increasing the circulating power and reducing a source of quantum noise. The instrument has five length degrees of freedom that must be controlled at a microscopic level to hold the optical cavities at their nominal operating length. The differential arm length degree of freedom, or ‘DARM’, is controlled by a feedback loop whose error signal is calibrated to measure the strain affecting the detector. More details on the aLIGO instrument can be found in Aasi et al. [42] although the fundamental noise sources that limit the detectors warrant further discussion later in this chapter after a brief discussion of the antenna response of a interferometric GW detector.

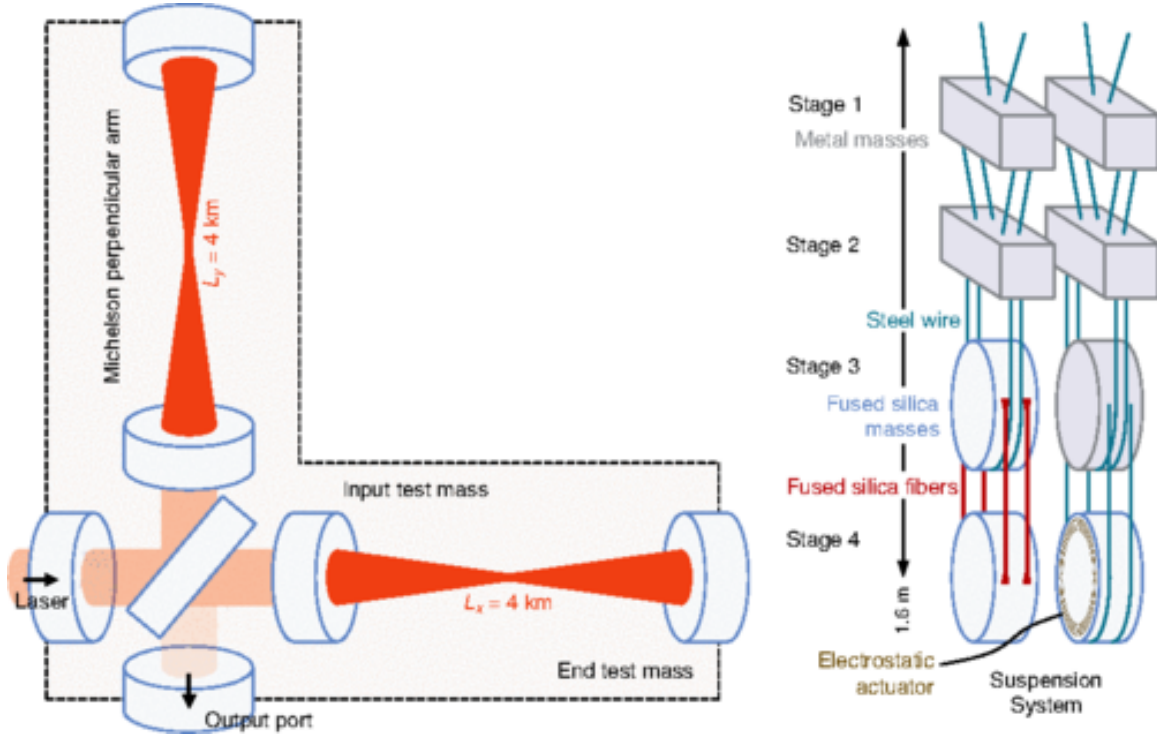


FIGURE 2.3. aLIGO layout with suspensions

A simplified version of the aLIGO optical layout. The test masses are seismically isolated by a four stage pendulum and shown on the right. Figure reproduced from Abbott et al. [43]

2.4.2. Antenna Response

The antenna response of an “L” shaped GW interferometer is fairly isotropic, at least compared to an electromagnetic antenna. However its response still depends on the sky location and polarization of incoming waves. For example, recall from Figure 2.1 the effect of each independent GW polarization on a ring of test particles. An “L” shaped detector in the plane of that ring will clearly have a varying response to a GW signal as the polarization angle or angle of incidence is changed. For example, it is easy to see how the maximal antenna response, for an arbitrary polarization angle, occurs when the detector is in the plane of a GW, but moving the interferometer arms outside of that plane reduces the response.

In general, the gravitational wave strain time series measured by a detector can be written as

$$h(t) = h_+(t)F_+(\theta, \phi) + h_\times(t)F_\times(\theta, \phi), \quad (2.11)$$

where F_+ and F_\times are the detector antenna functions which are given by [44]

$$F_+(\theta, \phi) = \frac{1}{2}(1 + \cos^2 \theta) \cos 2\phi, \quad (2.12)$$

$$F_\times(\theta, \phi) = \cos \theta \sin 2\phi \quad (2.13)$$

for an interferometer with arms in the xy -plane. The angles θ and ϕ refer to the polar and azimuthal angles respectively. The detector antenna functions are plotted in Figure 2.4, where it can be seen that the maximal response is from a GW directly overhead and null points are located in the detector plane at a 45° angle between the interferometer arms. Equation 2.11 will become important for the coherent method of signal detection described in Chapter IV.

2.4.3. Noise sources

Quantum noise sets the theoretical limit for sensitivity over much of the frequency band. Radiation pressure noise and photon shot noise arise from the quantum nature of light. The former refers to momentum transfer from individual photons hitting the test masses and the latter to statistical fluctuations in the photon arrival time at the interferometer output. Shot noise limits the strain sensitivity at frequencies over 100 Hz and scales as the inverse square root of the circulating laser power, which was about 100 kW during the first discoveries.

Thermal noise refers to Brownian motion in the detector components and is the limiting noise source in the central frequency region of the detectors. In

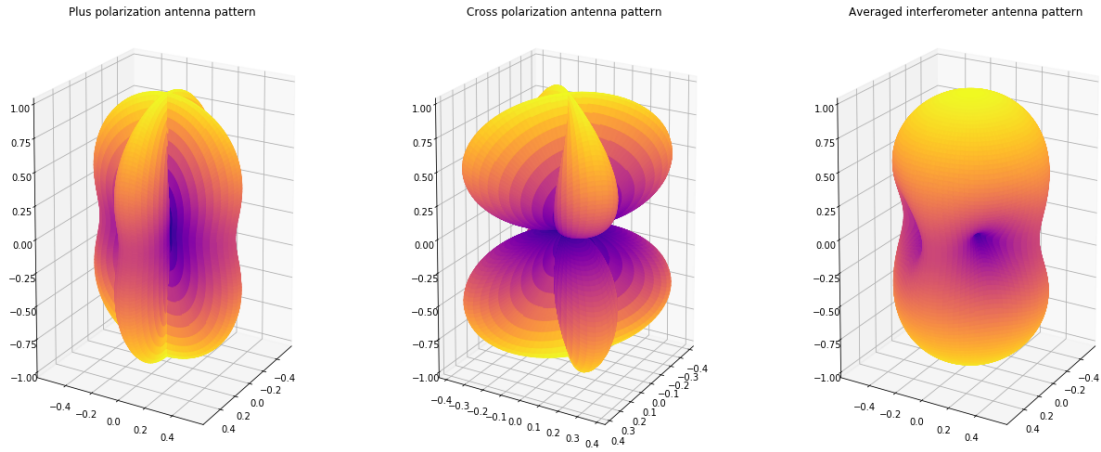


FIGURE 2.4. The antenna response of a LIGO interferometer to a gravitational wave. The patterns are oriented such that interferometer arms live in the xy -plane and nodes in the left panel will occur at a 45° angle between the arms and every 90° around the z axis.

particular, the motion in the suspensions and coatings used for optical components contribute to this noise source. To reduce thermal noise, materials with special properties are selected to provide advantageous thermal properties and cryogenic detectors are being developed (for example, the Japanese KAGRA detector which is currently being commissioned).

The aLIGO test masses are seismically isolated by multi-stage pendulums and active isolation platforms. However, motion can still be transmitted through the isolation system to the test masses, especially at lower frequencies. Additionally, the changing gravitational potential from locally varying mass density due to seismic waves or pressure introduces another source of noise, termed “Newtonian” noise. Newtonian noise could limit the detector in the future, although active compensation techniques with a field of local sensors are being developed. These sources of noise which contribute to setting the strain sensitivity of aLIGO are show in 2.5.

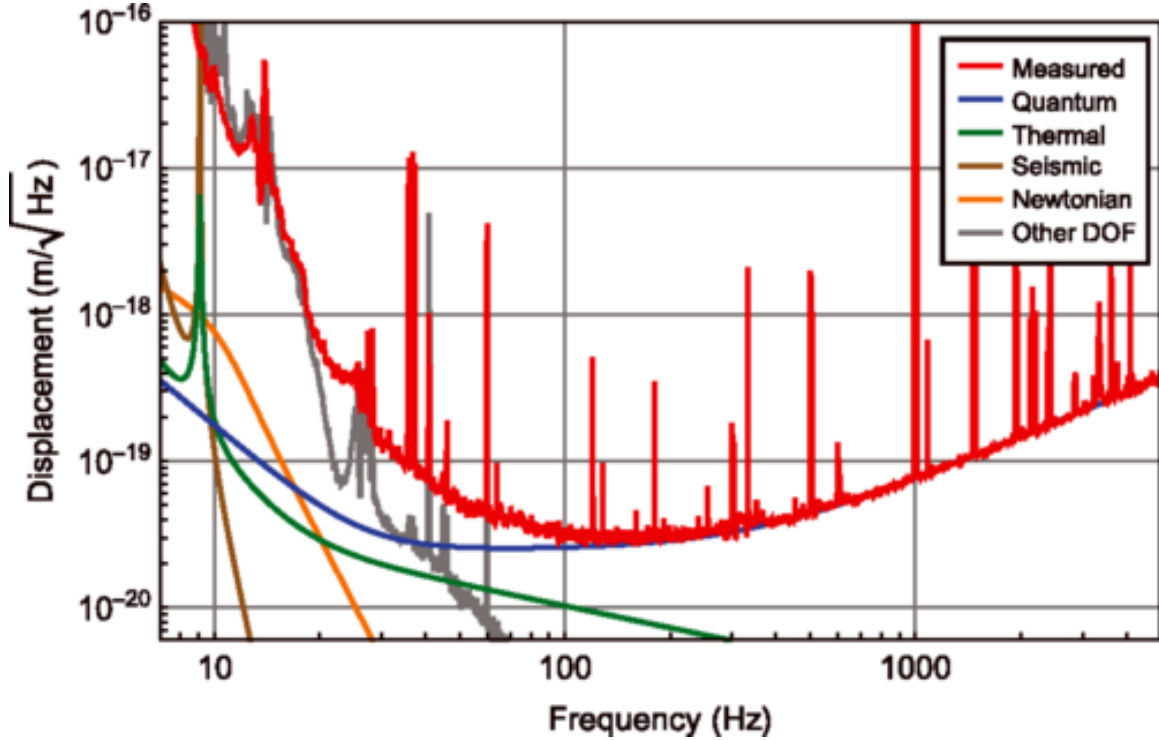


FIGURE 2.5. aLIGO noise curve

The displacement sensitivity of Hanford Advanced LIGO detector from the start of O1. Figure reproduced from Abbott et al. [43]

One other aspect of the aLIGO detectors that is relevant to this dissertation is the physical environment monitoring (PEM) system. The PEM system consists of numerous sensors spread around the detectors that are used to detect environmental disturbances around the interferometer: disturbances that could couple into DARM and pollute a gravitational wave measurement. It is relevant because I was part of the team that installed the PEM system at LIGO-Hanford before O1 and PEM-related topics will be the subject of Chapter 5.

To summarize, this chapter has shown that Einstein’s theory of general relativity predicts the existence of gravitational waves, as can be seen in the linearized limit. We discussed several astrophysical scenarios that could lead to detectable GW and presented the method used to detect GW with aLIGO. The

next chapter will explore the connection between GWs and a related astrophysical phenomenon — GRBs — which have an interesting history in their own right.

CHAPTER III

GAMMA-RAY BURSTS

The history of Gamma-Ray Burst science is an interesting detective story. Starting with a serendipitous discovery by the *Vela* satellite mission designed to monitor nuclear test ban compliance and culminating in the multi-messenger discovery of GRB 170817A and GW170817, it took scientists decades to unravel the mysteries of GRBs. Many space-based observational missions, in conjunction with ground-based follow-up campaigns and the work of many theorists and modellers, were required to formulate our current understanding of these mysterious events, with the promise of more interesting science in the years to come. This chapter will review some of the important observations that led to the current understanding of GRBs, go over the accepted models of the progenitors of these events, and explore the connection to GW astronomy, especially in the context of GRB 170817A.

3.1. Observations

In the 1960s the Vela series of military satellites were launched to monitor the compliance of the USSR with the 1963 nuclear test ban treaty by searching for short intense flashes of gamma-rays indicative of the detonation of a nuclear weapon. However, the satellites began recording mysterious bursts of gamma-rays that were eventually realized to be of cosmic origin. The existence of these bursts were presented to the public in 1973 [45], beginning a decades long search to explain their origin.

The basic properties of these bursts are that they are a short (usually < 100 s) burst of photons with energies ranging from KeV to GeV and sometimes

higher. The light curves show much diversity from burst to burst. Some show a fast rise time of 10^{-4} s followed by an exponential decay, while others have more structure and can vary quickly on time scales down to milliseconds. Figure 3.1 shows examples of GRB light curves observed by the BATSE instrument [46]. The typical fluence (energy flux integrated over the burst duration) can range from

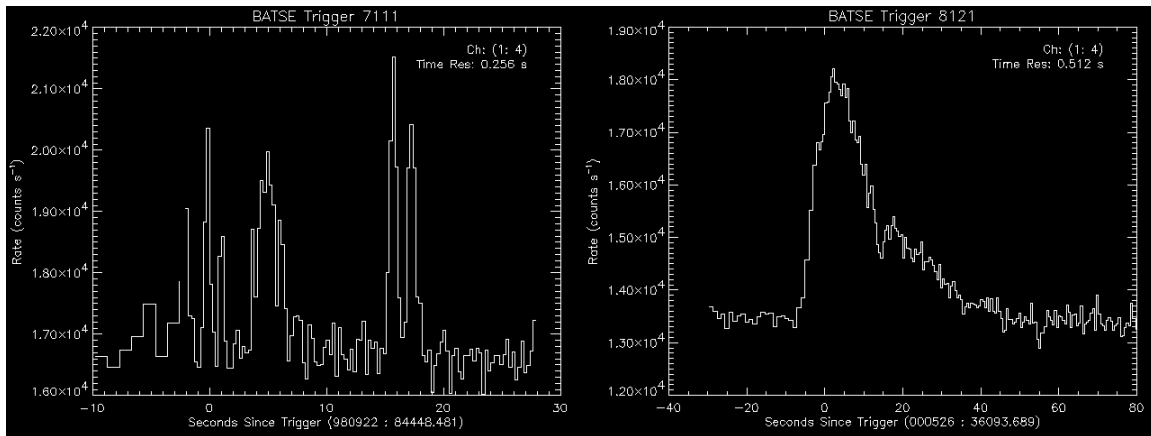


FIGURE 3.1. Example GRB Light Curves.

Light curves of GRB 980922 and GRB 000526 from all channels 1-4 of the BATSE instrument. The x -axis indicates seconds since trigger and ranges from -10 to 30 seconds in the left panel and -40 to 80 seconds in the right panel. The x -axis indicates the count rate for all BATSE channels which are sensitive to gamma-ray photons from 20 keV to over 300 keV. Courtesy of NASA, accessed from <https://gammaray.nsstc.nasa.gov/batse/grb/lightcurve/>.

10^{-12}Jm^{-2} to 10^{-7}Jm^{-2} .

For much of the 1990s it was unclear whether the GRBs were originating from a nearby location, such as the solar system or Milky Way galaxy, or if they were cosmological in origin. Early statistical tests based on the isotropy of the bursts on the sky and the fluence distribution favored a cosmological origin. That hypothesis was confirmed when the BeppoSAX spacecraft detected GRB 970228. The spacecraft's X-ray cameras were able to localize the burst to arcminute resolution and enable deep optical follow up, eventually associating the GRB with a

distant galaxy and confirming that GRBs originated at cosmological distances. This was the first observation of a GRB *afterglow*.

Afterglow emission [47] is lower-energy and longer-lasting than the prompt emission. It can be seen in the x-ray, optical, and radio bands sometimes up to years after the GRB. The discovery of GRB afterglows has been hugely important in the development of the field. For starters, afterglow observations have enabled very precise localization of GRBs. This allowed confident associations with host galaxies and finally ended the debate over whether GRBs were cosmological. Localization of some GRBs to star forming regions was also an important clue to their origin as I will discuss later. Furthermore, close inspection of the time evolution of afterglows pointed to GRB emission being narrowly collimated into *jets* with opening angles typically between 2 and 20 degrees. This shows up in the afterglow observations because a jet appears to dim more quickly than a spherical source would as it expands and cools. This phenomena, known as a *jet break* [48] has been observed for many GRBs and beamed emission is part of the generally accepted model, although the precise details are still under investigation.

Knowing the distance to the source, it becomes possible to estimate the intrinsic energy released by the burst. For example, assuming isotropic emission, the energy released at the source would be $E = (4\pi D^2)S$ where D is the luminosity distance and S is the fluence. For a typical GRB fluence of $S = 1 \text{ erg m}^{-2}$ and a distance of 1 Gpc, the amount of energy released would be 10^{52} ergs, exceeding a hundred times the total energy radiated by a supernova. As it turns out, GRB emission is *beamed* rather than isotropic which means that simple calculation is an over estimate (typical beaming-corrected total energy released are $\sim 10^{51}$ ergs), which places GRBs among the most energetic phenomena known to exist.

Despite their heterogeneous emission properties, such as light curve, duration, and fluence that can vary wildly from burst to burst, GRBs can be divided into two distinct classes: short-hard and long-soft. The short/long distinction refers to the duration of the burst and the common cutoff used is a T90 of 2 s although that can vary between detectors that are sensitive to different energy bands (T90 is defined as the time that 90% of the burst energy is captured). The hard (soft) distinction means that short (long) bursts have proportionally more photons in the high energy band of the detectors. This was primarily discovered by investigating the data from the BATSE instrument aboard the CGRO satellite (see figure 3.2). These two classes of GRBs were long thought to come from different physical sources, and that has been confirmed as I will discuss in the following section.

The spectra of GRBs are non thermal. They typically peak around a few hundred keV and often have long tails up to the MeV and GeV energy range. They are phenomenologically described by Band et al. [50] as a broken power law. This empirical model contains two power laws with different indices smoothly stitched together at some break energy.

The rise time δt of GRB light curves naively imply a length scale of $c\delta t$. Characteristic length scales as small as tens of kilometers fueled early speculation that neutron stars could be involved. This short length scale combined with the large amount of energy released implies a large energy density that would be opaque due to pair-production from photon-photon collisions. However, this implied thick optical depth at the source conflicts with the observed non-thermal spectrum. This apparent contradiction is elegantly resolved by the inclusion of relativistic effects. In the most popular model used to describe the observed GRB emission, the fireball model [51], there is a “central engine” that produces a

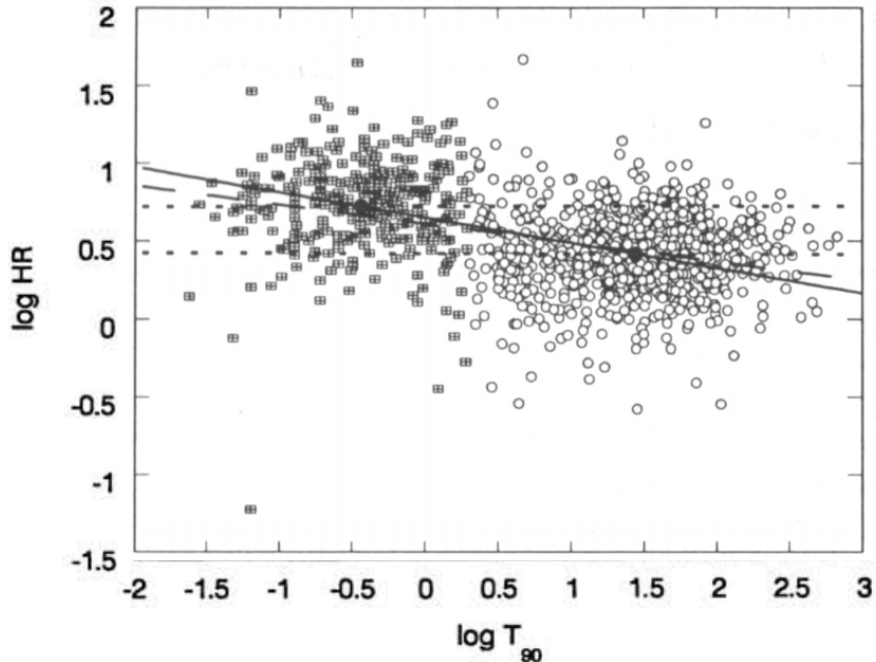


FIGURE 3.2. Hardness versus duration for BATSE GRBs.

HR is the ratio between the fluence in channels 3 and 2 in BATSE. T_{90} is measured in seconds. Squares correspond to short bursts and circles to long ones, while the filled circles represent the average of each class. Regression lines are included for each class individually and the total sample. Figure reproduced from Qin et al. [49]

relativistic energy flow which is transported some distance away and then converted into the radiation that is observed. The expanding relativistic fireball is dominated by e^\pm and photons at early times and later by relativistically accelerated baryons. The conversion of this kinetic energy into observed gamma-ray photons occur via *shocks*: when shells of relativistic material moving outward at different speeds interact (internal shocks), as in figure 3.3. Afterglow emission occurs when the jet interacts with the surrounding medium (external shocks). In this way, the expanding fireball material is optically thin by the time the photons are emitted so that high energy photons do not undergo pair production. Furthermore, the photons are blue shifted in the observer frame and these effects account for the

observed non thermal spectrum with high energy tails. Finally, this model naturally incorporates relativistic beaming, as an observer only sees radiation from a region with Γ^{-1} , where Γ is the bulk Lorentz factor of the emitting region.

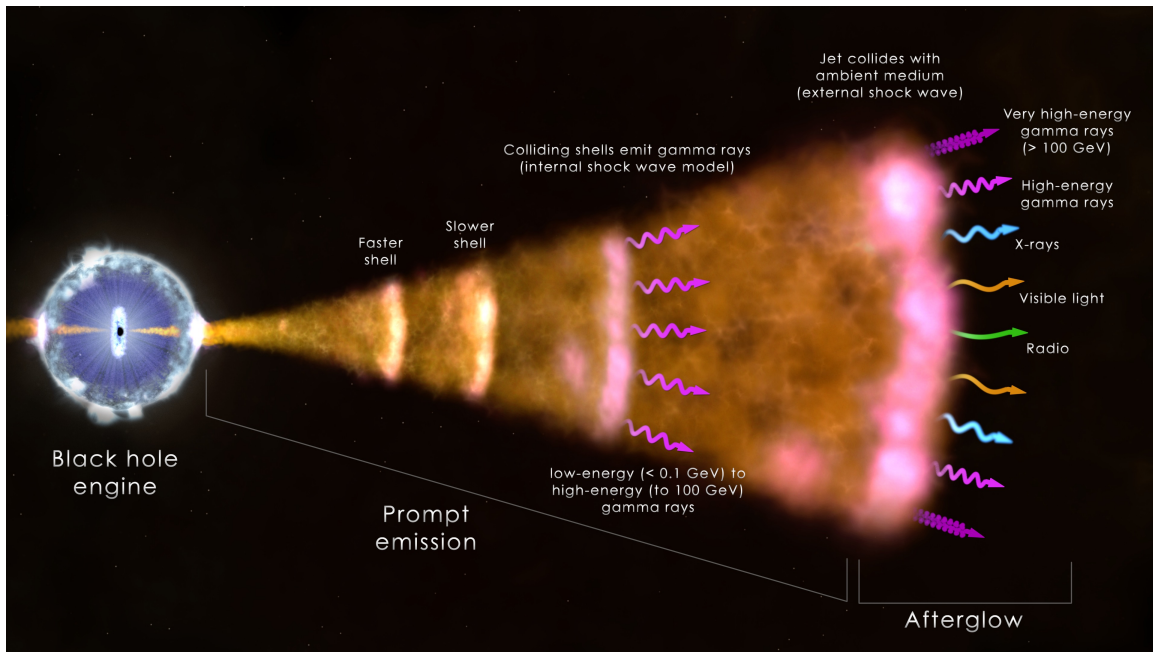


FIGURE 3.3. Illustration of GRB mechanism.

The illustration shows a central engine powering a jet of relativistic particles. The GRB is produced by shocks when shells of relativistic material moving at different speeds interact. Afterglow emission over the whole EM spectrum occurs when the jet interacts with the circumburst medium. Image from NASA/Goddard Space Flight Center.

This simple fireball model can mostly explain the observed radiation from GRBs, although the model is agnostic about the compact central engine and how that is formed. Also, the model does not explain how the two classes of GRBs arise, which is discussed in the following section.

3.2. Progenitor Models

The long-soft and short-hard classes of GRBs were first noticed in the BATSE catalog [46]. It was thought early on that each class could arise from different

progenitors, which has been proven correct over the decades. The population of long GRBs has been easier to pin down (and it didn't hurt that there are more long GRB observations and afterglows available to analyze). When precise localization was possible through afterglow observations, it became clear that the long GRBs were coming from star forming regions in galaxies. These regions contain massive stars that end their lives via supernova within hundreds of millions of years. This was the first evidence that long GRBs could be associated with the death of single, massive stars. The link was confirmed when GRB 980425 was observed in conjunction with the Type Ic SN 1998bw [52]. Over the years, more observations have confirmed that long GRBs arise in star forming regions and are associated with supernovae (or *hypernovae* from very massive, highly rotating stars). Now, the consensus view is that Long GRBs are associated with the death of massive stars although there are different models about the actual mechanism for the central engine. For example, in the collapsar model first put forward by Woosley [53] the GRB fireball is produced during a “failed” supernova: the core of a massive star collapses directly into a black hole and surrounding matter forms an accretion disk which powers the jets responsible for the observed radiation.

Early on, the short bursts proved more difficult to pin down. The role of neutron star mergers in the production of GRB had always been suspected. Even though they were ruled out for producing long bursts they remained a popular explanation for the short bursts. Some observational help arrived when the Neil Gehrels Swift observatory came online in 2005. With GRB 050509B, *Swift* was able to detect the first x-ray afterglow and precisely localize a short GRB [54]. The ensuing observations seemed to be consistent with the popular theory: short GRBs are produced by the merger of neutron stars. For example, the spatial distribution

(offset from host) and lack of supernova association were both consistent with binary mergers [55]. Two key predictions of the BNS merger model were the presence of detectable gravitational waves accompanying GRB and the presence of a supernova-like counterpart known as a *kilonova* (see Metzger [56] and references therein). Both of these predictions were spectacularly confirmed in 2017 with the detection of GW 170817 in conjunction with GRB 170817A by the LIGO/Virgo and Fermi collaborations.

3.3. GRB 170817A

As mentioned earlier, the LIGO/Virgo detectors detected a binary neutron signal [9] in coincidence with a GRB [57] on August 17, 2017. The GRB lightcurves and GW signal are shown in figure 3.4. This coincidence, based on the nearly simultaneous temporal and spatial observations had a chance probability of 5.0×10^{-8} [2]. The association immediately confirmed that BNS mergers were responsible for (at least some) short GRBs. The difference in arrival time between the GW and gamma-ray signals was measured to be 1.74 ± 0.05 s and from this measurement the difference between the speed of gravity and the speed of light was constrained to between -3×10^{-15} and $+7 \times 10^{-16}$ times the speed of light. It also placed bounds on Lorentz invariance and provided a new test of the equivalence principle via constraints on Shapiro delay. Importantly, alerts from this joint detection provided a better sky localization than either gamma-rays or GWs on their own. Follow up campaigns were able to identify optical, x-ray, and radio counterparts that unlocked further discoveries.

By its location in the duration-hardness plane, GRB170817 could be clearly classified as a regular short GRB. However, it was fainter than most and later

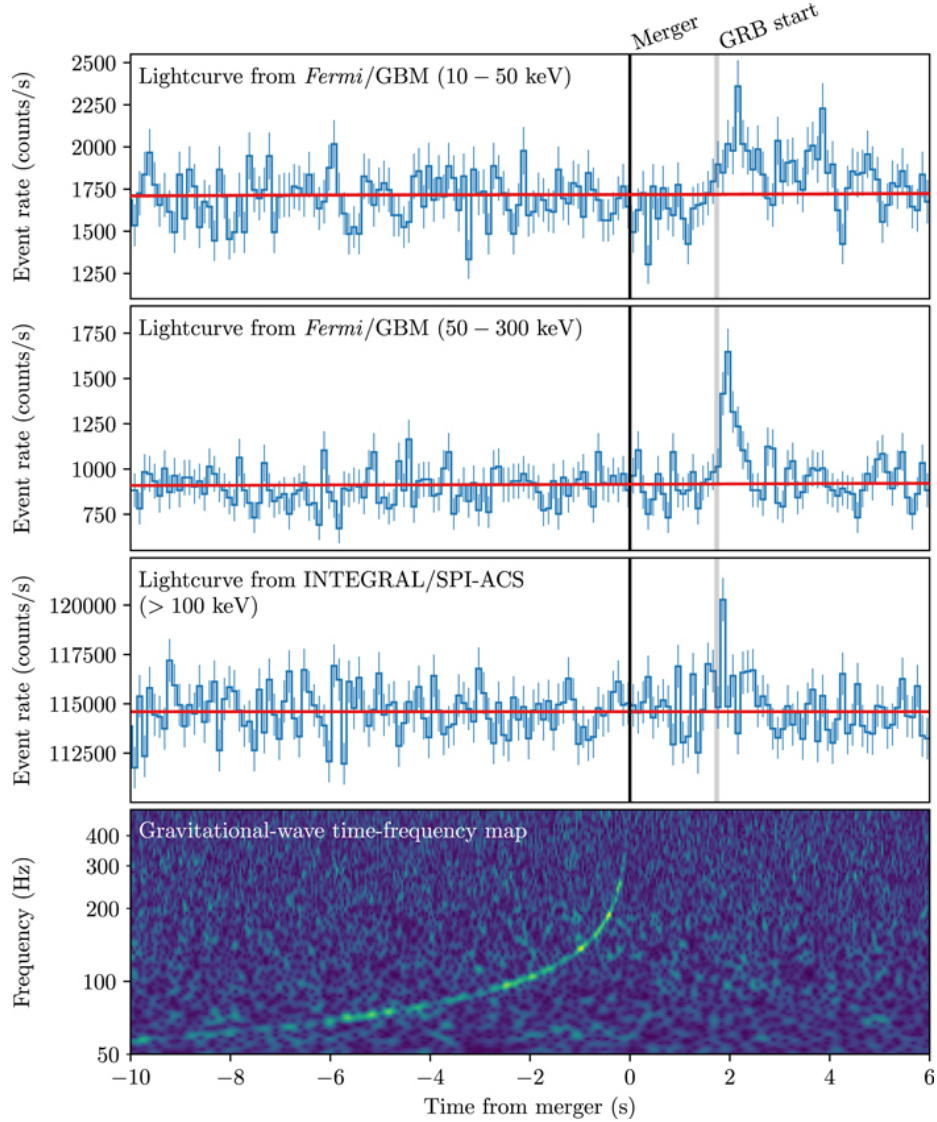


FIGURE 3.4. Joint GRB lightcurves and GW strain signal from the joint multimessenger of GRB 170817A and GW170817. Figure reproduced from [2]

turned out to be the closest GRB observed. The X-ray afterglow as not observable until days later, which contradicted the standard GRB model for an on-axis observer. The resolution to these tensions has been explained by the fact that GRB 170817 was viewed off-axis. A *structured* jet, whose intensity depends on viewing angle, produces the dim GRB and the afterglow is delayed due to the time it takes for the core of the jet to become visible as it slows. The structured

jet profile has further been constrained through radio measurements months and years later [58, 59, 60].

The optical afterglow has shown the presence of kilonova emission [61] caused by neutron-rich matter ejected from the binary system during merger. This kilonova emission contained the distinct signature of heavy elements, such as gold and platinum, being produced in a process known as rapid neutron capture (r-process) nucleosynthesis. In fact, the amount of mass ejected from this system suggests that binary neutron-star mergers may be a dominant source of r-process elements in the galaxy [61].

Finally, it is relevant to mention that I contributed to an analysis of GW data around GRB 170817A published in Abbott et al. [2]. That analysis was an unmodelled search for GWs assuming the GRB signal localized by Fermi was genuine, and returned a p-value of 1.3×10^{-5} for the GW strain measured by LIGO to have come from noise. This result served to increase confidence in the association early on before the consensus model for these observations had emerged. The methods, background, and more context for this analysis is provided in Chapter V.

3.4. GRBs as Sources of Gravitational Waves

The next chapter will focus on triggered follow-up searches for gravitational waves associated with GRBs. Before that, it would be good to review the model presented in this chapter with a focus on the generation of gravitational radiation that could be detectable by LIGO.

Due to the fact that GW generation would occur in the central engine, the standard fireball model for GRB emission does not say much about GW. However,

the beaming angle does have implications for GW detection. First off, since GW emission is roughly isotropic the expected rate of joint detection depends strongly on the GRB beaming angle. Conversely, measurement of the rate can be used to constrain the GRB opening angle which has been done, e.g., by Chen and Holz [62] and Williams et al. [63]. Also, since GRB emission is beamed along the rotational axis of the central engine, it is reasonable to assume that GW emission will be roughly circularly polarized; this can be important when designing searches for these GWs.

The distinctly different central engines of each GRB class will also have a strong effect on the expected GW emission. Short burst progenitors, NS-NS or NS-BH mergers, are strong emitters of gravitational waves known as compact coalescing binaries. These are efficient sources, with up to 1% of the total mass-energy of the system emitted as GWs and with a signal morphology that can be precisely modelled as discussed in the previous chapter. The inspiral signal from a light binary can last for minutes in the sensitive band of the LIGO detectors. In fact, efforts are ongoing to develop procedures whereby alerts are sent to electromagnetic observers prior to merger. Also, for short bursts, gamma-rays are expected to arrive at earth within a few seconds of the GW merger signal. which was true for GRB170817A (see figure 3.4).

Long GRBs have GW counterparts that are harder to model (see Fryer and New [31]). At common GRB distances, the standard picture for these events (core collapse of a massive star to a black hole with accretion powering GRB jet) make it hard to envision detectable GWs in general. Some simulations have shown the amount of energy released can be up to $E_{\text{GW}} = 10^{-2} M_{\odot} c^2$, although realistically the amount of energy released is much lower. While precise models are used to

search for GW emission from short GRBs, the nature of long bursts require more generic searches. One such search is described in the following chapter.

CHAPTER IV

SEARCH FOR GRAVITATIONAL WAVES ASSOCIATED WITH GAMMA RAY BURSTS

As discussed in the previous chapters, GRBs are natural candidates for sources of gravitational wave burst (GWB) due to their large energy budgets and compact matter distributions. This chapter considers the problem of detecting GWs from GRBs in realistic detector strain output. The problem of finding a small GWB in the presence of instrumental noise is compounded by the fact that realistic noise is often non-Gaussian. Many methods exist in the literature for GWB signal detection, ranging from matched-filter searches for known signal morphologies to searches for generic signals as well as from searches over the whole sky to triggered searches limited in time and duration. For the case of GRBs, basic properties of associated GWs can be assumed such as the time and sky position, which effectively lowers the parameter space we need to search for the signal. In the following sections we discuss basic concepts in statistical signal analysis before introducing the X-pipeline analysis package and finally presenting results from the O2 search.

4.1. Signal detection preliminaries

The time series output of a gravitational wave detector, $d(t)$, can be thought of as the sum of the detector noise $n(t)$ and a signal $h(t)$ which may be present or not:

$$d(t) = n(t) + h(t)$$

Using Bayes's theorem, the probability of the signal being present in the data is

$$p(h|d) = \frac{p(h)p(d|h)}{p(d)}$$

where $p(h)$ is the prior probability of the signal being present; $p(d)$ is the marginal probability of the data, known as the evidence; and $p(d|h)$ is the probability of getting the data given the signal hypothesis—called the likelihood. The denominator can be expanded as $p(d) = p(h)p(d|h) + p(0)p(d|0)$, making explicit the fact that there are two scenarios—signal or no signal. In terms of $\Lambda = \frac{p(d|h)}{p(d|0)}$, known as the *likelihood ratio*, the above can be written as

$$p(h|d) = \frac{p(h)p(d|h)}{p(h)p(d|h) + p(0)p(d|0)} = \frac{\Lambda}{\Lambda + p(0)/p(h)}$$

In this form, it is clear that the probability of a signal existing in the data is a monotonically increasing function of Λ , and Λ is the only term that depends on the data (since the ratio of priors is constant for a particular signal). The likelihood ratio is the optimal statistic in the Neyman-Pearson sense: it is the most powerful statistic to test between the competing hypotheses of signal versus no signal for a given false alarm rate. Since Λ can get very large the quantity $\log \Lambda$ is typically discussed and plotted, however any function that is increasing monotonically with the likelihood ratio suffices.

To illustrate this consider the simplest case: a known signal $h(t)$ in the presence of Gaussian noise. In this case, the probability $p(n)$ of obtaining a time series of detector noise $n(t)$ is

$$p(n) \propto e^{-(n,n)/2}$$

where the (n, n) notation refers to the noise-weighted inner product which is commonly defined (see, e.g., Brown [24]) as

$$(a, b) = \int_{-\infty}^{\infty} \frac{\tilde{a}\tilde{b}^* + \tilde{a}^*\tilde{b}}{S(|f|)} df$$

and $\tilde{a} = \tilde{a}(f)$ is the Fourier transform of $a(t)$, and $S(|f|)$ is the one-sided power spectral density of the noise. When the data stream does contain a signal, $d(t) = n(t) + h(t)$ and the probability can be written as $p(n) = d(t) - h(t)$. Then the likelihood becomes:

$$\begin{aligned} \Lambda &= \frac{p(d-h)}{p(d)} = \exp \left[-\frac{1}{2}(d-h, d-h) + \frac{1}{2}(d, d) \right] \\ &= \exp \left[-\frac{1}{2}(d, d) + (d, h) + \frac{1}{2}(h, h) + \frac{1}{2}(d, d) \right] \\ &= \exp \left[(d, h) + \frac{1}{2}(h, h) \right] \end{aligned}$$

we can threshold on part of that expression that increases monotonically with the likelihood ratio and depends on the data, namely (d, h) . This defines the basic matched filter which is completely derived in other sources such as Creighton and Anderson [23], Brown [24].

Typically, not everything is known about the signal a priori. For example, in a CBC search the amplitude, arrival time, or other parameters may not be known. The signal then depends on some set of parameters θ so that the signal can be written as $h(t; \theta)$. We then marginalize over the parameters θ in the likelihood:

$$\Lambda = \int \Lambda(\theta)p(\theta)d\theta$$

where $\Lambda(\theta)$ is the likelihood ratio for a signal with a particular parameter θ and $p(\theta)$ is the prior probability distribution for the parameters. The likelihood is then computed for many values of the parameters θ and the values which give the largest likelihood are used. This is known as the maximum likelihood statistic. Symbolically, in the presence of Gaussian noise the log of the likelihood ratio is

$$\ln \Lambda = (d, h(\theta)) - \frac{1}{2}(h(\theta), h(\theta))$$

and maximum is achieved at

$$\left(d - h(\theta), \frac{\partial}{\partial \theta} h(\theta) \right) \Big|_{\theta=\theta_{\max}}.$$

To search for signals where $h(t)$ is not well modeled, we can begin by writing the signal in some orthonormal basis as $h(t) = \sum_i c_i \hat{e}_i$ where c_i are coefficients and \hat{e}_i are the basis vectors (these could be, for example, Fourier components or wavelets that span the possible signal space). Then the likelihood ratio becomes

$$\ln \Lambda = \sum_i \left[c_i (d, \hat{e}_i) - \frac{1}{2} c_i^2 \right]$$

which is maximized when the coefficients are $c_{i,\max} = (d, \hat{e}_i)$. Substituting this back into the likelihood yields the excess power statistic \mathcal{E} defined as

$$\mathcal{E} = 2 \ln(\Lambda) = \sum_i (d, \hat{e}_i)^2.$$

In the case of Gaussian noise, \mathcal{E} is distributed as a chi-squared distribution where the number of degrees of freedom is equal to the number of basis vectors used to define the signal [64].

While it hardly scratches the surface of how GW searches work in practice, the excess power statistic gives a sense for how a real search may work: searches for unmodelled signals are essentially excess power searches. One glaring omission so far is that the noise associated with real GW detectors has components that are non-Gaussian distributed. This means that the statistics shown in this section don't necessarily perform well on real data, though many methods have been developed to alleviate this. In the next section I will describe X-pipeline which is one example of a software package that can robustly detect bursts of gravitational waves with a priori unknown waveforms in the presence of non-stationary noise. The most important feature that enables the following approach is the use of a detector *network*. This allows X-pipeline to use coherent likelihoods where the GW signal is required to be coherent over the network. Conversely, other statistics that do not contain coherent power can be calculated and consistency checks can be created to rule out non-Gaussian noise artifacts, or *glitches*. Furthermore, statistical properties of the likelihoods in non-Gaussian noise can be measured empirically by observing lots of data containing no signal. Signal-free data is guaranteed by looking at times away from the GRB trigger, and by introducing unphysical relative time-shifts to the data from different detectors.

4.2. X-Pipeline

X-pipeline has been used to search for GWs associated with GRBs since LIGO's fifth science run in 2010 [65] and is a generalization of the cross-correlation method used for initial GRB searches earlier on [5]. It is a coherent search that assumes the GW signal has a short duration with a known arrival time and sky location (an astrophysically *triggered* search). A complete explanation of the X-

pipeline software package can be found in Sutton et al. [3] with more details in Was et al. [66] and Was [67]. Here I will give a general overview that suffices to understand how the O2 GRB search operated, starting with a brief description of the type of coherent likelihood utilized by X-pipeline.

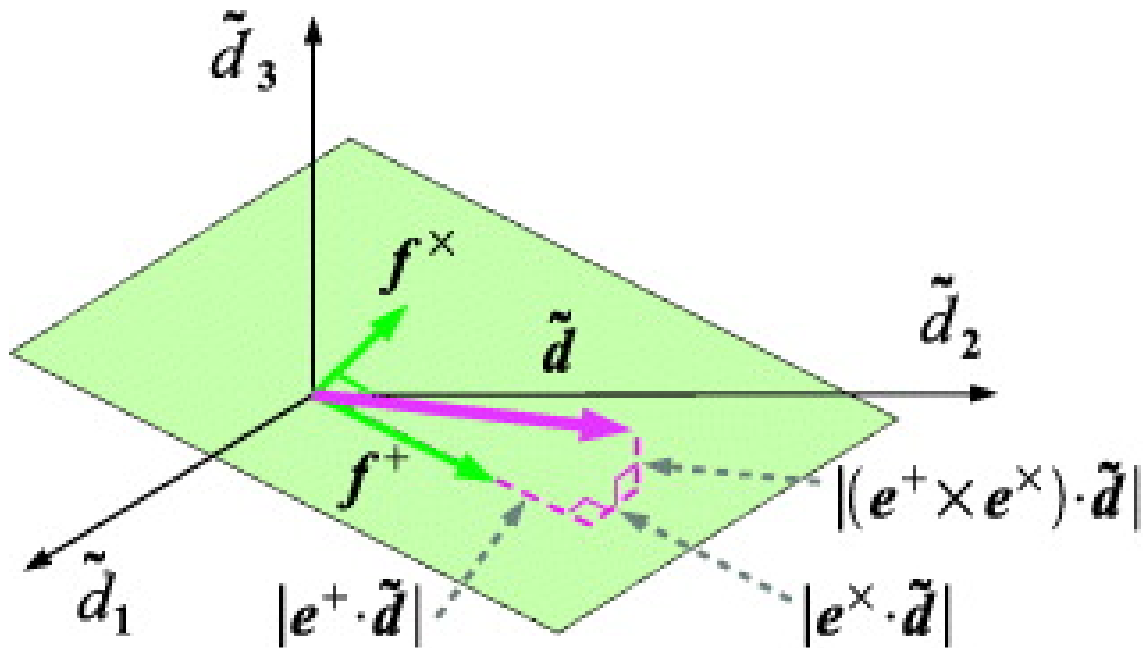


FIGURE 4.1. Data projected onto f_+ , f_\times space. The projection of a data sample from a three detector network. The green plane defines the space spanned by f_+ and f_\times . Figure reproduced from Sutton et al. [3]

4.2.1. Coherent Likelihood

Since the response of an interferometer to a gravitational wave is not perfectly isotropic (it depends on the sky location of the source and the polarization of the wave, as described in chapter III) we can use (2.11) to write the detector output as

$$d(t) = F_+ h_+(t) + F_\times h_\times(t) + n(t)$$

where F_+ and F_\times are the antenna response functions that depend on the sky location. For a network of D detectors we can express the previous equation in terms of matrices:

$$\mathbf{d} = \mathbf{F}\mathbf{h} + \mathbf{n}$$

where \mathbf{d} is a D by 1 dimension vector containing the data from each detector (time shifted to a reference location based on the speed-of-light propagation time of GWs), \mathbf{F} is a D by 2 dimension matrix containing the antenna response of each detector to both polarizations, \mathbf{h} is a vector containing the signal (2 dimensions; one for each polarization), and \mathbf{n} is a D dimension vector containing the noise (timeshifted or not). The data, signal, and noise are usually represented in the Fourier domain. Conceptually, we can follow a similar procedure for signal detection as outlined earlier with the matched filter but instead of having some template waveform our template is the known antenna response of the network \mathbf{F} . We create detection statistics out of linear combinations of the data that are sensitive to GWs. For example, the simplest likelihood in X-pipeline, called the *standard likelihood*, was derived in Sutton et al. [3] assuming Gaussian noise and maximizing the likelihood ratio over possible waveform values:

$$E_{SL} = \sum_k \mathbf{d}^\dagger \mathbf{P}^{GW} \mathbf{d}$$

where $\mathbf{P}^{GW} = \mathbf{F}(\mathbf{F}^\dagger \mathbf{F})^{-1} \mathbf{F}^\dagger$ is a projection operator that projects the data into the subspace spanned by \mathbf{F}^+ and \mathbf{F}^\times .

A common way to write the likelihood is to choose a particular orthonormal basis, known as the *dominant polarization frame* [3, 67], where the basis vectors are defined by the maximum and minimum of the antenna response of the network.

The polarizations are defined such that F^+ lies along the maximal basis vector and F^\times along the minimum. Unit vectors are then defined as $e^+ = F^+ / |F^+|$ and $e^\times = F^\times / |F^\times|$ (see Figure 4.1) and the standard likelihood becomes

$$E_{SL} = \sum_k \left[|e^+ \cdot d|^2 + |e^\times \cdot d|^2 \right].$$

Other likelihoods have been developed and are available for use in X-pipeline. Notably, two likelihoods that have been used in recently published GRB searches include the powerlaw statistic that is effective for two detectors in the presence of non-Gaussian noise [67] and the loghbayesiancirc statistic which is a bayesian-inspired likelihood statistic for circularly polarized signals (which is a reasonable assumption for GWs from GRBs) [66].

Going from the likelihood of a single data sample to the likelihood of an arbitrary gravitational wave burst is done in X-pipeline with a clustering approach. For a GW search with a known sky position, the detection statistic is computed for each pixel in a time-frequency map and pixels with detection statistic above a certain threshold are clustered to form candidate events. Typically, time-frequency pixels in a regular grid are combined with all of the neighboring 8 pixels that have a likelihood value above the threshold, although generalized clustering approaches have been used. The detection statistic from each pixel in the cluster is summed to give the final detection statistic of the event. The likelihoods are recomputed over values of user requested search parameters such as FFT lengths (to construct clusters that better fit possible signals) and with different relative time-shifts when searching over a discrete grid of sky positions. Figure 4.2 shows an example of a time-frequency map for a 20 s segment of data where the color axis indicates the standard likelihood value. In this example, the upward chirp is from the

GRB 170817 signal and the other bright pixels are noise artifacts which should be cut out by the methods described in the following sections.

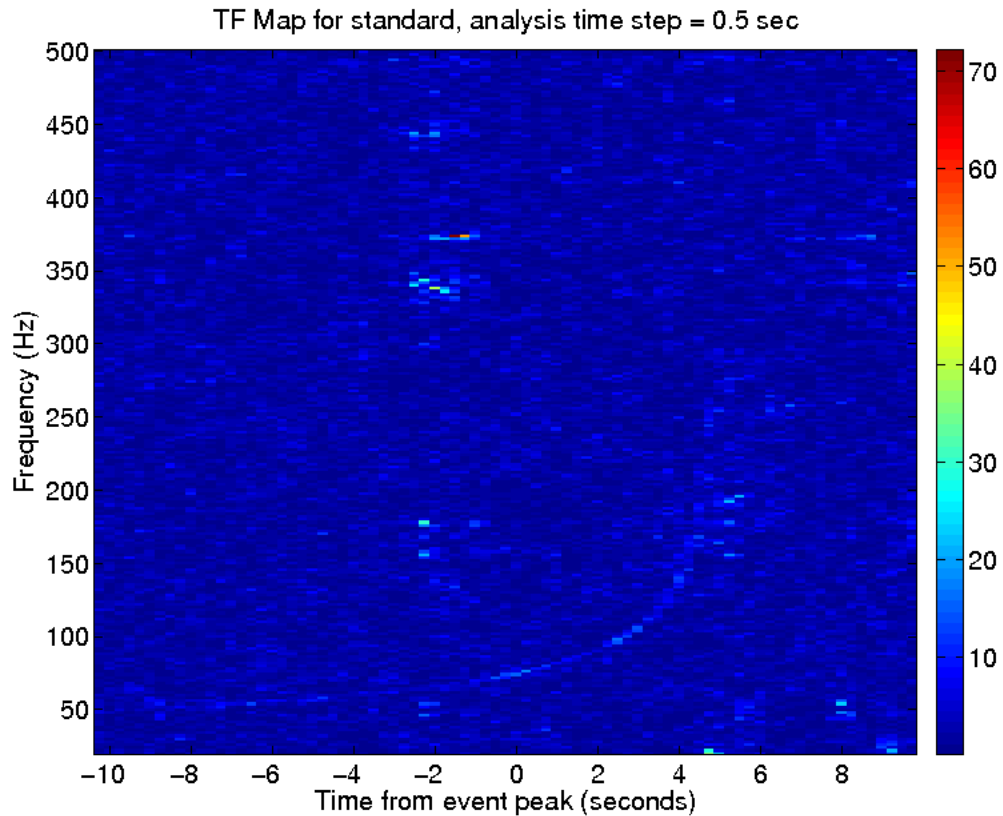


FIGURE 4.2. Time-frequency map of the standard likelihood for GRB 170817, where the color indicates the log of the likelihood. The BNS signal can be faintly seen chirping upwards from 50 Hz to around 250 Hz ending a little after 4 seconds. Bright pixels not on this track are from instrumental noise.

4.2.2. Consistency tests

Although the likelihoods discussed above are constructed to be sensitive to coherent GW signals, they still may return large values for spurious noise transients from the detectors. In addition to the likelihoods discussed above, it is possible to create linear combinations of the data which are insensitive to coherent GWs

signals. These combinations are called *null* statistics and can be used to form consistency tests to reject noise transients. Loud glitches in a single detector will cause the detection statistic and the null statistic to both be large whereas a true gravitational wave signal ought to return a high detection statistic and a low null statistic. In this way, tests based on the ratio of these quantities can be used to reject background noise.

Coherent GW signals are mostly cancelled out in a null stream, however imperfect cancellations can occur due to calibration errors, a discrete sky grid, or incorrect assumptions about polarization. An analysis relying on the null energy could therefore have issues rejecting large glitches. It has been shown [68] that a more robust method to discriminate signal from noise is to compare these null statistics to their *incoherent* counterparts. For some projection onto a unit vector e_α the associated coherent energy is

$$E_\alpha = |e^\alpha \cdot d|^2$$

and the associated incoherent energy is

$$I_\alpha = \sum_i |e_i^\alpha|^2 |d_i|^2.$$

A real GW signal mostly cancels out in the null energy, but no cancellation occurs for an incoherent statistic. Therefore, the ratio I_{null}/E_{null} is close to 1 for a glitch and for a true gravitational wave signal it should be large. The actual threshold can be tuned based on nearby data. Figure 4.3 shows a plot of the null energy versus the incoherent null energy for a GRB search.

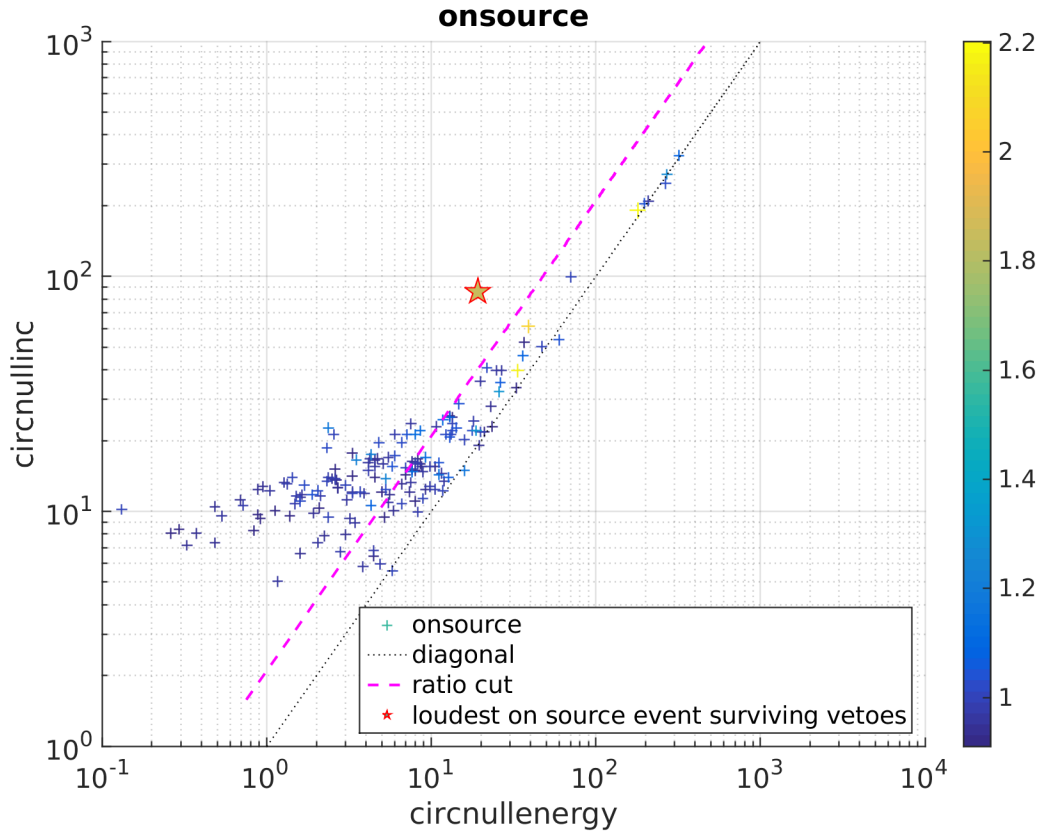


FIGURE 4.3. Incoherent null energy versus null energy for an example GRB analysis. Each cross represents a particular cluster colored according to its detection statistic value. Clusters that lie below the pink dashed line are discarded. The star corresponds to the loudest surviving cluster which can be found in Figure 4.2.

4.2.3. Data-quality Vetoes

In addition to the signal consistency tests that were just discussed, the presence of instrumental noise in the detectors can be gleaned from an thorough understanding of the interferometer and noise processes inherent in its operation. Periods of time where the strain data from a detector are contaminated with excess noise from known instrumental sources are flagged; and these flags are used to veto candidate events from a search—or totally remove stretches of poor-quality data

from the search. These *data-quality vetoes* are generated by setting a threshold on the value of some *auxiliary channel*¹—such as a photodiode or environmental sensor—that indicates when the DARM signal may be contaminated with excess noise. A large network of environmental monitoring sensors, which I contributed to as part of this PhD, are important for the development of these vetoes and will be discussed in Chapter V.

These *data-quality vetoes* can be applied in X-pipeline at different stages of the analysis. Category 1 (CAT1) vetoes are periods of time that are excised from the data-stream prior to analysis; whereas data containing category 2 (CAT2) vetoes are analyzed as normal until candidate events overlapping with the veto segment are discarded. Additionally, frequency based vetoes are applied where we discard events lying with frequency bands that are known to be contaminated with instrumental noise: an example is discussed in Chapter V. In practice, since the signal consistency tests in X-pipeline can also discriminate between instrumental noise transients and GW signals, the particular set of data-quality vetoes to include in a particular search is chosen based on whether they provide increased sensitivity to the search.

4.2.4. Detection Procedure

Having described the coherent likelihood, consistency tests, and vetoes in the previous sections, we are ready to discuss how a GRB triggered search is carried out with X-pipeline. Each GRB trigger consists of a sky location, time, and duration (T90). The data from each detector is time-shifted to account for the different GW arrival time according to the sky location of the GRB, and the T90

¹A data-stream recorded at the observatory other than the calibrated DARM signal.

is used to determine the *on-source* window for the GRBs. The on-source window is the time interval around the GRB time that is analyzed for candidate signals and depends on the expected time delay between the emission of the GW and GRB at the progenitor. Finally, the time-shifted on-source data is used to create time-frequency maps of the likelihood statistics which are clustered into events as described above. Data-quality vetoes and signal consistency tests are applied to these events and events which are not consistent with a real GW signal are vetoed. The surviving events are candidate gravitational wave events and the statistical significance of the events needs to be assigned.

As mentioned earlier, data from GW detectors often contains non-Gaussian glitches, or temporally non-stationary noise, which make it difficult to estimate the statistical properties of the detection statistic. Therefore, in order to claim whether a candidate gravitational wave event is statistically inconsistent with the noise background, the background is empirically estimated using nearby data. A sufficient block of data (usually three hours of data, which has been found to have similar noise characteristics) surrounding the GRB is divided into segments of the same length as the on-source and analyzed in the same way (these are called *off-source* segments). The off-source segments are assumed to not contain any gravitational wave signals; only background noise. The *loudest event statistic* [5, 69] is used to determine the significance of a GRB: the on-source event with the largest value of the detection statistic is compared to the cumulative distribution of loudest off-source events. The fraction of off-source events with greater or equal significance than the on-source event is interpreted as the *p-value* of that event. This p-value is an empirical measure of the probability of obtaining an event with the given significance from purely background noise (a significant GW detection

would have a small p-value). The threshold for “finding an interesting signal” can be set beforehand, usually at 1%.

In order to get p-values in the sub-1 percent range from 3 hours of background data, *time slides* are performed. Data from different detectors are artificially time shifted by amounts longer than the speed-of-light travel time, and the time shifted data are treated as background noise samples. In this way, the behavior of likelihood statistics on background noise is used to determine the statistical significance of a candidate event. As long as background noise is not correlated between detectors this is an effective and widely used method for evaluating the noise background of a network of GW detectors. However, correlated terrestrial noise influencing both detectors is not accounted for in this analysis of background noise. For this reason, there exists a network of physical environment sensors that monitors such noise sources and their coupling to the environment. This is described in more detail later in Chapter V.

Figure 4.4 shows an example of the foreground and background from an X-pipeline GRB analysis. The blue and red traces show the off-source events, while the green and pink traces correspond to the on-source. Many events do not pass consistency cuts and are discarded as can be seen going from the blue (green) trace to the red (pink) one. This figure illustrates the importance of data-quality vetos and coherent consistency cuts: the green and blue traces are before any of these cuts are applied and show large tails at high significance which totally cover the real signal present in the data. The red and pink traces are after the cuts are applied and are the relevant distributions when looking for signals. The presence of an event with high significance in the pink trace relative to the red trace indicates

the presence of a real signal in this example which comes from the analysis of GRB 170817A.

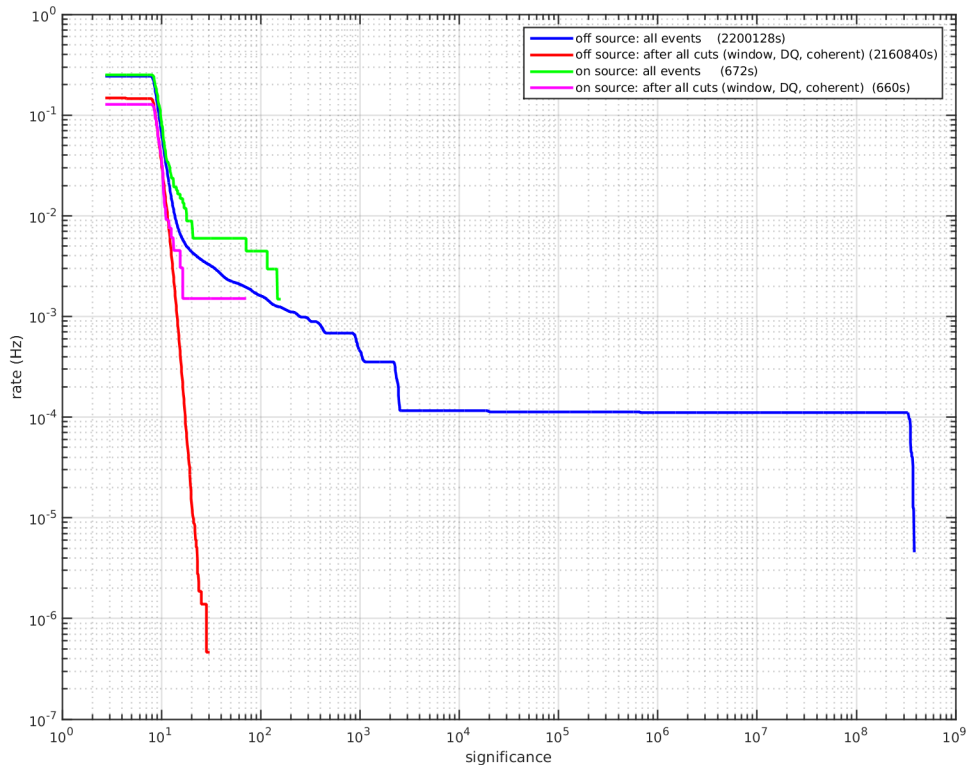


FIGURE 4.4. Event rates from the analysis of GRB 170817A. The blue (green) trace shows the off-source (on-source) data before any cuts are applied. The red and pink traces show the data after cuts have been applied.

4.2.5. Upper Limits and Tuning

X-pipeline also has a built in engine for adding simulated GW signals to the data. These *injections* are used to estimate the sensitivity of the search and tune the threshold for the consistency cuts in a so called *closed-box* analysis. The tuning and upper-limit calculation is automated in X-pipeline, so I will provide a brief overview of the process to understand how the results shown later were obtained.

To quantify the sensitivity of a search, X-pipeline will set an frequentist 90% upper limit on the h_{rss} of a gravitational wave signal present in the GRB on-source window. This is done separately for different waveform models and can therefore be translated into a distance model based on Equation 2.9 in chapter 2. The upper limit is calculated by injecting a large number of signals over a range of parameters such as peak time and signal strength then finding the value of h_{rss} for which 90% of the injections are recovered with a greater significance than the loudest surviving on-source event [69]. This is interpreted as a 90% chance such a signal would be found if it were present in the on-source window.

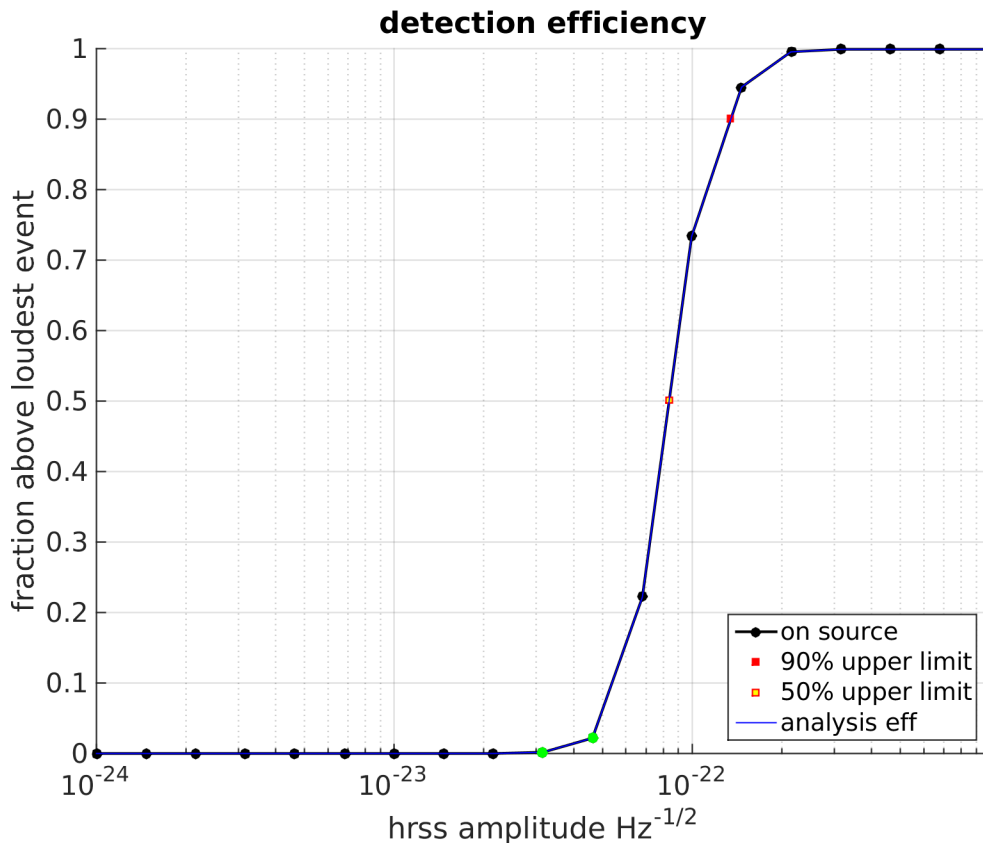


FIGURE 4.5. Fraction of injections recovered louder than most significant on-source event. In this example, 600 injections were used and the signal model was a circularly polarized sine-Gaussian with central frequency of 100Hz and a quality factor of 9. The precise 90% upper limit was obtained by interpolation.

Injections are also used to tune the coherent consistency cuts in X-pipeline. For example the E_{null}/I_{null} ratio discussed above is set based on the data to optimize the trade off between cutting out real signals (threshold too high) and allowing background noise through (threshold too low). The procedure, called a closed-box analysis, uses off-source data to test different values for thresholds and chooses the value that give the lowest upper limit for a single waveform model or averaged over a group of models. This is done automatically, without using on-source data so as not to bias the resulting upper limit. Looking at the final on-source results and upper-limits is then called “opening the box.”

The final result from running X-pipeline, then, is a p-value describing how likely the GW data in the GRB on-source window came from background noise and, in the no signal case, upper limits on h_{rss} for various signal models. If a population of GRBs are analyzed with X-pipeline, a trials factor should be applied to the p-values when interpreting the significance. The p-values can be combined to look for a possible population of sub-threshold GW signals in the GRB sample. This is done using noise-weighted binomial test [5] that considers the tail of low p-values from sample of analyzed GRBs.

4.3. O2 GRB Search

The O2 GRB search, published in Abbott et al. [10], used two search methods. One was an modelled search using a match-filter detection technique implemented in PyGRB [70, 71] that searched for binary neutron star or neutron star black hole signals from GRBs. I led the other search using X-pipeline as described in the previous section which searched for un-modelled transients. This section will describe the X-pipeline search in more detail and present the results.

4.3.1. GRB Sample

Collecting the sample of GRBs to search involves gathering information from the various locations where GRB satellites archive their data. The GRB sample contains events disseminated by the Gamma-ray Coordinates Network (GCN)², with additional information gathered from the Swift BAT catalog [72], the online Swift GRB Archive [73], Fermi Gamma-ray Burst Monitor (GBM) Burst Catalog [74, 75, 76], and the InterPlanetary Network (IPN) [77]. An automated system called VALID [78] cross-checks the time and localization parameters of the Swift and Fermi events against the published catalog with automated literature searches. In total, from November 2016 through August 2017, there were 242 bursts detected in the combined Swift + Fermi catalog. We received a total of 52 bursts localized by the IPN with many bursts appearing in both catalogs. GRBs that were poorly localized were removed from our sample, as were GRBs that did not occur during a period of stable, science-quality data taking by the available GW detectors.

Since the satellites observing GRBs have different abilities to localize the bursts, the size of the sky region to be searched within the O2 trigger catalog varies from sub 1° to many tens of degrees in radius. Here, I will discuss each GRBs observing mission and how their capabilities relate to the X-pipeline triggered search.

4.3.2. Fermi

The *Fermi* Gamma-Ray Space Telescope was launched in 2008 with a payload comprised of two science instruments: the Large Area Telescope (LAT) and the

²GCN Circulars Archive: http://gcn.gsfc.nasa.gov/gcn3_archive.html.

Gamma-Ray Burst Monitor (GBM). Fermi's main instrument, the LAT, is an imaging pair production telescope sensitive to high energy gamma rays above 20 MeV covering about 20% of the sky at a given time. The GBM consists of twelve sodium iodide scintillation detectors and two bismuth germanate detectors and is able to observe the entire unocculted sky in the energy range from 200 KeV to 40 MeV. It can promptly measure GRBs location, time history, and spectra which are all reported to follow up sites (including the LAT) in space and on the ground. Here, we are concerned with the GBM instrument, which has triggered on approximately two GRBs every three days since turning on and is responsible for the majority of the triggers used in LIGO followup searches.

GRB localizations from the GBM usually have a one-sigma error radius of about 10° associated with them. In addition to this statistical error reported by the GBM and recorded in VALID, there is a systematic error on the localizations as reported in Connaughton et al. [79]. This systematic error is modeled with two component Fisher distribution with a core of 3.7° and a tail of 14° , with 90% of localizations in the core and 10% in the tail. In constructing the grid to search over with X-pipeline, we take the quadratic sum of the statistical and systematic errors as the error radius and injections are distributed according to the same model.

4.3.3. Swift

The Neil Gehrels *Swift* Observatory, launched in November 2004, houses three instruments: the Burst Alert Telescope (BAT), the X-ray Telescope (XRT), and the Ultraviolet/Optical Telescope (UVOT). The observatory is able to provide afterglow observations of GRBs detected with the BAT by rapidly slewing the spacecraft towards the localization region. The BAT covers about 3 steradians of

the sky and uses a coded aperture mask to localize bursts with a resolution of a few arcminutes. For the purposes of GW searches with X-pipeline, triggers from Swift are analyzed as a single sky point since the Swift error is much smaller than intrinsic GW localization error.

4.3.4. IPN

The *Interplanetary Network* (IPN) is a group of satellites with onboard GRB detectors. Bursts are localized using the relative arrival time of GRBs for different satellites in the network. Depending on which satellites observed a particular burst and their spacial separation the localization region can vary from fractions to hundreds of square degrees or more. Figure 4.6 illustrates the principle behind localization with the IPN, whereby an annulus is constructed a pair of satellites, S_1 and S_2 , using equation

$$\cos \theta = c\delta t / D_{12}$$

where D_{12} is the distance between the satellites. The width of the annulus depends on the timing uncertainty and the distance between the satellites. For a network of three satellites, two independent annuloi can be determined and the final localization region is the intersection between them.

To run an X-pipeline search with a trigger from the IPN network, the timing information is combined with other constraints (such as occultation or a Konus ecliptic band) to form a 3σ localization region as described in Predoi et al. [80]. The discrete grid used by X-pipeline to search over is generated by paving the IPN error region with search points separated by 3.6° . An injection grid is generated by paving the search area with a much finer grid with a 0.2° spacing. This finer grid is used to generate injection points by randomly drawing locations within

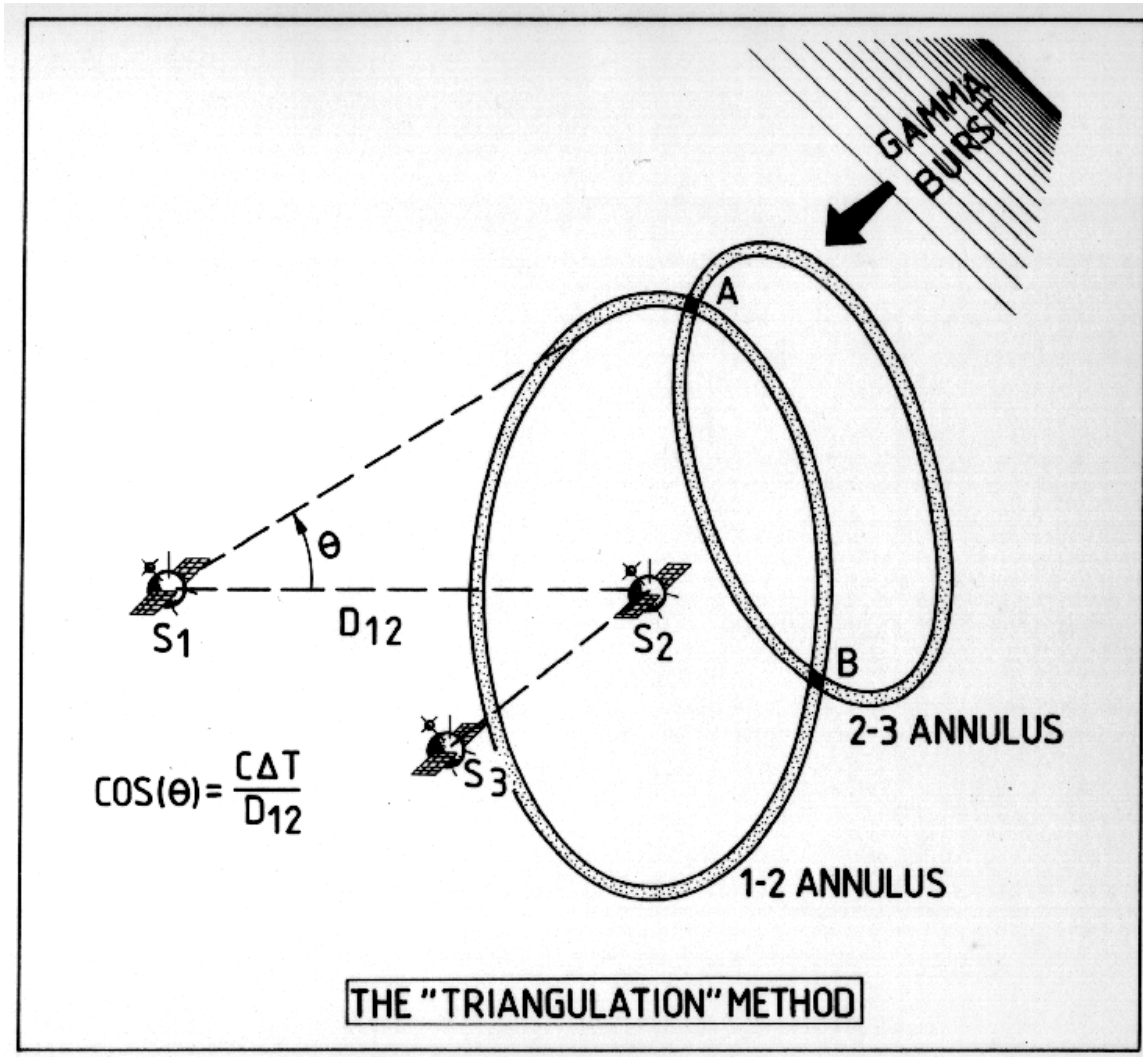


FIGURE 4.6. Triangulation of a GRB with the IPN network.
 From <http://www.ssl.berkeley.edu/ipn3/>.

boxes centered on these grid points with the number of injections in each box proportional to the source position probability distribution, which is taken to be a two-dimensional Gaussian with distances measured from the two central radii of the two intersection annuli.

In O2, the IPN burst list was received by the author via email from Kevin Hurley (who maintains the IPN catalog as of this writing) and checked for bursts where any gravitational wave data was available. The timing information from

each burst was subsequently received, and sky grids for the GW search were generated as described above. A total of 52 bursts localized by the IPN were created, although many bursts also appeared in the Swift/Fermi catalog. Many of these localizations were not used in the final analysis, such as bursts that were poorly localized, bursts whose error region was extremely long and narrow (when the annuli intersect at a grazing incidence), or bursts where the localization from the Fermi or Swift satellite alone was comparable or better to the IPN localization. Table 4.1 lists the GRBs localized with the IPN network.

TABLE 4.1. GRBs localized with timing data from the IPN during O2. Of the following IPN localizations eight of them were used for a GRB analysis with X-pipeline and reported in [10]. Many of these localizations were not used because, the error region was too large, did not improve over the Fermi or Swift localization previously available, or the region was too irregularly shaped.

Designation	Trigger (UTC)	T90 (s)	RA (°)	DEC (°)	Error (sq-deg)
GRB161203	18:41:08	5.5	162.20	-20.3	35.01
GRB161205	13:26:23	33	323.248	48.685	1478.92
GRB161217C	03:53:13	6.5	40.25	-18.4	1.85
GRB161218A	05:19:23	0.32	103.2	-10.1	0.34
GRB161218B	08:32:40	25.856	1.45	-16.2	0.58
GRB161222B	15:53:38	0.10	261.04	48.7	14985
GRB170114A	22:01:09	14.6	12.80	-11.8	2.54
GRB170121B	14:44:24	46.3	72.84	-12.65	1.78
GRB170202B	07:19:53	33	226.20	-41.3	1.84
GRB170206A [†]	10:51:57	1.2	213.18	12.58	0.63
GRB170208	13:16:37	53.7	285.20	1.14	1.98
GRB170210	02:48:11	71.4	226.06	-65.101	0.36
GRB170220	18:48:01	0.1	326.63	-55.890	194.76
GRB170222A [†]	05:00:59	1.6	292.97	28.07	0.28
GRB170306	14:07:27	18.9	153.00	51.71	1.56
GRB170308	05:18:06	11.5	214.76	-45.39	1.11
GRB170309	12:26:43	2.2	10.10	30.6	1.87
GRB170311 [†]	13:45:09	30	355.25	31.8	0.30

Table 4.1, *continued*

Designation	Trigger (UTC)	T90 (s)	RA (°)	DEC (°)	Error (sq-deg)
GRB170321	01:13:13	5	237.32	29.708	1749.68
GRB170323	07:52:55	70	292.66	20.41	43.02
GRB170422	08:14:04	25.3	174.62	7.19	71.786
GRB170424 [†]	10:12:06	53.2	343.04	-45.045	0.61
GRB170429	19:10:44	220	264.17	-20.25	3.64
GRB170601	08:24:17	308	286.76	22.48	137.30
GRB170606	05:37:05	85	0.0	0.00	2912.19
GRB170610	16:31:47	19.2	102.45	50.51	2.67
GRB170614A	11:39:54	28	213.87	42.12	2.64
GRB170614060557	06:05:57	122.60	98.49	8.12	49.26
GRB170618	11:24:41	52.5	177.30	12.3	2.47
GRB170702	19:27:12	0.54	150.00	-47.7	1040.09
GRB170703	08:44:03	34.5	208.60	0.50	1.90
GRB170710191254	19:12:54	6	157.90	45.52	28.09
GRB170712	03:20:30	21	174.70	14.12	90.58
GRB170726	03:46:32	17	26.68	9.45	193.14
GRB170802A	15:17:44	2.2	52.30	-39.2	0.17
GRB170803050715	05:07:15	12.50	67.66	-58.35	6.08
GRB170803B [†]	22:00:31	0.77	14.22	6.57	42.19
GRB170805A [†]	14:18:49	0.2	145.63	69.90	0.27
GRB170805B [†]	14:38:10	1	268.80	-23.5	0.21
GRB170806	19:34:02	12	0.0	0.0	5284.89
GRB170809 [†]	23:46:26	3.5	251.94	-17.56	1.26
GRB170811	06:06:40	12	304.97	-54.53	2046.20
GRB170816A	14:23:03	1.7	359.04	-24.54	18.05
GRB170817B	21:47:34	2.6	86.97	-42.49	13.15
GRB170820A	11:12:07	14.5	247.66	28.13	84.61
GRB170822	23:23:23	5.5	190.45	45.12	3086.19

[†] Was analyzed and reported in Abbott et al. [10].

4.3.5. GRB Classification

For the purposes of this work, GRBs are classified [as in 8] based on their T_{90} value – the period over which 90% of the flux was observed – and its uncertainty δT_{90} . GRBs with a value of $T_{90} + \delta T_{90} < 2$ s are *short*, and those with $T_{90} - \delta T_{90} > 4$ s are *long*. The remaining GRBs are *ambiguous*. As discussed in Chapter III, short GRBs are associated with binary neutron star mergers which have well modelled GW waveforms whereas long GRBs are associated with the collapse of massive stars which have GRB emission that is harder to model precisely.

The X-pipeline search was performed for all GRBs for which 660 s of coincident data was available from two GW detectors, regardless of classification. The modeled search for coalescing binary GW signals [70, 71] was performed for all short and ambiguous GRBs with at least 1664 s of data in one or more detectors. This scheme resulted in 98 GRBs being analyzed with our unmodeled method and 42 analyzed with our modeled method.

4.3.6. Running the X-pipeline search on the Caltech computing cluster

After collecting the sample of GRBs to analyze, the analysis can begin. All of the GRB parameters, such as peak time, T_{90} , and sky location, GW data including calibration and data-quality information, injection waveforms, and other information needs to be collated and passed to the X-pipeline software. The software runs on high-performance computing resources and expertise is required to diagnose any issues that may arise and ensure efficient completion of all computational jobs. The O2 X-pipeline GRB search took over 4 million CPU core hours of computing resources: I led the team responsible for launching, monitoring, and validating these computational jobs. This section goes into some of

the technical details required to reproduce the O2 X-pipeline search on the Caltech computing cluster.

First, the complete sample of GRBs occurring during the run must be checked against the available high-quality GW data available. There is a program in X-pipeline called `xnetworkselection.m` which takes a list of event times and on-source windows plus a list of science mode and veto segments. It applies network tests to determine which detectors satisfy the data quality criteria: namely no category 1 vetoes within 128 seconds of the GRB trigger time, less than 5% category 2 downtime during the on-source window, and no category 2 downtime within $[-5,+1]$ s of the GRB trigger time. To determine the available GW detector networks for GRBs in O2, the following command was run:

```
xnetworkselection H1L1V1 gps_trigs.txt time_offsets.txt \  
  ../data_segments/H1_science_cat1.txt None \  
  ../data_segments/L1_science_cat1.txt None \  
  ../data_segments/V1_science_cat1.txt \  
  ../data_segments/H1_cat24veto.txt None \  
  ../data_segments/L1_cat24veto.txt None \  
  ../data_segments/V1_cat24veto.txt \  
xnetworkselection_onsource.dat -600 60 16.0 704.0
```

The output file `xnetworkselection_onsource.dat` contains a single column indicating the network available to analyze each GRB. This column was added to the `o2_all.txt` containing all the data associated with each GRB with the following command:

```
paste xnetworkselection_onsource.dat o2_all.txt >  
  o2_catalog_networks.txt
```

To analyze each GRB the sample is divided according to which satellite(s) localized the burst, since the error regions differ significantly as discussed above, and according to the number of GW detectors available, since 2 and 3 detectors searches are run separately. Then, to get lists of GRBs from each satellite and with 2 or three GW detectors available the following commands were used (IPN bursts are handled separately):

```
grep -E 'H1L1.*Fermi' o2_catalog_networks.txt > 2det_fermi
grep -E 'H1L1.*Swift' o2_catalog_networks.txt > 2det_swift
grep -E 'H1L1V1.*Fermi' o2_catalog_networks.txt > 3det_fermi
grep -E 'H1L1V1.*Swift' o2_catalog_networks.txt > 3det_swift
grep 'H1\\|L1\\|V1' o2_catalog_networks.txt | \
grep -v 'H1L1\\|V1' > 1det
```

Once the lists of GRBs have been generated, the included script `xbatchgrb.py` is used to set up the directories and submission files needed to submit the X-pipeline GRB search to the cluster. `xbatchgrb.py` accepts a parameter file, GRB list, waveform catalog, among other parameters: importantly it takes a flag that indicates which satellite detected the GRB. In the case of a burst detected by Fermi, the error region is then inflated to account for the systematic error discussed in a previous section. Furthermore, a parameter can be set for using a line of sky points (along the line of constant time delay) instead of a grid to search over. This is used for 2-interferometer bursts where it has been demonstrated to reduce computational cost without losing sensitivity [81]. For example, the command used to run the 2 detector Fermi sample is:

```
xbatchgrb.py \
--params-file ./input/grb_offline_02_cleaned.ini \
```



```

--grb-list ./input/catalogs/2det_fermi \
--catalogdir ./input/waveforms/ \
--network-selection \
--detector H1 \
--detector L1 \
-t line \
--big-mem 2500 \
--long-inj \
--disable-fast-inj \
--fermiFlag

```

This sets up computational jobs for analyzing the GRB with X-pipeline: specifically, it prepares the many `xdetection.m` (which contains the search algorithm) computational jobs that need to be run to search over different sky positions, with various injections, and with time-slides. These `xdetection.m` jobs are the most computationally expensive part of the whole analysis, and is the step that takes the interferometer strain data and (after injecting signals, if requested, and conditioning the data) generates time-frequency maps for each likelihood type and clusters them into events, returning a list of events. These jobs are organized into a directed-analytic-graph (DAG) which represents the computations that need to be completed and their dependencies on other computations. The DAG is submitted to the computing cluster using a batch system known as Condor [82], using a command such as `condor_submit_dag $GRB_NAME.dag`. The scheduling and logging of these jobs are then handled by the Condor system, although the human analysts are often needed in case the computation does not finish correctly: temporary filesystem issues can cause data not to be found which will cause the

pipeline to fall over, although. Issues like that can be fixed with a simple re-submission of the DAG, although occasionally typos or bugs will necessitate more substantial investigations or re-running of the pipeline.

After the computationally expensive part of generating events, the post-processing step can be run. This is when the coherent vetoes, efficiency estimation, candidate identification, and upper limit calculation occur, as described previously in this chapter. In addition, a human-readable webpage is created summarizing the results of the pipeline. The script that sets up the jobs for a whole sample of GRBs is `xbatchgrbwebpage.py`, and for example was run for the O2 2-detector Fermi GRBs with the following parameters:

```
xbatchgrbwebpage.py \
  --parent-dir ~/GRB_02_cleaned/runs/Fermi/2det \
  --auto-dir ~/GRB_02_cleaned/post_processing \
  --web-dir ~/public_html/GRB_02_cleaned/Fermi/2det \
  --log-dir /local/jordan.palamos/log \
  --user-tag cleaned_fermi_2det \
  --veto-method alphaLinCutCirc \
  --percentile 99-99 \
  --add-stat powerlaw \
  --big-mem 8000 \
  --tuning-waveforms \
  sgc70q9~sgc100q9~sgc150q9~sgc300q9~bns~nsbh~adi-a~adi-b\
  ~adi-c~adi-d~adi-e
```

Once all of the post-processing jobs are finished, the analysis is essentially complete, and web pages for off-source data are automatically created. The webpages for each GRB should be checked for any indication something went wrong

with the analysis. For example an error in the input parameters, corrupted files, or poor data-quality at the time of the GRB could all require the analysis to be rerun. Two things to check when verifying that the analysis is behaving as expected is to ensure that fraction of injected signals recovered approaches 1 for large amplitude injections and there are not tails in the significance distribution after coherent cuts are performed. After verifying that the analysis performed well on off-source data, the command to generate a webpage containing on-source data (a process called ‘opening the box’) is: `condor_submit $GRB_NAME_openbox.sub`. At this point, one can look at the final result which will contain the p -value for the loudest event per GRB as well as h_{rss} upper limits for each waveform.

4.3.7. Search Results

98 GRBs were analyzed using X-pipeline in O2 and no significant events were found except for GRB 170817A which will be discussed in the following section. For the population of results we have compared the distribution of p -values against the expected distribution under the no-signal hypothesis, shown in Figure 4.7. We find a combined p -value of 0.75 looking at the most significant 5% of events from the unmodeled search using the weighted binomial test from Abbott et al. [5].

For GRBs other than GRB 170817A we use injections as described in section 4.2.5 to place 90% confidence level lower limits on the distance D_{90} assuming various emission models. We report results from two waveform families: circularly-polarized sine Gaussian (CSG) and accretion disk instability (ADI). CSGs are a generic model for GWs from a rotating quadrupolar mass distribution that could arise from rotational instabilities in the stellar collapse scenario. We try various central frequencies for the CSG models with a fixed Q factor of 9 (see equation

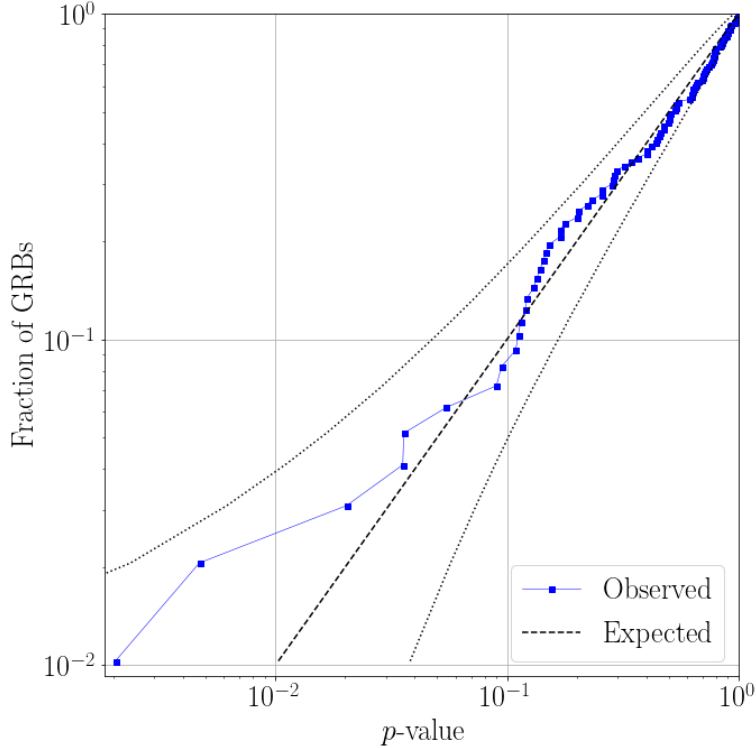


FIGURE 4.7. Cumulative distribution of p -values from the unmodeled search for transient GWs associated with 97 GRBs. GRB 170817A was removed. The dashed line represents the expected distribution under the no-signal hypothesis, with dotted lines indicating a 2σ deviation from this distribution. These results are consistent with the no-signal hypothesis, and have a combined p -value of 0.75 as calculated by a weighted binomial test [4, 5].

1 in [8]), and assume an optimistic radiated total energy of $E_{GW} = 10^{-2}M_{\odot}c^2$. ADI models [6, 7] refer to an extreme scenario for GW emission driven by strong coupling between a rapidly spinning black hole and a magnetically suspended disk. While the ADI models used here are unlikely to represent a realistic GW signal, they do capture the generic features of proposed emission models. The distribution of these lower limits for two of these models, ADI model A and a circular sine-Gaussian with central frequency of 150 Hz [8], are shown in Figure 4.8. These limits depend on detector sensitivity (which can vary over time), the detector

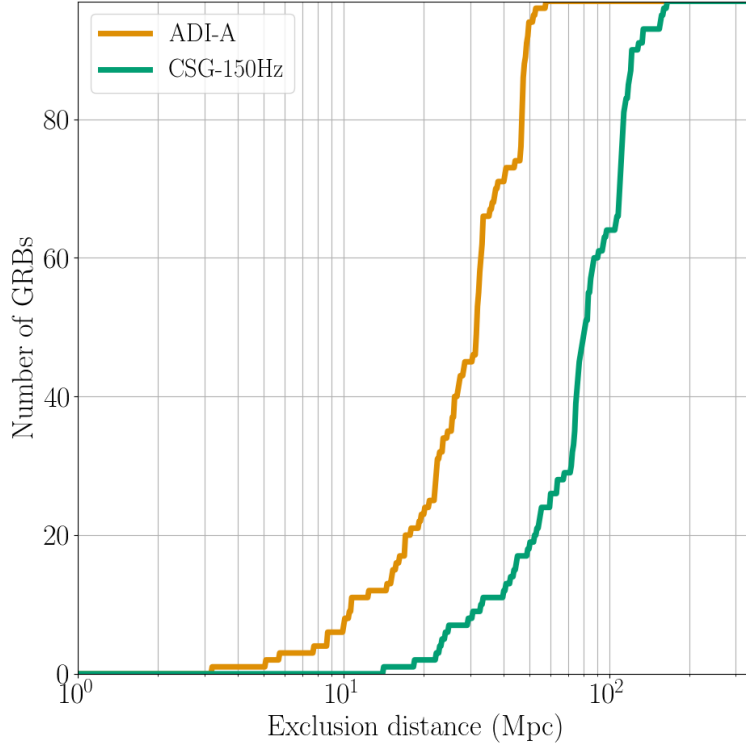


FIGURE 4.8. Cumulative histograms of the 90% confidence exclusion distances D_{90} for accretion disk instability signal model A [6, 7] and circular sine-Gaussian 150 Hz [8] model. For a given GRB and signal model this is the distance within which 90% of simulated signals inserted into off-source data are successfully recovered with a significance greater than the loudest on-source trigger. The median values for ADI-A and CSG-150 waveforms are 32 Mpc and 81 Mpc respectively.

antenna response for the GRB direction, systematic errors due to mismatch of a true GW signal and the waveforms used in simulations, as well as amplitude and phase errors from detector calibration. In Table 4.2 we provide population median exclusion limits for each model used, which vary from 15 Mpc to 113 Mpc.

The median D_{90} values, which vary from 15 Mpc to 113 Mpc across different model types, compare favorably with those from the first observing run, either increasing or staying the same depending on the specific signal model. In Table 4.3

TABLE 4.2. Median 90% confidence level exclusion distances, D_{90} , for the searches during O2. Modeled search results are shown for three classes of NS binary progenitor model, and unmodeled search results are shown for circular sine-Gaussian (CSG) [8] and accretion disk instability (ADI) [6, 7] models.

Modeled search (Short GRBs)	NS-BH		NS-BH	
	BNS	Generic Spins	Aligned Spins	
D_{90} [Mpc]	80	105	144	
Unmodeled search (All GRBs)	CSG	CSG	CSG	CSG
	70 Hz	100 Hz	150 Hz	300 Hz
D_{90} [Mpc]	112	113	81	38
Unmodeled search (All GRBs)	ADI	ADI	ADI	ADI
	A	B	C	D
D_{90} [Mpc]	32	104	40	15
				E
				36

we provide information on each GRB that was analyzed, including selected D_{90} results from both the PyGRB and X-Pipeline search where relevant.

Table 4.3: Information and limits on associated GW emission for each of the analyzed GRB. The Satellite column lists the instrument whose sky localization was used for the purposes of analysis. The Network column lists the GW detector network used in the analysis of each GRB – H1 = LIGO Hanford, L1 = LIGO Livingston, V1 = Virgo. A [†] denotes cases in which the on-source window of the generic transient search is extended to cover the GRB duration ($T_{90} > 60$ s). In cases where each analysis used a different network, parentheses indicate the network used for PyGRB analysis, and detail is provided in the table footnotes. Columns 8–12 display the 90% confidence exclusion distances to the GRB (D_{90}) for several emission scenarios: BNS, generic and aligned spin NSBH, ADI-A, and CSG GW burst at 150 Hz with total radiated energy $E_{\text{GW}} = 10^{-2} M_{\odot} c^2$.

GRB Name	UTC Time	R.A.	Dec.	Satellite(s)	Type	Network	D_{90} (Mpc)				
							BNS	NSBH ^k	NSBH ^l	ADI-A	CSG ^m
161207224	05:22:47	19 ^h 39 ^m 14 ^s	−9°56′	Fermi	Long	H1L1	–	–	–	8	40
161207813	19:31:22	3 ^h 55 ^m 09 ^s	15°44′	Fermi	Long	H1L1	–	–	–	26	73
161210524	12:33:54	18 ^h 52 ^m 28 ^s	63°03′	Fermi	Ambiguous	H1L1	61	72	112	19	49
161212652	15:38:59	01 ^h 39 ^m 36 ^s	68°12′	Fermi	Ambiguous	H1	49	59	60	–	–
161217128	03:03:45	14 ^h 26 ^m 31 ^s	51°59′	Fermi	Ambiguous	H1L1	65	85	122	18	56
170111815	19:34:01	18 ^h 03 ^m 31 ^s	63°42′	Fermi	Ambiguous	H1	95	160	198	–	–
170111A	00:33:27	1 ^h 22 ^m 45 ^s	−32°33′	Swift	Long	H1L1	–	–	–	13	78
170112A	02:01:59	1 ^h 00 ^m 55 ^s	−17°14′	Swift	Short	H1L1	83	106	144	32	79
170113A ^f	10:04:04	4 ^h 06 ^m 59 ^s	−71°56′	Swift	Long	H1L1	–	–	–	32	107
170121067	01:36:53	0 ^h 12 ^m 07 ^s	−75°37′	Fermi	Ambiguous	H1L1	79	105	144	26	73
170121133	03:10:52	16 ^h 07 ^m 57 ^s	13°49′	Fermi	Ambiguous	H1L1	96	142	172	23	88
170124238	05:42:12	19 ^h 26 ^m 57 ^s	69°37′	Fermi	Long	H1L1	–	–	–	25	72
170124528	12:40:29	00 ^h 43 ^m 24 ^s	11°01′	Fermi	Short	H1	65	101	116	–	–
170125022	00:31:14	17 ^h 36 ^m 34 ^s	28°34′	Fermi	Ambiguous	H1	46	52	57	–	–
170125102	02:27:10	23 ^h 57 ^m 38 ^s	−38°14′	Fermi	Short	H1L1(H1) ^a	30	39	63	20	51
170127067	01:35:47	22 ^h 37 ^m 19 ^s	−63°56′	Fermi	Short	H1L1	76	129	141	24	64
170127B	15:13:29	01 ^h 19 ^m 58 ^s	−30°20′	Swift	Short	H1	113	169	197	–	–
170130302	07:14:44	18 ^h 04 ^m 12 ^s	−29°07′	Fermi	Long	H1L1	–	–	–	48	121
170130510	12:13:48	20 ^h 35 ^m 00 ^s	1°26′	Fermi	Long	H1L1 [†]	–	–	–	26	68
170202A ^g	18:28:02	10 ^h 10 ^m 06 ^s	5°01′	Swift	Long	H1L1	–	–	–	47	113
170203486	11:40:25	16 ^h 20 ^m 21 ^s	−0°31′	Fermi	Short	H1L1	66	99	119	10	81
170203A	00:03:41	22 ^h 11 ^m 26 ^s	25°11′	Swift	Long	H1L1	–	–	–	38	112
170206A	10:51:58	14 ^h 12 ^m 43 ^s	12°34′	IPN	Short	H1L1	151	254	264	50	122
170208553	13:16:33	18 ^h 57 ^m 40 ^s	−0°07′	Fermi	Long	H1L1	–	–	–	31	64
170208A	18:11:16	11 ^h 06 ^m 10 ^s	−46°47′	Swift	Long	H1L1	–	–	–	50	134
170208B	22:33:38	8 ^h 28 ^m 34 ^s	−9°02′	Swift	Long	H1L1 [†]	–	–	–	32	77
170210116	02:47:36	15 ^h 04 ^m 14 ^s	−65°06′	Fermi	Long	H1L1 [†]	–	–	–	49	122
170212034	00:49:00	10 ^h 20 ^m 24 ^s	−1°29′	Fermi	Long	H1L1	–	–	–	29	76
170219002	00:03:07	3 ^h 39 ^m 21 ^s	50°04′	Fermi	Short	H1L1	171	251	304	52	159
170219110	02:38:04	5 ^h 14 ^m 45 ^s	−41°14′	Fermi	Long	H1L1	–	–	–	10	33

Table 4.3, *continued*

GRB Name	UTC Time	R.A.	Dec.	Satellite(s)	Type	Network	D_{90} (Mpc)				
							BNS	NSBH ^k	NSBH ^l	ADI-A	CSG ^m
170222A	05:00:59	19 ^h 31 ^m 53 ^s	28°04'	IPN	Short	H1L1	80	86	112	23	60
170302166	03:58:24	10 ^h 17 ^m 00 ^s	29°23'	Fermi	Ambiguous	H1L1	107	175	206	47	109
170304003	00:04:26	22 ^h 02 ^m 00 ^s	-73°46'	Fermi	Short	H1L1	105	143	178	34	85
170305256	06:09:06	2 ^h 34 ^m 38 ^s	12°05'	Fermi	Short	H1(L1) ^b	48	73	82	10	14
170306130	03:07:17	10 ^h 31 ^m 31 ^s	27°45'	Fermi	Long	H1L1	-	-	-	45	111
170310417	09:59:50	14 ^h 33 ^m 14 ^s	53°59'	Fermi	Long	H1L1	-	-	-	50	135
170310883	21:11:43	10 ^h 26 ^m 43 ^s	41°34'	Fermi	Long	H1L1	-	-	-	5	23
170311	13:45:09	23 ^h 43 ^m 48 ^s	33°24'	IPN	Long	H1L1	-	-	-	34	92
170311A	08:08:42	18 ^h 42 ^m 09 ^s	-30°02'	Swift	Long	H1L1	-	-	-	22	43
170317A	09:45:59	6 ^h 12 ^m 20 ^s	50°30'	Swift	Long	H1L1	-	-	-	33	80
170318A	12:11:56	20 ^h 22 ^m 39 ^s	28°24'	Swift	Long	H1L1 [†]	-	-	-	47	119
170318B	15:27:52	18 ^h 57 ^m 10 ^s	6°19'	Swift	Short	H1L1	152	254	281	48	112
170323058	01:23:23	9 ^h 40 ^m 45 ^s	-38°60'	Fermi	Long	H1L1	-	-	-	28	75
170325331	07:56:58	8 ^h 29 ^m 55 ^s	20°32'	Fermi	Short	H1L1	73	88	125	33	77
170330A	22:29:51	18 ^h 53 ^m 17 ^s	-13°27'	Swift	Long	H1L1 [†]	-	-	-	41	110
170331A	01:40:46	21 ^h 35 ^m 06 ^s	-24°24'	Swift	Long	H1L1	-	-	-	49	119
170402285	06:50:54	22 ^h 01 ^m 26 ^s	-10°38'	Fermi	Long	H1L1	-	-	-	9	110
170402961	23:03:25	20 ^h 31 ^m 40 ^s	-45°56'	Fermi	Long	H1L1	-	-	-	48	113
170403583	13:59:18	17 ^h 48 ^m 19 ^s	14°31'	Fermi	Short	H1L1	166	240	261	-	-
170403707	16:57:33	16 ^h 24 ^m 09 ^s	41°49'	Fermi	Long	H1L1	-	-	-	24	54
170409112	02:42:00	23 ^h 10 ^m 19 ^s	-7°04'	Fermi	Long	H1L1 [†]	-	-	-	20	106
170414551	13:13:16	2 ^h 54 ^m 00 ^s	75°53'	Fermi	Long	H1L1	-	-	-	33	80
170416583	14:00:05	18 ^h 56 ^m 52 ^s	-57°01'	Fermi	Long	H1L1 [†]	-	-	-	9	24
170419983	23:36:14	17 ^h 39 ^m 28 ^s	-11°14'	Fermi	Long	H1L1	-	-	-	49	119
170419A	13:26:40	5 ^h 19 ^m 25 ^s	-21°26'	Swift	Long	H1L1	-	-	-	48	114
170422343	08:13:54	12 ^h 34 ^m 31 ^s	16°49'	Fermi	Long	H1L1	-	-	-	47	114
170423719	17:15:08	22 ^h 57 ^m 21 ^s	-4°16'	Fermi	Long	H1L1	-	-	-	36	98
170423872	20:55:23	13 ^h 58 ^m 24 ^s	26°22'	Fermi	Long	H1L1	-	-	-	17	45
170424	10:12:06	10 ^h 00 ^m 40 ^s	-13°41'	IPN	Long	H1L1	-	-	-	32	75
170424425	10:12:30	22 ^h 54 ^m 07 ^s	-45°12'	Fermi	Long	H1L1	-	-	-	32	74
170428136	03:16:17	0 ^h 19 ^m 02 ^s	56°14'	Fermi	Long	H1L1	-	-	-	23	75
170428A ^h	09:13:42	22 ^h 00 ^m 12 ^s	26°55'	Swift	Short	H1L1	105	167	178	32	86
170430204	04:54:20	01 ^h 35 ^m 26 ^s	30°07'	Fermi	Short	H1	32	54	81	-	-
170501467	11:11:53	6 ^h 28 ^m 02 ^s	13°43'	Fermi	Long	H1L1	-	-	-	34	84
170506169	04:02:48	7 ^h 29 ^m 02 ^s	51°52'	Fermi	Ambiguous	H1L1	103	174	149	36	84
170604603	14:28:05	22 ^h 41 ^m 36 ^s	40°42'	Fermi	Short	L1	131	204	237	-	-
170610689	16:31:47	4 ^h 35 ^m 38 ^s	46°29'	Fermi	Long	H1L1	-	-	-	53	162
170611937	22:29:35	11 ^h 34 ^m 19 ^s	-7°22'	Fermi	Long	H1L1	-	-	-	32	75

Table 4.3, *continued*

GRB Name	UTC Time	R.A.	Dec.	Satellite(s)	Type	Network	D_{90} (Mpc)				
							BNS	NSBH ^k	NSBH ^l	ADI-A	CSG ^m
170614255	06:06:41	4 ^h 42 ^m 12 ^s	37°56′	Fermi	Long	H1L1 [†]	–	–	–	22	55
170614505	12:06:39	20 ^h 43 ^m 58 ^s	–37°54′	Fermi	Ambiguous	H1	9	22	0	–	–
170616165	03:58:07	3 ^h 18 ^m 02 ^s	19°40′	Fermi	Long	H1L1 [†]	–	–	–	34	95
170618475	11:24:41	0 ^h 59 ^m 19 ^s	26°44′	Fermi	Long	H1L1	–	–	–	48	130
170625692	16:35:47	7 ^h 06 ^m 48 ^s	–69°21′	Fermi	Long	H1L1	–	–	–	33	84
170626A	09:37:23	11 ^h 01 ^m 37 ^s	56°29′	Swift	Long	H1L1	–	–	–	33	82
170629A	12:53:33	8 ^h 39 ^m 50 ^s	–46°35′	Swift	Long	H1L1	–	–	–	48	117
170705200	04:48:30	23 ^h 58 ^m 02 ^s	–21°56′	Fermi	Long	H1L1	–	–	–	29	74
170705244	05:50:45	15 ^h 50 ^m 26 ^s	–7°26′	Fermi	Long	H1L1	–	–	–	32	86
170705A ⁱ	02:45:47	12 ^h 46 ^m 50 ^s	18°18′	Swift	Long	H1L1 [†]	–	–	–	47	156
170708046	01:06:11	22 ^h 13 ^m 00 ^s	25°37′	Fermi	Short	L1	57	105	103	–	–
170709334	08:00:24	20 ^h 40 ^m 10 ^s	02°12′	Fermi	Ambiguous	L1	139	228	255	–	–
170714A ^j	12:25:32	2 ^h 17 ^m 17 ^s	1°58′	Swift	Long	H1L1 [†]	–	–	–	48	123
170715878	21:04:13	19 ^h 08 ^m 52 ^s	–16°37′	Fermi	Long	H1L1	–	–	–	47	114
170723076	01:49:10	9 ^h 03 ^m 45 ^s	–19°26′	Fermi	Long	H1L1	–	–	–	26	75
170723677	16:15:27	1 ^h 28 ^m 16 ^s	62°41′	Fermi	Long	H1L1	–	–	–	37	111
170723882	21:10:18	14 ^h 10 ^m 19 ^s	39°50′	Fermi	Ambiguous	H1L1	95	83	179	40	110
170724A	00:48:44	10 ^h 00 ^m 14 ^s	–1°02′	Swift	Long	H1L1 [†]	–	–	–	21	84
170726249	05:58:15	11 ^h 05 ^m 40 ^s	–34°00′	Fermi	Ambiguous	H1L1	124	152	207	38	112
170728A	06:53:28	3 ^h 55 ^m 36 ^s	12°10′	Swift	Short	H1L1	89	129	163	26	81
170731751	18:01:39	16 ^h 20 ^m 48 ^s	64°18′	Fermi	Long	H1L1 [†]	–	–	–	17	44
170802638	15:18:24	3 ^h 29 ^m 12 ^s	–39°13′	Fermi	Ambiguous	H1L1V1	45	62	72	3	24
170803172	04:07:15	5 ^h 06 ^m 00 ^s	23°60′	Fermi	Ambiguous	H1L1(H1L1V1) ^c	56	83	105	16	53
170803B	22:00:32	00 ^h 56 ^m 53 ^s	06°34′	IPN	Short	L1 ^d	140	215	234	–	–
170804A	12:01:37	0 ^h 25 ^m 37 ^s	–64°47′	Swift	Long	H1V1 [†]	–	–	–	15	45
170805901	21:37:49	16 ^h 15 ^m 52 ^s	36°23′	Fermi	Long	H1V1	–	–	–	11	25
170805A	14:38:10	20 ^h 50 ^m 26 ^s	22°28′	IPN	Short	H1L1V1	69	100	114	22	61
170805B	14:18:49	8 ^h 40 ^m 32 ^s	70°06′	IPN	Short	H1L1V1	132	163	218	33	114
170807A	21:56:09	9 ^h 33 ^m 44 ^s	–17°21′	Swift	Long	H1L1	–	–	–	27	76
170808065	01:34:09	0 ^h 13 ^m 12 ^s	62°18′	Fermi	Ambiguous	L1V1	58	83	87	11	18
170808936	22:27:43	9 ^h 42 ^m 38 ^s	2°11′	Fermi	Long	L1V1	–	–	–	22	41
170809	23:46:26	16 ^h 52 ^m 37 ^s	–12°18′	IPN	Long	H1L1V1	–	–	–	27	87
170816258	06:11:11	0 ^h 42 ^m 48 ^s	–15°37′	Fermi	Long	H1L1 [†]	–	–	–	17	55
170816599	14:23:03	23 ^h 25 ^m 36 ^s	19°06′	Fermi	Short	H1L1V1(H1V1) ^e	46	56	73	15	34
170817908	21:47:34	5 ^h 32 ^m 07 ^s	50°04′	Fermi	Ambiguous	H1V1	35	51	63	16	30
170817A	12:41:06	13 ^h 09 ^m 36 ^s	–23°24′	Fermi	Ambiguous	H1L1V1	N/A	N/A	N/A	N/A	N/A
170818137	03:17:20	19 ^h 48 ^m 53 ^s	06°21′	Fermi	Ambiguous	H1L1	103	146	169	–	–
170821265	06:22:00	16 ^h 51 ^m 26 ^s	19°07′	Fermi	Long	H1L1 [†]	–	–	–	33	76

Table 4.3, continued

GRB Name	UTC Time	R.A.	Dec.	Satellite(s)	Type	Network	D_{90} (Mpc)				
							BNS	NSBH ^k	NSBH ^l	ADI-A	CSG ^m
170822A	09:11:51	6 ^h 17 ^m 29 ^s	54°60′	Swift	Long	H1L1V1 [†]	–	–	–	32	97
170823A	22:16:48	12 ^h 34 ^m 51 ^s	35°33′	Swift	Long	H1L1 [†]	–	–	–	58	166
170825307	07:22:01	18 ^h 17 ^m 36 ^s	–26°12′	Fermi	Long	L1V1	–	–	–	15	31
170825500	12:00:06	0 ^h 14 ^m 33 ^s	20°07′	Fermi	Long	H1L1	–	–	–	47	116
170825784	18:49:11	7 ^h 45 ^m 16 ^s	–48°43′	Fermi	Long	H1L1V1 [†]	–	–	–	6	22

^a GRB 170125102 occurred when the Livingston detector was not in its nominal observing state, however the data was deemed suitable for the purposes of the unmodeled analysis.

^b GRB 170305256 occurred near the null of the Hanford detector and inclusion of its data did not aid the PyGRB search sensitivity compared to a Livingston-only analysis.

^c GRB 170803172: Virgo data did not meet the data quality requirements of **X-Pipeline**.

^d GRB 170803B occurred near the null of the Virgo detector (see note *b*). In addition, Livingston data did not meet the data quality requirements of **X-Pipeline**, so this GRB was not subject to the unmodeled analysis.

^e GRB 170816599 occurred near the null of the Livingston detector (see note *b*).

^f GRB 170113A has redshift of $z = 1.968$ [83].

^g GRB 170202A has redshift of $z = 3.645$ [84].

^h GRB 170428A has redshift of $z = 0.454$ [85].

ⁱ GRB 170705A has redshift of $z = 2.01$ [86].

^j GRB 170714A has redshift of $z = 0.793$ [87].

^k NS-BH with generic spins

^l NS-BH with aligned spins

^m Circularly-polarized sine-Gaussians with a central frequency of 150 Hz

4.3.8. GRB 170817A

The GRB that deserves special mention here, of course, is GRB 170817A which has been associated with a binary neutron star merger and followed up extensively as described in the previous chapter. It was the only GRB in the O2 sample analyzed by X-pipeline that could be considered a detection, with a p -value of 3.1×10^{-4} in this search. For comparison, PyGRB returned a p -value of $<9.38 \times 10^{-6}$ for this GRB: as expected for a real BNS signal, the search modelled as a BNS returned a more significant result. An older X-pipeline analysis that used different search parameters gave a p -value of 1.3×10^{-5} and was reported in Abbott et al. [2]. Here, we describe the differences between the two searches that gave rise to the different p -values between two different X-pipeline analyses of GRB 170817A.

First, the data used were slightly different between each analysis. The newer analysis used *cleaned* data where the large glitch overlapping the signal was subtracted using the algorithm described in Pankow et al. [88] and various other noise sources have been subtracted as described in Davis et al. [89]. At the time of the original analysis, these cleaning techniques were not yet developed and the only cleaning applied was *gating* the large glitch. These changes did not seem to greatly affect the final results, since the noise that was cleaned by these methods was already rejected by the consistency cuts in X-pipeline. One setting that was changed between the two analyses was the clustering window. The binary neutron star signal from GRB 170817A was spread out over a much longer time period than the typical signal considered with X-pipeline. Each individual pixel of the signal does not necessarily stand out above the clustering threshold, so the true signal is clustered into multiple events comprising different parts of the time-frequency

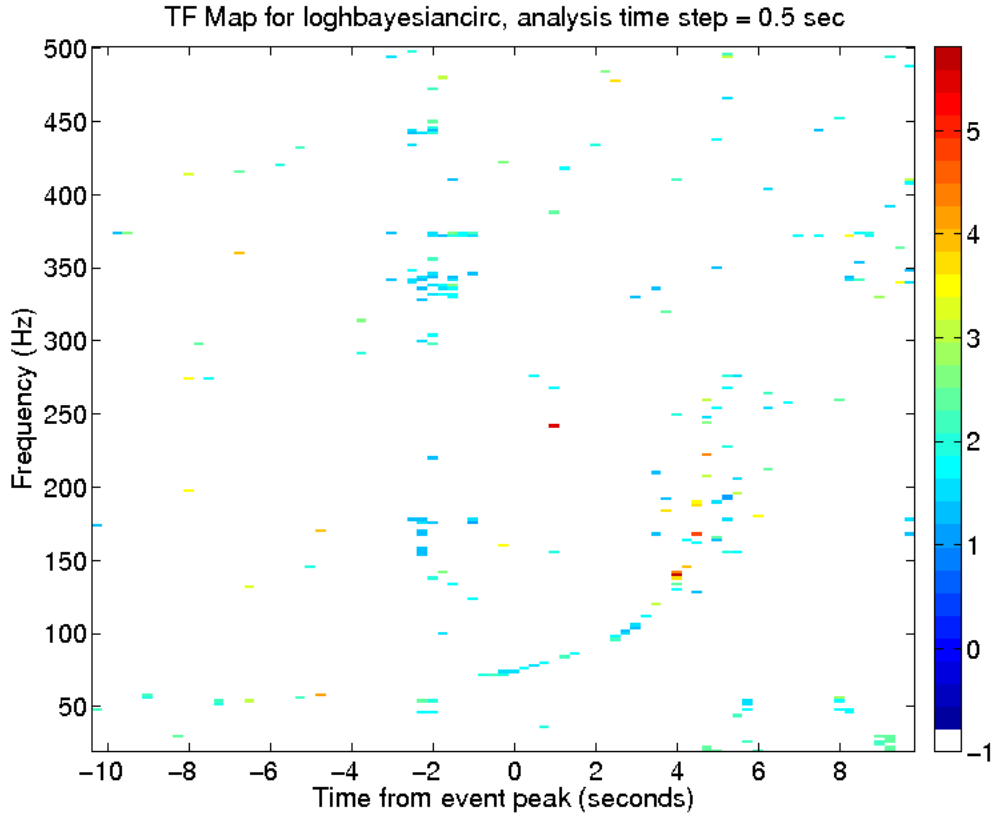


FIGURE 4.9. New time-frequency map of the detection statistic for GRB 170817. Pixels below the threshold have been set to white. Clusters are made by combining each pixel with any surrounding eight pixels. The loudest cluster consists of 9 pixels between 70 Hz and 80 Hz at $t = 0$. That cluster is a portion of the BNS signal that chirps upwards from about 50 Hz to over 200 Hz just after 4 s on this plot.

path. The older analysis used a generalized approach that clustered events with a 7 by 7 pixel large window. This approach is more sensitive to signals spread out in time, at the cost of potentially clustering noise pixels together as well. The newer analysis presented here used the nearest 8 pixels to cluster events, in order to be consistent with the rest of the O2 GRB sample. The clustering approach used by the older analysis is more sensitive to BNS signals which explains the higher significance from that analysis. Figure 4.9 shows the time-frequency map from

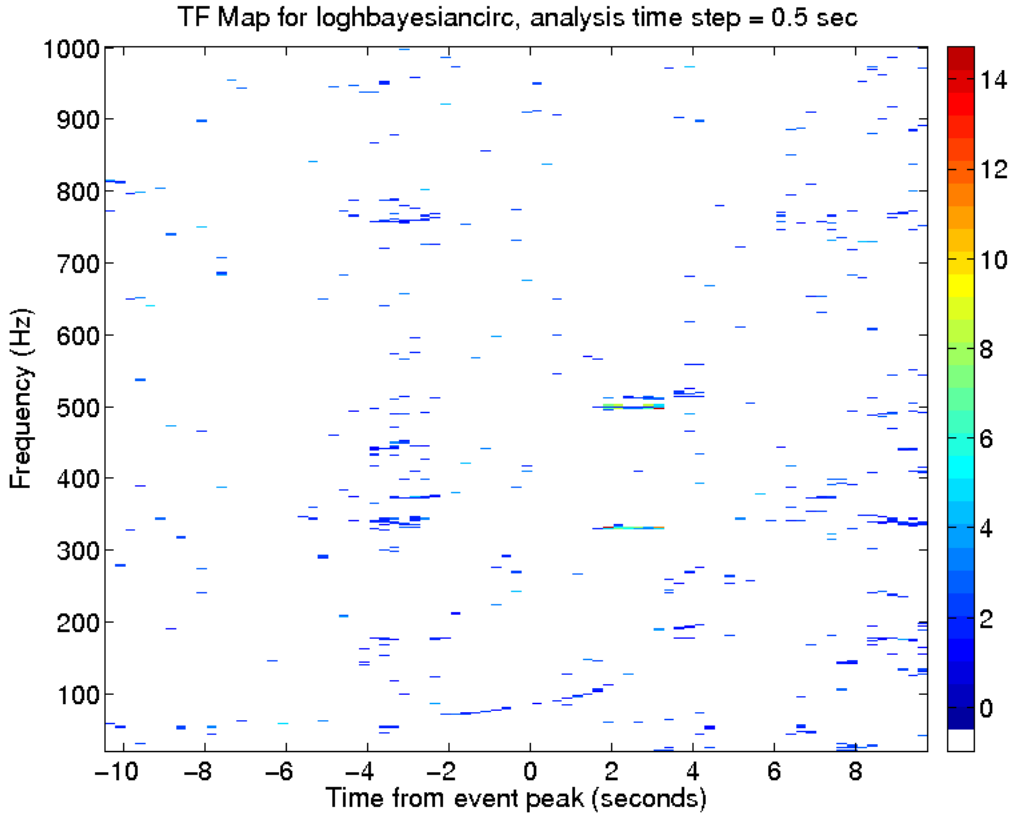


FIGURE 4.10. Old time-frequency map of the detection statistic for GRB 170817. Pixels below the threshold have been set to white. Clusters are made by combining each pixel with any surrounding eight pixels. The loudest cluster consists of 9 pixels between 70 Hz and 80 Hz at $t = 0$.

the new analysis. The loudest event consists of 9 pixels between 70 Hz and 80 Hz at $t = 0$ and can be compared with the older result where the loudest event is a cluster where the pixels are not actually touching (Figure 4.10).

Both analyses used the sky location reported by the Fermi GBM. The sky localization region was not very precise, since the GRB was quite dim, and had a 90% confidence region that covered 1100 sq-deg. Although the location of GRB 170817 is now known very precisely, both analyses used the GBM data, which provides a better comparison to the rest of the O2 sample.

The detection of GRB170817A by the burst pipeline gives us confidence that a significant GW signal from a GRB is detectable even if we do not have good a priori knowledge of the emission model.

4.4. O3 GRBs

GRBs detected during the O3 run are currently being analyzed with X-pipeline and PyGRB. I have analyzed over 50 GRBs from the first part of O3 and these results will be included in a paper that is currently in preparation. In addition to running the X-pipeline software package on these GRBs, a new feature was added to the pipeline that can remove glitches from the data prior to analysis. The motivation for and implementation of this method, which has been applied to some O3a GRBs, is presented here.

4.4.1. Improving the search by excising glitches from the data stream (gating)

Short bursts of instrumental noise, known as glitches, are common in the aLIGO data and are known to affect detection pipelines. Two strategies mentioned so far to deal with glitches include data-quality flags, where data that are known to be contaminated with instrumental noise are excluded from an analysis, and coherent cuts where candidate GW events are discarded because they are more similar to a single detector glitch than a coherent signal. However, there is another approach that can be used to deal with the short-in-time loud glitches that are common in the aLIGO data. This approach is known as gating—and is a subtle departure from the data-quality veto approach. Whereas a traditional data quality veto will either throw away all data that may be contaminated (in the CAT1

definition described above) or throw out all triggers during a time segment (CAT 2), the gating approach still uses nearby data and may allow recovery of a signal that overlaps with a glitch.

A well known example of this is the loud glitch present during GW 170817 in the Livingston datastream [9]. Figure 4.11 shows the Livingston data with the glitch at the time of GW170817, and shows a technique to model and subtract the glitch. However, at the time multiple approaches were used, and instead of modelling and subtracting the glitch, the X-pipeline analysis used a simpler method: gating. The data around the time of the glitch was multiplied by a window function that smoothly went from one to zero and back, effectively zeroing out the data around the glitch. This gating method has proven to be a simple and reliable method to remove short glitches. This section will describe the motivation for, implementation, and performance of a new feature in X-pipeline that can easily apply gating on-the-fly when analyzing GRBs.

While the coherent cuts in X-pipeline are able to reliably reject glitches that could otherwise masquerade as signals, glitches still have a subtle negative affect on the pipeline's ability to estimate it's sensitivity. The main advantage with gating short glitches is that you still use the nearby data: injections and real signals that overlap with the data can still be recovered. Injected signals (especially long duration signals) for tuning cuts and estimating sensitivity will likely overlap with any glitch present in the on-source window. The whole cluster will then contain both a simulated signal and a single detector glitch, and will likely fail the coherent consistency cuts. The recovery of these injections is desirable, and constitutes a useful check on the efficacy of the pipeline to find real signals. Therefore, the following method was implemented for users of X-pipeline to remove these glitches.

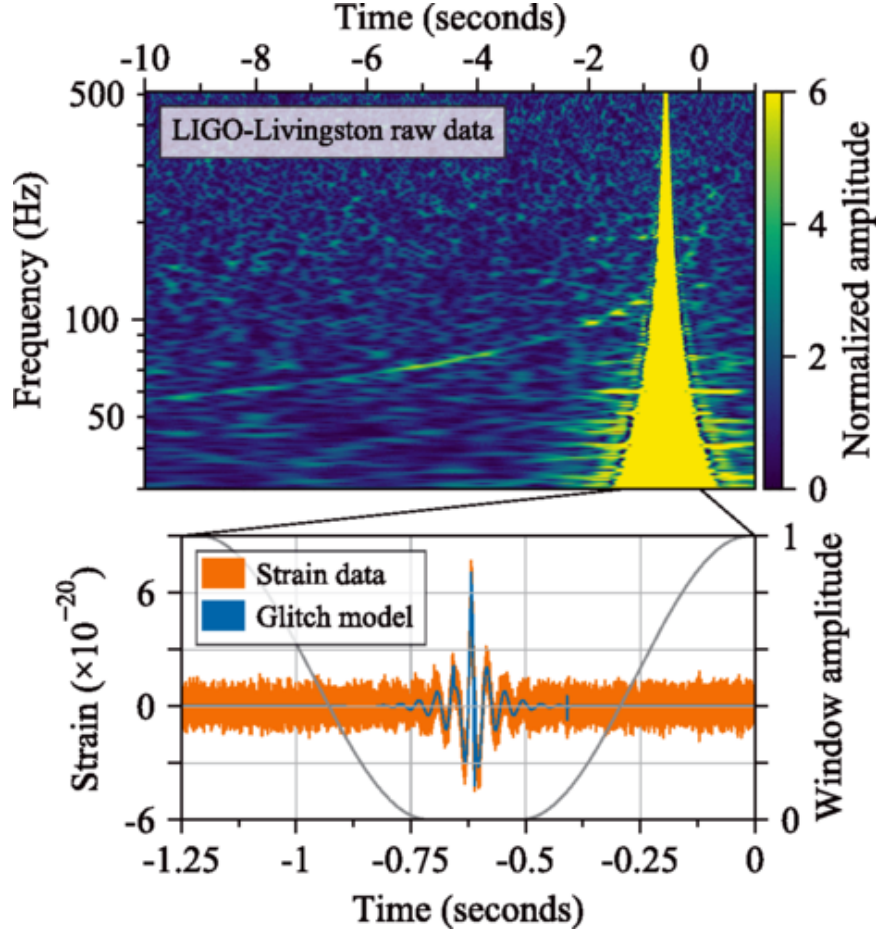


FIGURE 4.11. Time-frequency representation of the GW170817 signal from Livingston. The raw data is shown in the top panel and a large instrumental glitch is easily visible on top of the BNS signal track. The BNS coalescence falls at 0.4 s in this figure, and the glitch occurs 1.1 s before that time. The bottom panel shows the time domain data, where the glitch was modelled so that it could be subtracted. Figure reproduced from Abbott et al. [9].

The method for gating is to simply multiply the data by a smoothly varying window function that is equal to zero where the data is contaminated by a glitch and goes to unity on either side. This way, the glitch is totally removed from the data with less spectral leakage compared to a rectangular window. The window function used is one minus a Tukey window. The gating is applied in the data conditioning part of X-Pipeline, after high passing the data and before The user

must specify the window parameters and glitch times when running the pipeline. Glitches that get removed this way should still be systematically chosen from known instrumental artifacts, however, since only zeroing out certain problematic times where there is excess noise would bias the final results.

A simplified version of the MATLAB code that applies the gates is included below.

```

% ---- Loop over detectors.
for ii = 1:numberOfChannels
    currDetector = gateList{ii};
    % ---- Loop over gates for this detector.
    for jj = 1:length(currDetector(:,1))
        centerSample = round(currDetector(jj,1)); %-- force to be
            an integer
        zeroTime      = currDetector(jj,2);
        taperTime     = currDetector(jj,3);
        % ---- Make window. Force the length of the window to be
            an
        %      even number.
        alpha = taperTime/(zeroTime+taperTime);
        windowSamples = 2*round(sampleFrequency*(zeroTime+
            taperTime)/2);
        window = 1 - tukeywin(windowSamples, alpha);
        samplesBefore = centerSample - windowSamples/2;
        samplesAfter  = length(data) - centerSample -
            windowSamples/2;
        % ---- Construct and apply the full gating window.
        gateVect = [ones(samplesBefore,1); window; ones(
            samplesAfter,1)];
        data(:,ii) = data(:,ii).*gateVect;
    end
end
end

```

This approach was tested and shown to work with a few X-pipeline GRB analyses from O2. The GRB 170817A analysis, for example, was rerun using this approach and verified to give the same result as when the analyst made a gated data-set ‘by hand’ and fed it into X-pipeline. Another burst reported in the O2

GRB search above, GRB 170402, was found to have short glitches in the on-source region that could potentially benefit from this approach. Time-frequency representations of two short glitches in the Hanford data are shown in Figure 4.12.

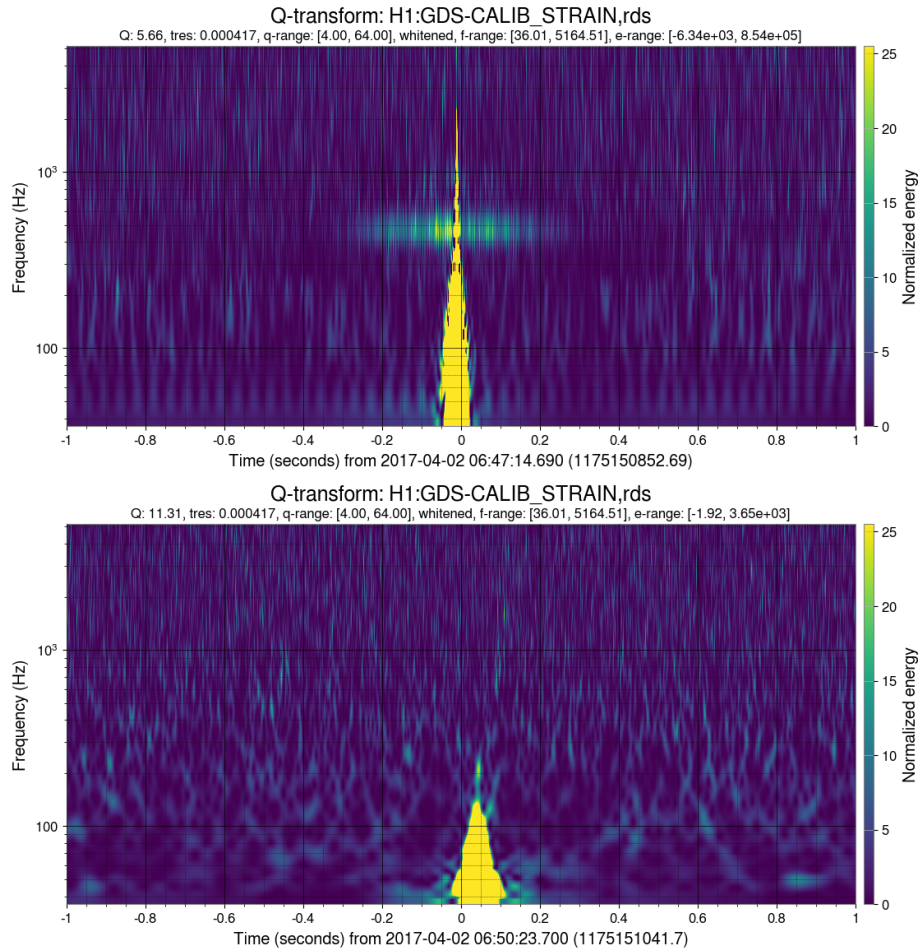


FIGURE 4.12. Time-frequency representations of two glitches from the analysis of GRB 170402. When these glitches were removed using the gating method, the recovery of injected signals with X-pipeline was improved.

While the X-pipeline coherency requirements were able to remove these glitches as event candidates, injections that overlapped with them were also removed, causing many injections to not be recovered. Verifying the recovery of these injections is an important check when deciding if an X-pipeline analysis is suitable for publication, not to mention the fact that a real signal could be rejected.

When these glitches were removed using the gating approach described in this section, recovery of injected signals was improved, as expected. Figure 4.13 shows how the recovery of injected signals was affected by using the gating approach to remove glitches during the analysis of GRB 170402. This shows that this new, flexible addition to X-pipeline can help future analyses search for signals in the presence of loud short glitches.

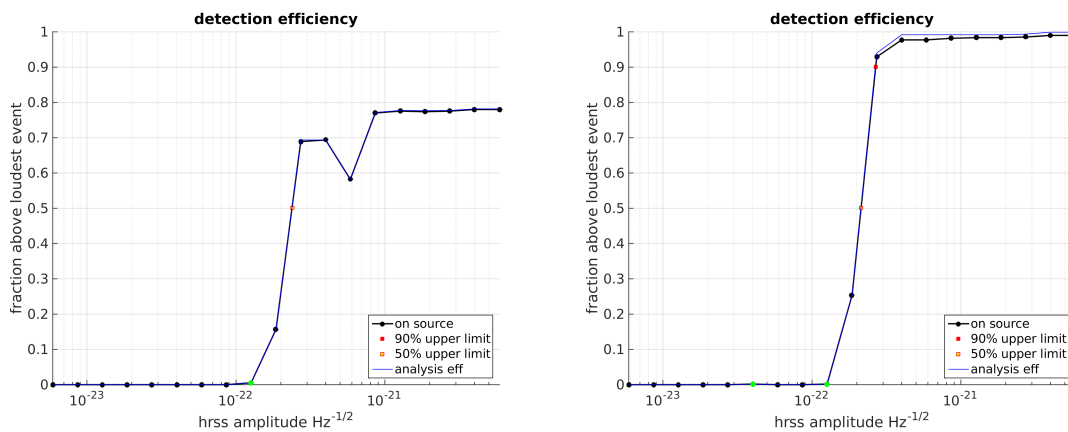


FIGURE 4.13. Detection efficiency curves for ADI-D waveforms in the X-pipeline analysis of GRB 170402. The left panel shows the analysis before gating two glitches in the Hanford data, the presence of these glitches caused many injections to be rejected by coherency requirements. When the data around those glitches are zeroed out, the injections can again be recovered by the pipeline

4.4.2. Low Latency Online Search

Many of the scientific discoveries enabled by gravitational wave detection also depend on crucial observations in the electromagnetic spectrum, as discussed earlier in this dissertation. Much effort has been put into building infrastructure that enables timely communication between gravitational wave astronomers and conventional astronomers. The LIGO-Virgo collaboration sends electronic notices

and circulars in the GCN announcing potential GW signals (see [90]) and also maintains a online candidate event database, called GraceDB [91]. For example, see Abbott et al. [92] for an overview of low-latency GW alerts and their EM followup during O2.

The coherent GRB follow-up searches, such as the X-pipeline and PyGRB search described earlier in this dissertation, have historically been published in an *offline* mode with latencies of months or years from GRB detection to publication of the final GW search results. However, these pipelines can also run in an online mode: they can be launched automatically as soon as a GRB is discovered with search parameters optimized to return a result quickly rather than give precise distance limits to the source. The reduction in latency of these alerts is important because other astronomical observations may become impossible as time passes and transient electromagnetic signals fade. For example, while optical GRB afterglow light curves have a diversity of morphologies [93], their fading nature makes detection less likely ~ 0.1 days after the GRB [94]. Therefore, knowing the probability of GW emission and preliminary distance upper limits to GW sources associated with a particular GRB on the timescale of hours could help inform observers when deciding what resources to devote toward the followup of that GRB.

To that end, computer programs have been developed that autonomously listen for GRB alerts, launch coherent GW pipelines, and report results including the false-alarm-rate of any GW candidate and distance upper limits. These programs are known as the GRB *medium latency followup* codes and consist of perl and python scripts that can automatically handle those tasks including the launching and monitoring of jobs on the LIGO Scientific Collaboration (LSC)

computing clusters (a process that usually takes much human effort to complete). While these codes were mostly developed prior to my involvement, I aided in their development and took over responsibility for maintaining, running, and reporting their results during the O3 period. I was responsible for getting these codes reviewed internally by the LSC so that their output could be approved for public release. When O3 was prematurely suspended due to COVID-19 the medium latency GRB pipeline had just been approved to publicly report its results; it is now planned to be in operation during the upcoming O4 run. The rest of this section contains a description of the main scripts and some technical details about running the pipeline.

A repository containing the medium latency code can be found at <https://git.ligo.org/emfollow/medium-latency-followup>³. Figure 4.14 shows the design of the medium latency code: each node is a perl or python script that handles a part of the pipeline and they rely on a shared directory structure with text files to communicate between processes. The important pieces are as follows, each is a perl script although many rely on python subroutines that are called along the way:

- `queryGraceDB` checks GraceDB for GRB events reported by the Fermi and Swift satellites and dumps the data for each burst into a text file. It queries GraceDB for new events every 5 minutes by default.
- `XprocessGRB` checks the file containing GRB data for new entries, and if there is a new GRB attempts to launch X-pipeline after validating things like data segments, sky error, and data quality. It calls the python script `grb.py` from the X-pipeline package to create the search workflow, then launches the job

³Valid LIGO.ORG credentials are required to view this site

Online GRB processor

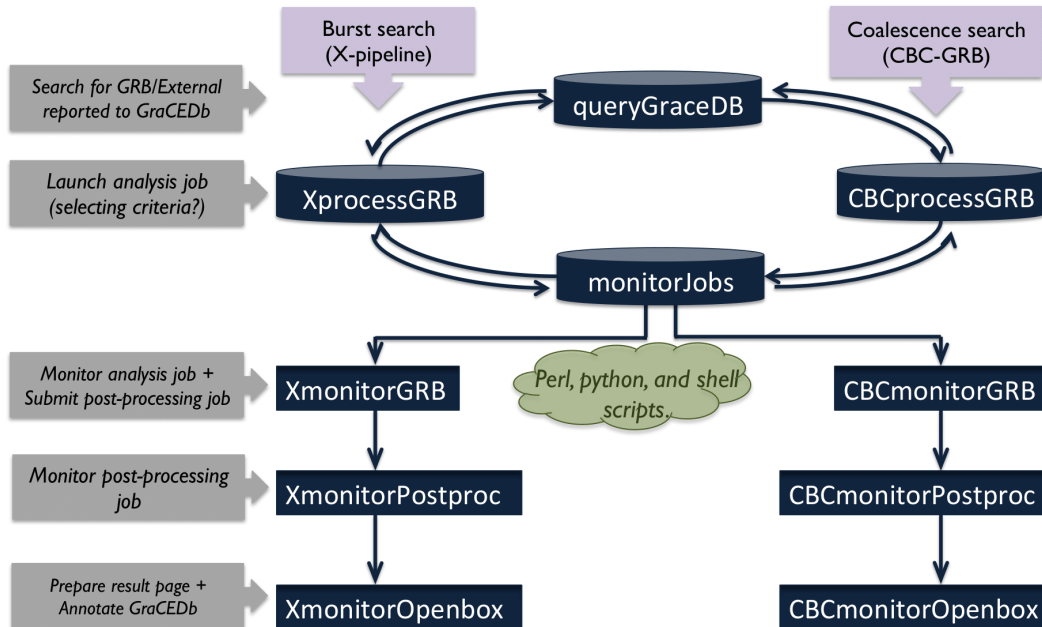


FIGURE 4.14. Schematic of the medium latency GRB codes

on the computing cluster, saving the job info in a text file. Can be configured to automatically send an email to an analyst and add a log message to GraceDB indicating X-pipeline has been launched.

- `monitorJobs` is a parent script that periodically calls the other monitoring scripts.
- `XmonitorGRB` checks the status of the compute jobs, re-launching jobs that may fail from spurious errors. When the X-pipeline analysis job completes, this script will launch the post-processing job and save its info. Can be configured to automatically send an email to an analyst and add a log

message to GraceDB indicating X-pipeline trigger generation has finished and post-processing has begun.

- `XmonitorPostproc` checks the status of the post-processing jobs that tune the X-pipeline analysis and create a human readable webpage showing the “closed box” results as described earlier in this chapter. Also, it launches the “open box” jobs that will have the final results of the analysis. Can be configured to automatically send an email to an analyst and add a log message to GraceDB indicating X-pipeline closed box results are available.
- `XmonitorOpenbox` monitors the status of the open box jobs, re-launching when necessary, and saves the location when results are available. Will send an email and annotate GraceDB with the final results of the pipeline: including a json file with the false alarm probability associated with any candidate GW event that may be present.

There are corresponding scripts for the PyGRB search pipeline as well, although they have been combined into a single python script called `CBC_Pipeline.py`. The medium latency PyGRB search is similar to the X-pipeline version, but has some unique considerations such as choosing a suitable waveform template bank for the search [95].

In order to run the medium latency GRB search, there is a particular directory structure that must be set up, with named files in certain locations that must be present. A script to set up a new run has been created called `make_combined_dir.sh` which can be called on the command line with the name of a new run (e.g. O4) as an argument. This code is intended to be used on the LIGO computing cluster located at Caltech and has not been tested in other

environments. Parameter files that tell the program, for example, which location to find current GW data must also be updated. The main parameter file that needs to be updated is `exttrig_params.pl`, although the default X-pipeline ini file should also be verified for any new data collection run. In order to actually launch the search, each perl script can be launched with the `nohup` command, but for convenience a script called `run_processor.sh` is included in the repository that can be run without any arguments.

During O3 over 60 GRBs were followed up with X-Pipeline in this medium latency configuration, although it was not fully reviewed and did not upload to the public-facing version of GraceDB. I led a detailed technical review of these codes during O3. For the review, some fake GRB events were uploaded to GraceDB and X-pipeline was launched in order to verify the behavior of the pipeline. Those fake GRB analyses used real interferometer data and provide a realistic example showing the latency that can be expected through this procedure, which will depend the amount of computing resources available to the search at the time of the GRB. Figure 4.15 shows a screenshot of a webpage containing the medium latency GRB search results after the fake bursts were analyzed. Final X-pipeline results were available hours after the burst which show that this approach can be useful for providing astronomers with more information in future runs on a reasonable timescale.

Burst/CBC O3_lasttest Online GRB Search

GraceDB GRB	Satellite	Trigger time and duration			Coordinates			Pipeline	IFO in science	ID	Trigger generation job				Post-processing job			
		UT	GPS	Trig_Dur (sec)	R.A. (deg)	Dec (deg)	Err (deg)				Latency (min)	Run time	Status	Rescue #	ID	Run time	Status	Result
S264323	Fake_Fermi	2020-02-25, 06:36:47	1266647825	0.016	2.000	-2.000	4.317	X-pipeline	H1L1	142051208	28.85	0+01:44:59	PROCESSED	001	142052032	0+02:49:57	PROCESSED	OPEN
								PyGRB+cohPTF	H1L1	142066070	718.38	0+07:43:02	PROCESSED	000	--	--	CLOSED_BOX	OPEN_BOX
S264170	Fake_Fermi	2020-02-24, 20:52:51	1266612789	0.016	1.000	-1.000	4.317	X-pipeline	H1V1	142022864	25.27	0+03:27:40	PROCESSED	000	142039451	0+00:50:03	PROCESSED	OPEN
								PyGRB+cohPTF	H1V1	142023743	27.27	0+04:20:02	PROCESSED	000	--	--	CLOSED_BOX	OPEN_BOX

Contact: jordan.palamos@ligo.org

FIGURE 4.15. Screenshot of medium latency test results.

While the GRB alerts were fake, the X-pipeline analyses used real data simulating a real GRB alert. The latency of a few hours from GRB alert to having results available can be expected in general for the X-pipeline medium latency search.

CHAPTER V

PHYSICAL ENVIRONMENT MONITORING

As mentioned in previous chapters, the effect of GWs at the earth from even the strongest sources is minuscule and the detection of GW signals relies on a thorough understanding of the noise processes influencing the detectors. The noise sources impacting the Advanced LIGO and Virgo detectors include quantum sensing noise, seismic noise, suspension thermal noise, mirror coating thermal noise, and gravity gradient noise [96]. As mentioned in Chapter II, these are the instrumental noise sources set the fundamental limits on detector sensitivity. However, there also exist transient noise events, for example coming from anthropogenic sources, weather, equipment malfunctions that impact the interferometers. Therefore, many sensors are deployed around the interferometers to monitor instrument behavior and environmental conditions responsible for these types of noise. While transient noise events are generally accounted for in GW searches using the time-slide method described in Chapter IV, some types of environmental events (such as large lightning strikes, for example) could create correlated noise that is not accounted for in that type of analysis. This chapter describes work completed during the course of my PhD related to the Physical Environment Monitoring (PEM) system which is designed to measure any disturbances in the physical environment that may affect the interferometers. Studying how environmental signals couple into the gravitational wave channel, in order to both validate gravitational wave detections and to increase the sensitivity of the detectors, is a vital part of GW astronomy that has enabled the scientific discoveries discussed in previous chapters. This chapter starts by describing

installation of the PEM system, goes on to discuss a new RF scanner I developed for PEM, and provide some examples of how PEM can identify and remove real noise sources from DARM and increase our confidence in real signals.

5.1. PEM system overview and O1 installation

The system relies on a network of sensors of various types. Accelerometers, seismometers, microphones, magnetometers, and other types of sensors are spread out around critical parts of the detectors. The fundamental requirement for the PEM network is that it must be more sensitive to environmental signals than the gravitational wave detector is to those environmental signals. To achieve this, PEM sensors must be spread out around the observatory and specifically at locations where environmental signals are likely to couple into the gravitational wave detector: Figure 5.1 shows a map of the LIGO Hanford observatory with the location of PEM sensors overlaid. To characterize the response of the PEM network and the coupling of environmental signals to DARM, injection studies are performed with deliberately generated environmental disturbances. The amplitude of the injected signal is compared between a PEM sensor and DARM: the relative signal strength is known as the coupling factor. Typically, these injections need to be much larger than the ambient noise in order to show up in DARM and the injections only take place during non-observational time stretches. This coupling factor is a useful metric to track for vetting gravitational wave detections and identifying unusually high couplings that should be reduced. A more complete description of the PEM system can be found in [97] for the S6 era and updated in [98] for the advanced detector era.

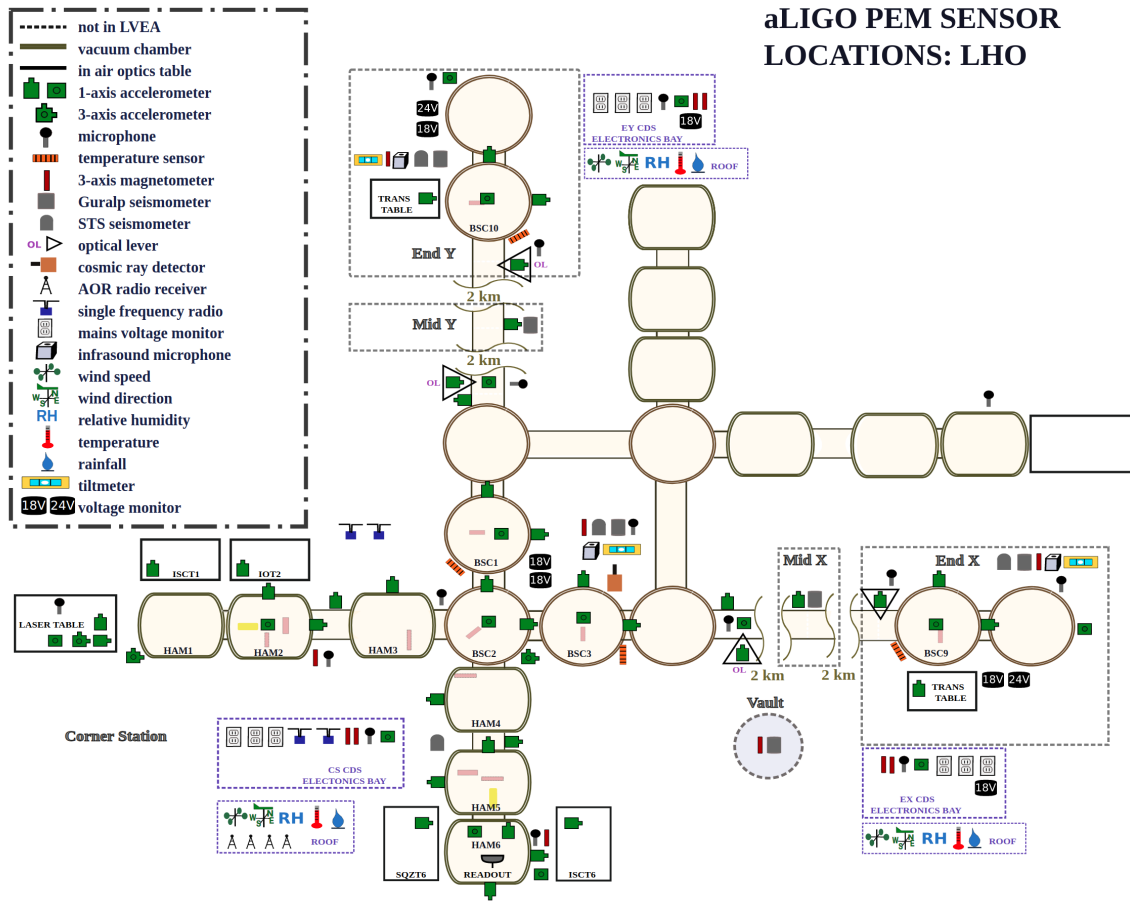


FIGURE 5.1. Map showing the location of physical environment monitor sensors at the Hanford observatory. Accessed from <http://pem.ligo.org/>

Across multiple trips to LIGO-Hanford during the course of this PhD, I assisted a talented team of scientists, engineers, and students responsible for the PEM system. At various times I participated in the installation and calibration of all types of PEM sensors, as well as diagnosing issues that could arise with sensors; carrying out some injection campaigns described above; and creating documentation of the system. Figure 5.2 shows the installation of an PEM accelerometer on a vacuum chamber of the type used to house the LIGO test masses. Here, will focus on a particular type of ambient signal, one that I spent

the most time on, as an example of the kind of work that goes into PEM: radio frequency signals.



FIGURE 5.2. The author installing an accelerometer on a vacuum chamber at LIGO-Hanford.

During initial LIGO environmental RF fields could couple into the modulation frequencies used to control the interferometer and thereby appear in the DARM signal. This was more likely due to the method used to readout the GW signal used the initial detectors. The homodyne DC-readout technique used in Advanced LIGO [99] is less sensitive to RF noise. Still, the aLIGO PEM network records narrow-band radio signals around specific frequencies used for interferometer sensing and control. For example, RF phase modulation is impressed on the laser beam at 9 MHz (equivalent to the FSR of the input mode cleaner) and 45 MHz which is used for global sensing of the interferometer [42]. Therefore, the PEM system includes $\lambda/2$ antennae demodulated at 9 MHz and 45 MHz, as well as AOR radio receivers that can be tuned for various frequencies.

These narrow-band antennae are half-wave dipoles that have been cut out of the correct length of wire: 15.9 m and 3.2 m lengths for receiving frequencies of 9 MHz and 45 MHz respectively. The site for mounting these antenna were chosen to near potential areas where RF signals could couple into the interferometer though away from heavily trafficked areas. This required mounting the antennae several meters up on the walls of the building using ladders and strings. The antennae were fed with coaxial cable to the electronics bay, where the signal was demodulated with a local oscillator and amplified before being read into the audio band aLIGO DAQ system.

Injected signals were created with a different antenna and amplifier from a building on the observatory site many wavelengths away, in the far field, to measure coupling between the environmental RF signals and the detector output. Radio signals at various frequencies were injected while the interferometer was locked and the DARM signal was checked for evidence of coupling [100]. The signal amplitude was limited by the amplifier power available, and for most frequencies there was no observable coupling, however at the 45 MHz modulation frequency a signal did appear in DARM when the injected signal was about 3 orders of magnitude above background. Figure 5.3 shows PEM radio receiver signals and DARM at the time of this injection, which appears around 1050 Hz since all signals were demodulated at 45 MHz and recorded with the audio-band electronics used in LIGO. From this injection we can say that at 45 MHz a radio signal needs to be 200 times higher than ambient background in the auxiliary channel in order to produce a signal with SNR of 1 in DARM. Injections such as these are usually carried out before and after each observation run, for many different signal types, in order to have an

accurate picture of environmental couplings that may have changed over the course of a run.

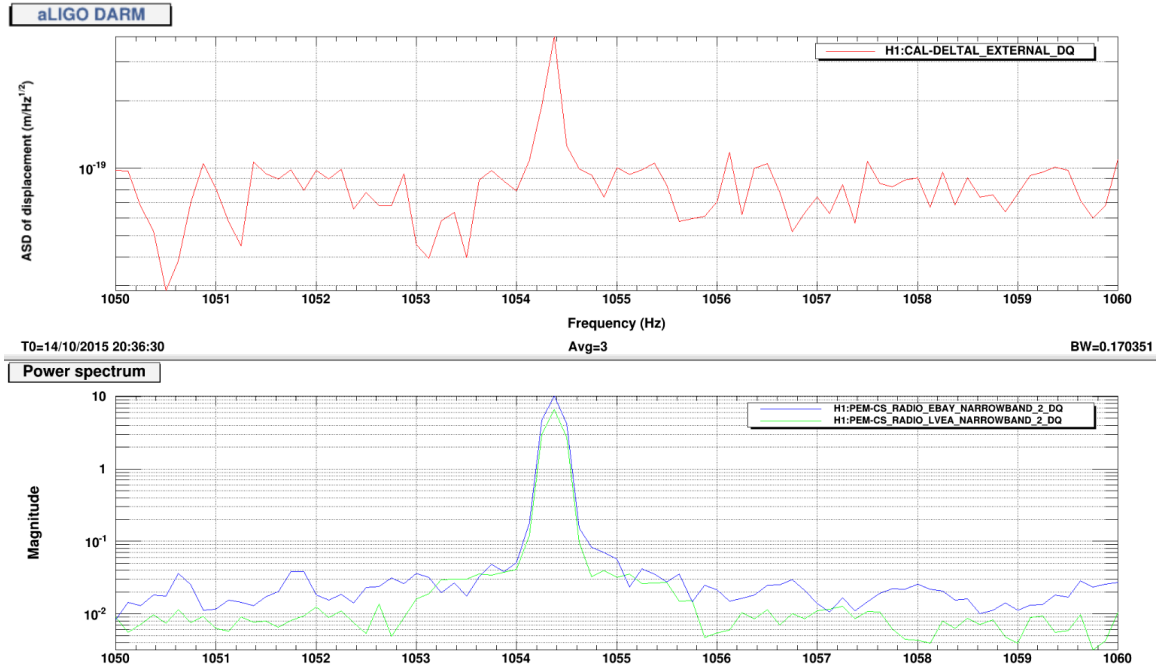


FIGURE 5.3. PEM injection at 45 MHz.

The top panel shows the calibrated DARM ASD in units of meters per $\text{Hz}^{1/2}$. The bottom panel shows the PEM 45 MHz radio signal in arbitrary units: the blue and green traces correspond antennae at different locations near the interferometer. The environmental signal shows up nearly three orders of magnitude above background whereas the DARM signal is about a factor of two.

5.2. Description of the new RF scanner system

A new sensor to be added to the network was developed during the course of this PhD. Although certain radio frequencies, as described above, were monitored during initial LIGO and continue to be, a wide-band monitor was lacking to understand the RF environment around the detector. This new sensor would provide an overview of the whole RF spectrum to give a broader understanding of the ambient RF environment around the site. Additionally, it would be able to

pick up unforeseen large external electromagnetic events that could couple into the detectors.

This new sensor would be able to monitor a large frequency range, from low frequency (LF) to ultra high frequency (UHF) and while also being able to catch short transients on the order of 100 ms, comparable to some short GW transients. Furthermore, it would need to operate reliably without human intervention and fit within budgetary constraints (which excluded most commercially available wideband RF monitoring solutions). The RF-scanner system went through a couple stages of evolution from O1 to the present time in order to better meet the requirements outlined above. The rest of this section will describe the system that was developed for aLIGO and some potential upgrades for future runs.

The antennae used for the RF scanner have stayed constant throughout the three observing runs. They were selected to provide adequate omnidirectional wideband sensitivity while balancing some practical considerations: the antennae needed to fit on the existing roof weather station, be weather/wind proof, and fit within budgetary constraints. Three commercially available surveillance and monitoring antennae were procured from RADIXON [101]: one active “whip” antenna (model number AX-81SM for the LF-HF band) and two passive “discone” antennae (AX-71C and AX-24B for the VHF-UHF and UHF-SHF bands respectively). During testing and with injection studies it was determined that the middle band AX-71C, which had the largest physical footprint of over 1.5 m in height, was not worth the added complexity of combining three antennae and installation of a large antenna. The AX-81SM and AX-24B antenna were installed on the roof of the LIGO-Hanford observatory in Fall 2015 and have remained in place since. Both antennae are connected to approximately 100 ft long coaxial

cables (type LMR-195) running to the interior of the laboratory, through surge arrestors at the building entry point. The active AX-81SM antenna is powered with a 12 volt DC power injector and includes a 250 uH common mode choke on the feed line. The signal from both antennae are combined at the receiver, which has been updated between O2 and O3. A schematic of the RF scanner system as installed at the LIGO-Hanford observatory is shown in figure 5.4 and table 5.1 lists necessary equipment.

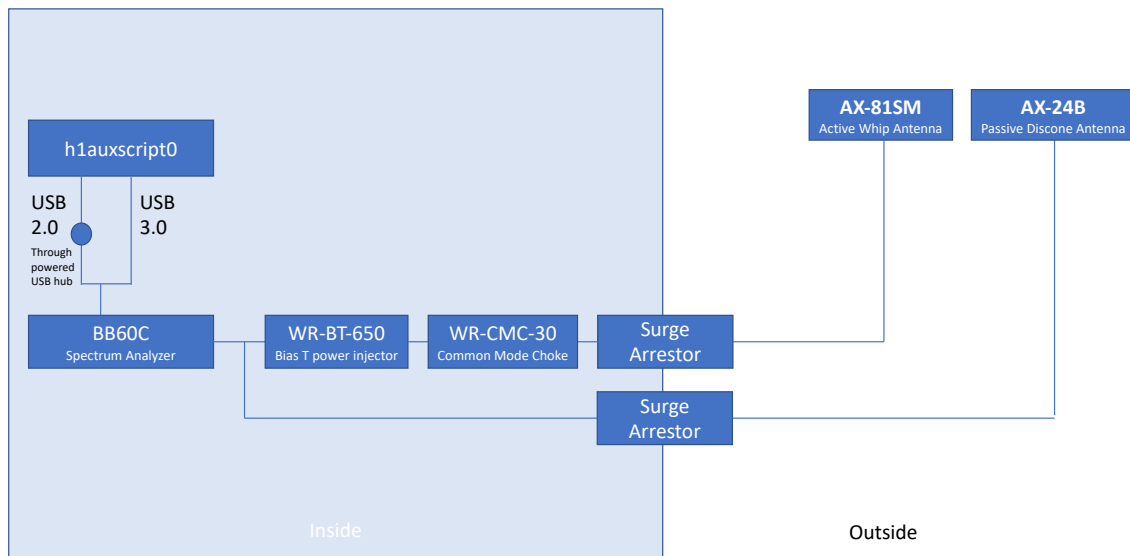


FIGURE 5.4. Block diagram of the RF scanner system.

Shown is the model number for each part of the system in place at Hanford during O3. h1auxscript0 is the name of the rack mounted computer that controls the system.

5.2.1. O1-O2 Radio Receiver

During O1 and O2 the RF scanner receiver relied on a standard laboratory-grade spectrum analyzer¹. The spectrum analyzer was connected to an MS

¹Rohde & Schwarz model FSC3

TABLE 5.1. Hardware used in the RF scanner system.

Equipment	Manufacturer	Use
Rack mounted computer	Any site standard machine running Linux OS	Running code to control the analyzer and process data
BB60c spectrum analyzer	Signal Hound	Acquiring measurements
Active LF-HF antenna	RADIXON	Antenna with good wideband response
AX-24B	RADIXON	Antenna for coverage above 1 GHz
WR-BT-650 power injector	WiNRADiO	Inline power injector for active antenna
WR-CMC-30 common mode choke	WiNRADiO	Filtering common mode noise
Assorted low-loss cables and connectors	any	

windows based computer (a laptop in O1 and a rack mounted unit in O2) running a MATLAB program. The MATLAB program would automatically set the analyzer's sweep parameters, acquire RF spectrum measurements, and stitch the spectrum data into spectrogram-style plots for saving. These sweep parameters were chosen to balance the competing goals of covering a wide swath of the RF spectrum, while still being sensitive to short duration and narrow-band signals. Since the spectrum analyzer could save a static number, 631, data points per sweep: the frequency spectrum could be broken up into segments for increased frequency resolution, especially at lower parts of the frequency spectrum. However, this came at the cost missing short duration signals in one part of the frequency spectrum when measurements were being collected in the other. The typical monitoring configuration had three frequency bands: 9 kHz to 1 MHz, 1 MHz to

200 MHz, and 200 MHz to 3 GHz—and it took approximately 1 second to sweep through all bands. In this configuration, short duration signals could be missed, although the system was able to recover many injected and ambient signal types.

As an example of the types of signals that the system can monitor: figure 5.5 shows spectrum measurements from August 2016 of the frequency band used by cellular communications. In order to see if the RF scanner could pick up cellular activity on site, these measurements were taken while operating different cellular devices known to be used at the site. Comparing the measured spectra with the federal spectrum allocation rules [102] reveals the sources of peaks. Around 600 MHz there are broadcast television signals, and above that at 700 MHz and 800 MHz there are cellular phone signals. The specific cell phones that were intentionally used during the time that these data were collected used the 1700 MHz and 1900 MHz cellular bands. These show up as peaks in the spectrum indicating that the RF scanner is able to pick up cellular phone use on the site: in addition to the rest of the anthropogenic RF background such as TV and FM radio signals that are omnipresent.

However, in the O1-O2 configuration, although the receiver was capable of picking up cellular phone signals on the site, it also missed many signals of that type. Since cellular phone signals are digitized and sent in packets with time duration on the order of milliseconds, the spectrum analyzer could often miss these short duration signals when taking a spectrum measurement. The spectrum analyzer belongs to the superheterodyne class (also known as a swept-tuned spectrum analyzer) and it works by mixing the input signal with a local oscillator and displaying the level of the resulting signal. Internally, there is a local oscillator that is swept through the desired frequency band and mixed with the

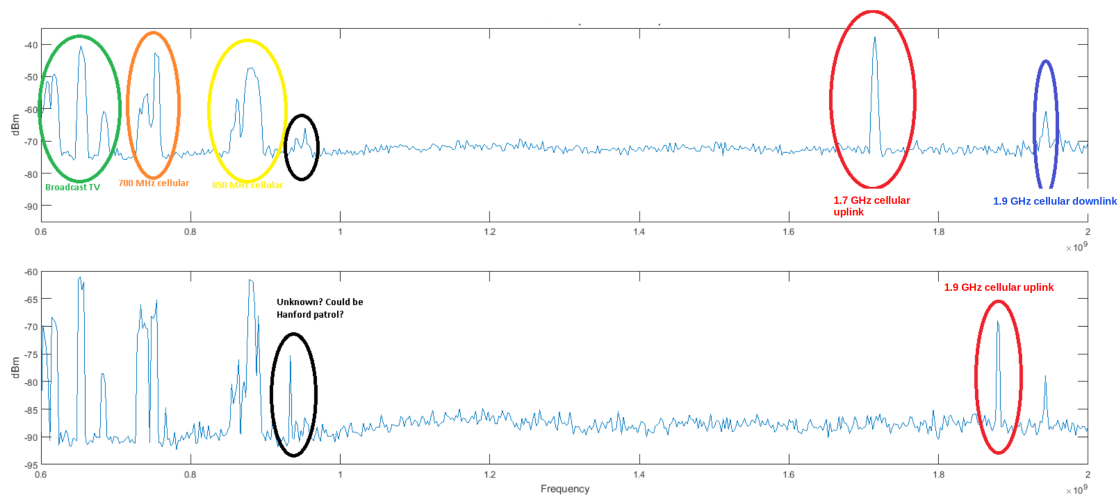


FIGURE 5.5. Annotated spectra of RF activity at the LIGO-Hanford site on August 4, 2016 from 600 MHz to 1 GHz. Shown is frequency in Hz versus dBm at the radio receiver. The top and bottom panels correspond to different cellular phones in use at the time each spectrum was captured. The annotations describe the type of signal corresponding to peaks in the spectrum: peaks circled in green are from broadcast television signals, orange and yellow are from common cellular phone signals (although not the particular phones being used to test the system), the peaks highlighted in black are unknown, and red and blue circles indicate the cellular signals intentionally used during this test.

input signal: the amount of time that takes fundamentally limits the sensitivity of the analyzer to short transient signals. The solution is to switch to a FFT based real-time spectrum analyzer which can sample the whole spectrum over short time periods and catch these transient signals: this is part of the motivation for the system upgrade that occurred before O3. Although it was not possible to thoroughly characterize the response of the RF scanner for short duration signals at these frequencies, there is no evidence for coupling to DARM so this is not high priority. Nevertheless, it may be the subject of future work to verify the reliable reception of short duration cellular signals with the spectrum analyzer—possibly using a high frequency RF amplifier to inject signals.

5.2.2. O1 swept-sine RF injection

Unexpected RF coupling to the detector could occur due to unplanned RF oscillators in commercial electronics used in the interferometer. So-called *whistle* glitches [103] are an example of unknown oscillators polluting the GW data, as was the 650 Hz noise discussed later in this chapter. Therefore, a frequency-swept RF injection was performed to check for strong coupling over a wide swath of the RF spectrum. Whereas previous injection studies have focused on specific frequencies where coupling has been found, such as the 9 Mhz and 45 Mhz modulation frequencies, this injection swept from 9 kHz to 100 MHz to test for unexpected coupling outside of those narrow bands. This swept-sine injection was performed in O1 and used a linear step size of 5 kHz and a step time of 200 ms. Additionally, it served as a test the sensitivity of the new RF scanner.

Over most of the frequency range injected, the RF scanner picked up at a level of at least 20 db (Figure 5.6). There were times that it dipped below that, notably at the extreme high and low ends of the frequency range where the background was higher. Loud persistent background lines could mask the injection at certain points, such as in the FM radio band.

Some parts of this injection were also picked by the narrowband antennae of the PEM system as it swept through their bands. The injection would appear as a short 200 ms sine wave at a frequency corresponding to the difference between the PEM antennae demodulation frequency and the instantaneous injection frequency.

Most importantly, the gravitational wave channel was checked for any unexpected signals that could correlate with this injection. We checked for short 200 ms signals around known specific frequencies, and also for an overall increase in glitches during this hour. No evidence was found for strong coupling between the

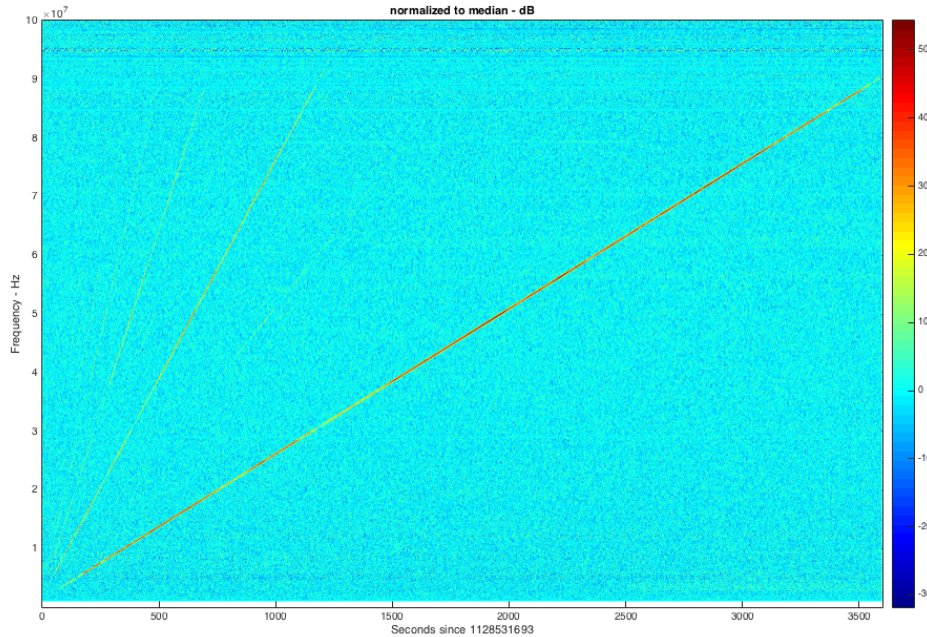


FIGURE 5.6. Swept sine RF injection. Time versus frequency plot of spectral data from the radio receiver. The start time is given in GPS time and corresponds to Oct 10 17:01:16 UTC. The color axis indicates power measured at the RF receiver in dB, normalized to the median.

DARM signal and environmental RF signals. For the band of the sweep we would have to see an SNR of at least 100 in the RF scanner before anything shows up in DARM.

5.2.3. O3 Radio Receiver

For O3 the spectrum analyzer in the RF scanner was switched for an FFT based spectrum analyzer. The upgrade was intended to increase system's sensitivity to short duration signals, as well as eliminate gaps in coverage when saving data that sometimes occurred with the original analyzer. The new spectrum analyzer, a Signal Hound BB60c [104], is a 9 kHz to 6 GHz Spectrum Analyzer and RF Recorder with an instantaneous bandwidth of 27 MHz, and sweep speeds of 24

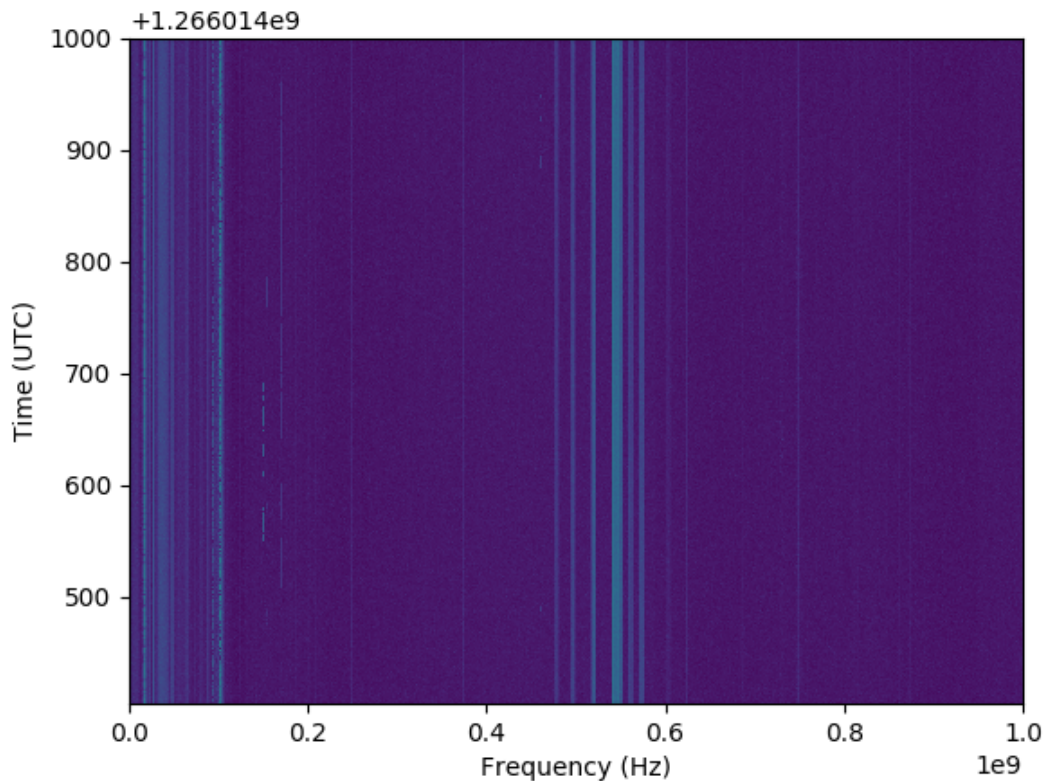


FIGURE 5.7. RF spectrum from the system used for the O3 run. Frequency in Hz versus time in seconds. The time axis spans 10 minutes and the start time corresponds to February 17, 2020 at 22:40:00 UTC. The frequency spans from DC to 1 GHz. Prominent steady lines in the spectrum correspond to things like FM radio and TV broadcasts.

GHz/sec. Furthermore, the analyzer is compatible with computers running the Linux operating system and the API it was shipped with is better suited to develop custom applications with standard tools such as python. This will hopefully lead to better integration with existing computing infrastructure at the LIGO lab and a more robust system. Python routines have been developed that automatically capture spectrum measurements and save the data to spectrogram plots, which are automatically transferred to the LIGO-Hanford computing cluster. In fact, the spectrograms produced by the new system (see example in Figure 5.7) are now

available promptly on the PEM website, <http://pem.ligo.org/>, and updated every ten minutes.

The RF scanner software can be found in a git repository located at https://git.ligo.org/jordan.palamos/rf_scanner². In addition to the C libraries that take care of the low-level communication between the computer and the spectrum analyzer, the repository contains two python scripts:

- `bb_api.py` contains the API to interact with the C library, needs have the correct path to the linked library `libbb_api.so` defined. To use the API other python programs need to import this using: `from bb_api import *`.
- `rf_sweep.py` contains custom python scripts that configure the spectrum analyzer settings, make spectrum measurements, and plot or save the spectrum data. During normal operation this script is called without arguments: then it connects the spectrum analyzer, collects 10 minutes of spectral data, saves a spectrogram plot and exits.

In order to provide continuous coverage, once everything is properly setup, `rf_sweep.py` can be called every ten minutes using a tool such as cron. During O3, the plots were saved and periodically copied (using cron and rsync) to a public web server linked from pem.ligo.org. Future work could save the raw data instead of just plot images: initial testing showed excessive latency when attempting this leading to gaps in the coverage, although it could be possible with more efficient use of computing resources.

²Valid LIGO.ORG credentials required to view this.

5.3. Glitch identification and mitigation

5.3.1. Example of 650 Hz wandering line

A highly useful application of the PEM system is the ability to investigate a noise source that is actively harmful to a particular gravitational wave search. One good example of the PEM system being used to improve the sensitivity of a particular gravitational wave search occurred with the X-pipeline GRB search during O1. When looking at background of the X-pipeline search during O1, it stood out that around the time of some GRBs there was an excess of events with a peak frequency around 650 Hz. For example, the analysis of off-source data around a burst detected by Swift-BAT on October 16, 2015 [105] showed many GW candidate events clustered around 650 Hz.

Figure 5.8 shows the central frequency versus significance for off-source triggers around the time of this burst revealing an unusual amount of triggers are clustered at 650 Hz. When a GW search pipeline shows previously unknown noise clustered around a specific frequency or time it is often very useful to look for the noise in environmental sensors: as was done with this 650 Hz noise.

Visual inspection of the Hanford detector’s strain channel spectrogram revealed a “wandering line” that appeared in some, but not all, of the lock stretches around this time. This noise was concentrated in a narrow band approximately 5 Hz wide with a peak frequency usually around 650 Hz although the peak could vary up to 100 Hz over the course of a day. Since this unknown noise source occurred in a narrow frequency band it was an obvious target to search for in the data of the PEM system as a candidate for environmental contamination. Out of the PEM channels searched, this wandering spectral line only showed up in the narrow-band

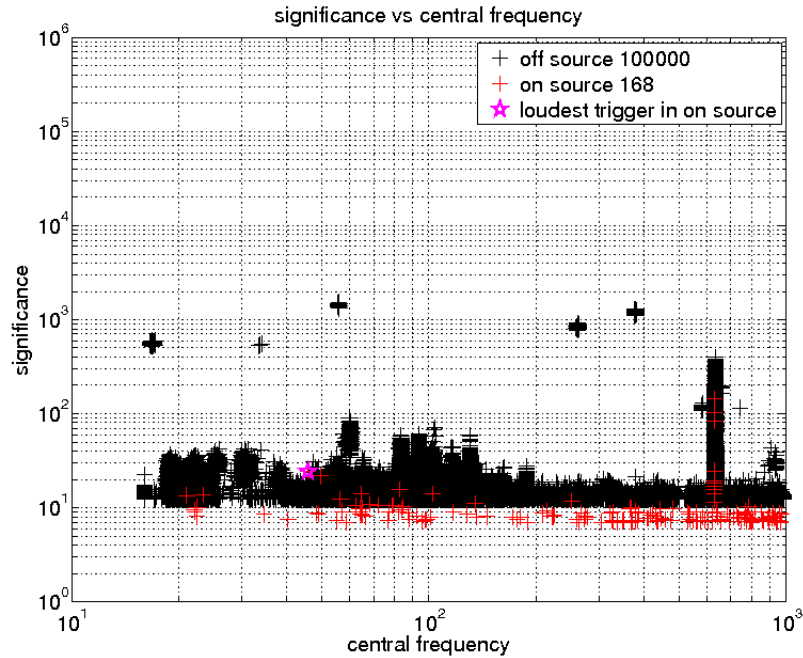


FIGURE 5.8. Frequency versus significance for an X-pipeline analysis showing 650 Hz noise. The red crosses correspond to “dummy on-source” triggers, as described in the previous chapter, and show an abundance of significant triggers with a central frequency of 650 Hz, indicating the possibility of excess instrumental noise at that frequency.

radio receivers. From injection studies, it can be shown that the amplitude of this noise artifact was too low to for it to be environmental RF noise that coupled into the interferometer. More likely, the PEM RF antenna was picking up some unintentional signal generated within the electronics of the interferometer itself.

Another clue came from looking at when in time the noise peak appeared. If the mystery noise appeared in a given lock stretch, it would first appear in the PEM RF channel approximately tens of seconds before the interferometer achieved its nominal low-noise state. In fact, the noise would appear during a specific step of the automated lock acquisition sequence (called the “DC readout transition”). After inspecting a list of changes that occur during this step of

lock acquisition, the only thing that could cause this noise was setting a voltage controlled oscillator (VCO) at a particular frequency. This VCO is used during the lock acquisition of the interferometer, but not during low-noise data collection. However, when the VCO was no longer needed it was left at either 78.7873 MHz or 78.7944 MHz. During the lock stretches where the VCO was left at 78.7873 MHz, the 650 Hz noise would appear in the strain channel. The signal from this VCO was presumably beating against some other RF signal associated with the interferometer. In order to fix this noise, we set the VCO to a much different set value when not in use. After making this simple change the 650 Hz noise never returned and searches for GW with X-pipeline had an increased sensitivity.

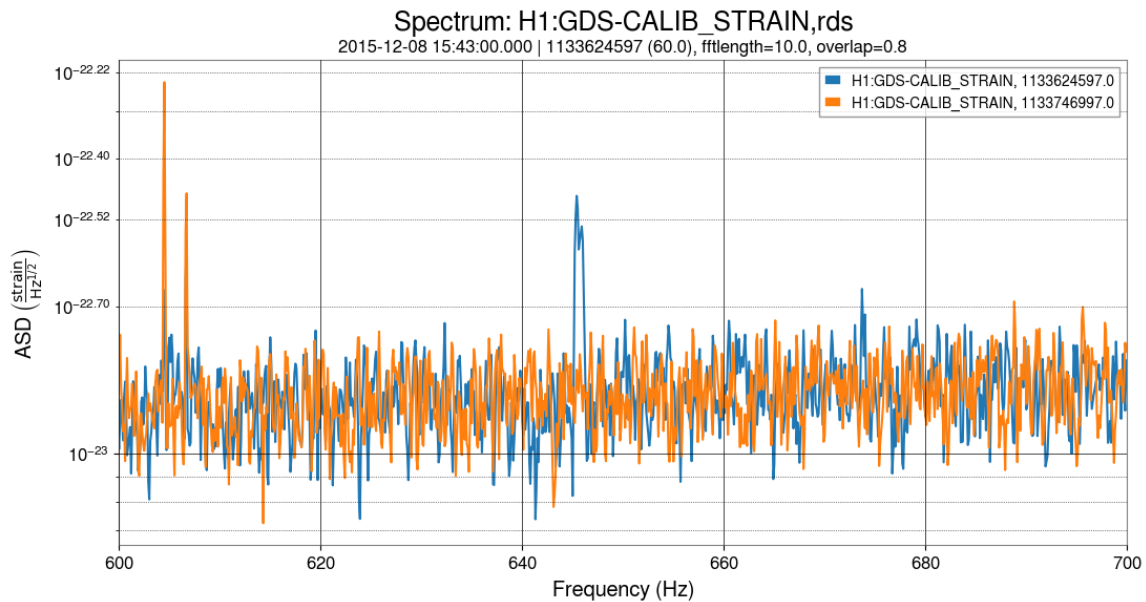


FIGURE 5.9. aLIGO strain spectrum before and after 650 Hz line mitigation. The blue trace shows the spectrum before the fix, and has a peak near 650 Hz and that sticks up above the orange trace.

5.4. PEM event validation

Another important use for the PEM system is to validate candidate GW events. During the era of the first GW detections, the quantitative procedure for vetting GW events using PEM data had to be developed, an important step in the early days of gravitational wave astronomy. As a member of the team that developed these early procedures, I ran software to generate time-frequency image representations of data from PEM sensors, visually inspected these images, and quantitatively estimated the degree to which environmental disturbances could contribute to the DARM signal at the time of a GW event. Although these methods are actively under development and the procedure is mostly automated by now, this section will describe how PEM validation was done during O1 using the signal of GW151226 as an illustrative example. PEM *vetting* reports are publicly available for GW150914 [11] and GW170817 [106], which contain no environmental signals cast doubt on the authenticity of those important events.

The first step to validate a GW detection candidate from the PEM perspective is—after verifying all sufficient sensors were recording high quality data—to search data from all environmental sensors for excess power during the time of the candidate event. The most important check (which has now been automated) was to visually inspect time-frequency plots of the sensor data to see if any environmental signals overlap with the GW event. This is done using an *omega-scan* [107], which are widely used within the LIGO detector characterization group for visualizing glitches in the data. To go along with the primary visual inspection, a quantitative procedure was developed that relied on a signal-to-noise ratio (SNR) from the omega-scan pipeline.

An omega-scan returns the SNR of a signal with arbitrary morphology that may be present in the data in addition to providing a visual time-frequency representation of the data. It works by projecting the data onto a basis of sine-Gaussians and searches of a range of quality-factor (Q) values, picking the time, frequency, and Q which has the most energy relative to white noise. Although it was originally developed to search for un-modelled gravitational wave bursts, for this application the omega pipeline is run over all PEM channels at the time of an GW event to give us the SNR of transient environmental signals during that time. In addition to the time interval, the frequency band is restricted to the band of the GW signal and Q range is restricted to a range that makes the GW signal visible in the omega time-frequency plot. Figure 5.10 shows the omega spectrogram at the time of GW151226, with Hanford DARM signal on the right and the most significant PEM channel on the left.

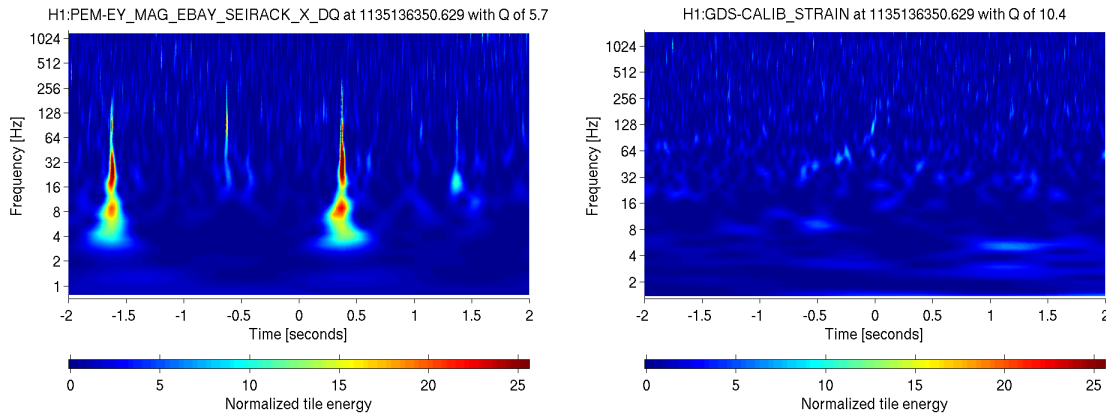


FIGURE 5.10. Omegascan of DARM and the most significant PEM channel during GW151226. Shown on the left is the omegascan of a magnetometer located at an electronics rack at the ‘end Y’ arm of the interferometer. On the right is the Hanford DARM signal.

For each environmental sensor that has a transient signal that overlaps with the time-frequency path of a GW event, coupling factors that were empirically

derived from injection studies are applied to determine how much SNR would be necessary in the environmental channel to show up in DARM. When possible, injections from different frequency bands are used depending on the frequency of the putative GW signal. The SNR of the DARM signal at the time of the GW event is used to determine how much environmental signal is required if environmental coupling were to explain the DARM signal instead of a real GW. Finally, the ratio between the SNR required and the observed SNR of each environmental channel is calculated, which yields a quantitative metric describing how much larger an environmental signal needs to be for the GW event to be explained by environmental coupling.

For example, in the case of GW151226 the closest environmental signal at Hanford was from a magnetometer (which has a data channel labelled H1:PEM-EY_MAG_EBAY_SEIRACK_X_DQ) located near an electronics rack at the end of the interferometer's Y-arm. The omegascan of the data from that sensor revealed a transient signal with SNR of 7.8 that overlapped with the time-frequency path of the GW event. From the injection studies, it was determined that a signal in the magnetometer channel needs to have an SNR greater than 25 to show up before that magnetic field induces a signal in DARM (this value is for a signal at 600 Hz, near to the top of the GW signal band, and is actually an lower limit since sufficiently large injection amplitudes were not possible at the time). Since the GW signal had a DARM SNR of 5.3, the PEM SNR to explain the DARM signal through magnetic coupling would need to be:

$$\begin{aligned}
 (\text{SNR Required}) &= (\text{measured DARM SNR}) \times (\text{PEM SNR to just show up}) \\
 &= 25 \times 5.3 = 132.6.
 \end{aligned}$$

Since the actual PEM SNR was only 7.8, this means that the magnetic transient signal would need to be at least 17 times bigger to explain away the potential GW event as a magnetic event. Table 5.2 shows this calculation for every environmental channel at Hanford that had a transient signal coinciding with GW151226. The magnetometer in the example above was closest to accounting for the DARM signal based on this analysis, therefore nothing was found to cast doubt on the veracity GW151226. This procedure, which proved to be fairly labor intensive, was done for many GW events during O1 and O2.

TABLE 5.2. Hanford PEM channels triggered during GW151226. SNR refers to the value calculated by the Omega pipeline at time of the GW event. ‘SNR to show’ column uses a measured coupling factor to give the SNR value at which the environmental disturbance starts induce a visible signal in DARM. ‘SNR required’ is how much SNR the PEM channel needs if environmental coupling from that sensor were to account for the signal in DARM, and the ratio in the last column describes how much bigger the PEM signal would need to be before the DARM signal could be accounted for through environmental coupling.

Channel Name	SNR	SNR to show	SNR required	SNR required / SNR
H1:PEM-CS_MAG_EBAY_LSCRACK_X_DQ	9	100 ^a 50 ^{dt}	265	29
H1:PEM-CS_MAG_EBAY_LSCRACK_Y_DQ	13.6	100 ^a 50 ^{dt}	265	19
H1:PEM-CS_MAG_EBAY_LSCRACK_Z_DQ	6	100 ^a 50 ^{dt}	265	44
H1:PEM-CS_MAG_EBAY_SUSRACK_X_DQ	6.9	100 ^a 50 ^{dt}	265	38
H1:PEM-CS_MAG_EBAY_SUSRACK_Z_DQ	7.1	100 ^a 50 ^{dt}	265	37
H1:PEM-CS_MAG_LVEA_INPUTOPTICS_X_DQ	6.8	200 ^b 60 ^{dt}	318	47
H1:PEM-CS_MAG_LVEA_INPUTOPTICS_Y_DQ	8	200 ^b 60 ^{dt}	318	40
H1:PEM-CS_MAG_LVEA_INPUTOPTICS_Z_DQ	8.1	200 ^b 60 ^{dt}	318	39
H1:PEM-CS_MAG_LVEA_VERTEX_Y_DQ	5.8	300 ^a 60 ^{dt}	318	55
H1:PEM-CS_MAINSMON_EBAY_1_DQ	27.1	5000	26500	978

Table 5.2, continued

Channel Name	SNR	SNR to show	SNR required	SNR required / SNR
H1:PEM-CS_MAINSMON_EBAY_2_DQ	20.1	5000	26500	1318
H1:PEM-CS_MAINSMON_EBAY_3_DQ	24.1	5000	26500	1100
H1:PEM-EX_MAG_EBAY_SEIRACK_Y_DQ	5.9	700 ^c 100 ^{d†}	530	90
H1:PEM-EX_MAG_EBAY_SUSRACK_X_DQ	11.9	700 ^c 100 ^{d†}	530	45
H1:PEM-EX_MAG_EBAY_SUSRACK_Y_DQ	10.5	700 ^c 100 ^{d†}	530	50
H1:PEM-EX_MAG_EBAY_SUSRACK_Z_DQ	12.2	700 ^c 100 ^{d†}	530	43
H1:PEM-EX_MAINSMON_EBAY_1_DQ	9.2	5000	26500	2880
H1:PEM-EX_MAINSMON_EBAY_2_DQ	11.3	5000	26500	2345
H1:PEM-EX_MAINSMON_EBAY_3_DQ	10.4	5000	26500	2548
H1:PEM-EY_MAG_EBAY_SEIRACK_X_DQ	7.8	25 25 ^{d†}	132.5	17
H1:PEM-EY_MAG_EBAY_SEIRACK_Z_DQ	6.8	25 25 ^{d†}	132.5	19
H1:PEM-EY_MAG_EBAY_SUSRACK_Y_DQ	6.6	25 25 ^{d†}	132.5	20
H1:PEM-EY_MAG_EBAY_SUSRACK_Z_DQ	6.8	25 25 ^{d†}	132.5	19
H1:PEM-EY_MAINSMON_EBAY_1_DQ	12.9	5000	26500	2054
H1:PEM-EY_MAINSMON_EBAY_2_DQ	14	5000	26500	1893
H1:PEM-EY_MAINSMON_EBAY_3_DQ	12.8	5000	26500	2070

[†] Coupling factor is an upper limit.

^a Evaluated for a signal at 24 Hz.

^b Evaluated for a signal at 42 Hz.

^c Evaluated for a signal at 350 Hz.

^d Evaluated for a signal at 600 Hz.

5.4.1. GW150914 global environment checks

Since GW signal detection relies on inter-site coincidences, environmental disturbances that travel at the same speed as GWs are of particular interest.

Things such as global-scale electromagnetic disturbances could potentially affect both LIGO sites within the same speed-of-light delay window as GW events. While the primary method for monitoring these types of signals is still the magnetometers and RF receivers of the PEM system at each LIGO site, investigation of electromagnetic data from other observatories has been part of GW event validation during the era of first detections. In O1 and O2 I was responsible for gathering data from external (to LIGO) electromagnetic observatories as a redundant addendum to the PEM event validation. This section will describe the global environment data collection using GW150914 as an example, although similar work was done for other GW events. Long term, however, on-site magnetometers, antennae, and the wide-band RF monitoring system will be relied on exclusively for this type of event validation.

During the epoch of GW150914, which occurred during the engineering run leading up to the official start of O1, the wide-band RF-scanner was not yet fully operational. Additionally, extra precaution was warranted when making the first claim of direct GW detection. Therefore, an extensive campaign of data collection from various other observatories was done to get a complete understanding of the global electromagnetic environment during GW150914. On site magnetometers would be able to pick up any known electromagnetic disturbance loud enough to directly couple into DARM, the presence of an anomalous electromagnetic event occurring during GW150914 certainly warrant further investigation. The types of physical phenomena that one may expect to find include events related to lightning strikes, such as RF tweaks, whistlers, and choruses [108]; Schumann resonances; anthropogenic RF traffic; or solar radio events. These types of signals and their

potential for influencing the GW150914 signal are summarized in the full PEM report for that event [11].

The main type of external observation that was gathered was very low frequency (VLF) radio data: natural RF transients such as whistlers and choruses would generally show up in these bands. Additionally, magnetometer, solar, and ionospheric data are included to get a complete picture of the global EM environment. Table 5.3 summarizes the types data that were collected during this investigation: the full results with arguments against these and other specific environmental sources contributing to GW150914 can be found in the PEM report for that event [11]. Similar investigations have been done for other GW events including GW170817 [106].

The other type of external observation that was collected during the time period of GW150914 as part of the environmental analysis was cosmic ray data. Cosmic rays could conceivably couple to the LIGO detector through momentum transfer at a test mass, or more complicated electric coupling with charged particles: however this has not been observed. The cosmic ray detector installed at the Hanford site has not shown evidence of cosmic-ray coupling so far. Additionally, the curved geometry of the earth makes it impossible for a single cosmic ray primary to affect both LIGO sites simultaneously. Despite this, as a redundant check, cosmic ray observation stations around the world were checked for fluctuations in cosmic ray rates correlated over long distances during the time of GW150914. Cosmic ray data were gathered from the NOvA experiment in Illinois through email communication [109] and electronically from a global network of cosmic ray detectors [110]. The rate of cosmic ray triggers at the NOvA detector was gaussian, and no other detectors showed elevated rates at the time of

GW150914, supporting the conclusion that cosmic ray events did not contribute to the GW signal. Since coupling between cosmic ray showers and DARM has not been observed, and the global investigation for GW150914 did not uncover anything unexpected, this type of investigation is unlikely to become part of the standard PEM validation process for new GW triggers and the on site cosmic ray detector will suffice.

TABLE 5.3. Global electromagnetic observations gathered at the time of GW150814. None of these observations have shown any anomalous electromagnetic events that could have affected the GW data. The full report can be found in [11].

Source	Location	Observations
Victoria Magnetic Observatory	Victoria, BC	Geomagnetic activity
Rosse Solar-Terrestrial Observatory	Offaly, Ireland	Geomagnetic activity, solar radio bursts
Spaceweather Website [111]	Various locations	Various observations incl. solar wind, solar radio, and upper atmospheric measurements
WIND Satellite	L ₁ Lagrange point	Space based radio and plasma wave monitoring up to frequencies of 14 MHz for the E field and 3 kHz for the B field.
Geostationary Operational Environmental Satellite (GOES)	Geosynchronous orbit	Space based magnetometer, X-ray, charged particle, and ultraviolet sensors
IK1QFT VLF Station	Cumiana, Italy	Natural radio below 15 kHz

Table 5.3, *continued*

Source	Location	Observations
Laurentian VLF Station	Ontario, Canada	Natural radio below 15 kHz
Forrest, VA VLF	Forrest, VA	Natural radio below 15 kHz
Moore Observatory	Brownsboro, KY	Ionosphere monitoring at 24 kHz
Learmonth Observatory	Learmonth, Australia	Solar radio activity

CHAPTER VI

CONCLUSION

The past five years have seen the rapid evolution of GW astronomy from an interesting possibility to a flourishing new field of scientific study. GW150914 and GW170817 highlight the plethora of important new discoveries that have been enabled by advanced LIGO and Virgo. As the field of GW astronomy matures, it is sure to enhance our understanding of various topics such as energetic transient astrophysical phenomena such as GRBs and fast radio bursts; the origin of stellar mass and intermediate mass black holes (thus shedding light on the entire field of stellar evolution); and the processes in the interior of core-collapse supernova—just to name a few.

This dissertation has presented the small ways in which I have contributed towards the global effort of gravitational wave astronomy. After reviewing some general background about GWs and GRBs we have presented a search in the O2 data for GW signals associated with GRBs. No signal from from any GRB other than GRB 170817A was recovered with this search. The sample of GRBs was also checked for a population of GW signals below the detection threshold and none was found. Since no signals were found, upper limits were placed on the distance to sources under different models for GW emission from GRBs. The median 90% confidence level exclusion distance for a generic CSG model with central frequency of 100 Hz was determined to be 113 Mpc. While the CSG waveform models do not correspond to an exact prediction for realistic GW emission, they provide a good estimate for the sensitivity of an unmodelled search. An “eyes-wide-open” approach

to GW searches allows the detection of signals even if models do not ultimately match nature.

Special attention was given to the GW170817 signal which was found using the X-pipeline triggered GRB search. A detailed explanation was given of the difference between two published results, and since this was the first triggered GRB search in LIGO data to contain a significant real GW event it therefore provides an interesting test for the methodology behind externally triggered searches (a future search could detect a significant GW signal that was not previously reported by an all-sky search). Finally, a glitch removal feature that was added to X-pipeline and an effort to run X-pipeline in an automated low-latency fashion were both discussed.

Since the detection of GWs relies on the ability to make extremely precise strain measurements in the presence of instrumental noise, it is important to understand the physical environment around LIGO detectors and how environmental noise may couple to the detectors. The interplay between GW searches and detailed knowledge of the detector environment has been discussed and will doubtlessly prove to be an important aspect of gravitational astronomy during the lifetime of the advanced LIGO/Virgo detectors and beyond. My contributions to the effort to characterize the LIGO detectors, especially in regards to environmental noise were described in chapter V. In particular, a description of a new wide-band RF monitor is given and coupling between RF fields at the observatory and the LIGO detector was explored.

It has taken the work of thousands of scientists around the world spread over decades in order to get the field of gravitational wave astronomy to where it is

now—it was an honor to be a part of this effort and will be exciting to see what comes next.

REFERENCES CITED

- [1] Benjamin P Abbott, Richard Abbott, TD Abbott, MR Abernathy, Fausto Acernese, Kendall Ackley, Carl Adams, Thomas Adams, Paolo Addesso, RX Adhikari, et al. Observation of gravitational waves from a binary black hole merger. *Physical review letters*, 116(6):061102, 2016.
- [2] Benjamin P Abbott, Robert Abbott, TD Abbott, F Acernese, K Ackley, C Adams, T Adams, P Addesso, RX Adhikari, VB Adya, et al. Gravitational waves and gamma-rays from a binary neutron star merger: Gw170817 and grb 170817a. *The Astrophysical Journal Letters*, 848(2):L13, 2017.
- [3] Patrick J Sutton, Gareth Jones, Shourov Chatterji, Peter Kalmus, Isabel Leonor, Stephen Poprocki, Jameson Rollins, Antony Searle, Leo Stein, Massimo Tinto, et al. X-pipeline: an analysis package for autonomous gravitational-wave burst searches. *New Journal of Physics*, 12(5):053034, 2010.
- [4] Joshua Abadie, BP Abbott, R Abbott, TD Abbott, M Abernathy, T Accadia, F Acernese, C Adams, RX Adhikari, C Affeldt, et al. Search for gravitational waves associated with gamma-ray bursts during ligo science run 6 and virgo science runs 2 and 3. *The Astrophysical Journal*, 760(1):12, 2012.
- [5] B Abbott, Robert Abbott, Rana Adhikari, Juri Agresti, P Ajith, Bruce Allen, R Amin, SB Anderson, WG Anderson, M Arain, et al. Search for gravitational waves associated with 39 gamma-ray bursts using data from the second, third, and fourth ligo runs. *Physical Review D*, 77(6):062004, 2008.
- [6] Maurice HPM van Putten. Proposed source of gravitational radiation from a torus around a black hole. *Physical review letters*, 87(9):091101, 2001.
- [7] Maurice HPM van Putten, Gyeong Min Lee, Massimo Della Valle, Lorenzo Amati, and Amir Levinson. On the origin of short grbs with extended emission and long grbs without associated sn. *Monthly Notices of the Royal Astronomical Society: Letters*, 444(1):L58–L62, 2014.
- [8] Benjamin P Abbott, R Abbott, TD Abbott, MR Abernathy, F Acernese, K Ackley, C Adams, T Adams, P Addesso, RX Adhikari, et al. Search for gravitational waves associated with gamma-ray bursts during the first advanced ligo observing run and implications for the origin of grb 150906b. *The Astrophysical Journal*, 841(2):89, 2017.
- [9] Benjamin P Abbott, Rich Abbott, TD Abbott, Fausto Acernese, Kendall Ackley, Carl Adams, Thomas Adams, Paolo Addesso, RX Adhikari, VB Adya, et al. Gw170817: observation of gravitational waves from a binary neutron star inspiral. *Physical Review Letters*, 119(16):161101, 2017.

- [10] B.P. Abbott et al. Search for gravitational-wave signals associated with gamma-ray bursts during the second observing run of Advanced LIGO and Advanced Virgo. *Astrophys. J.*, 886:75, 2019. doi: 10.3847/1538-4357/ab4b48.
- [11] Robert Schofield. Pem vetting report for gw150914. <https://dcc.ligo.org/LIGO-T1800505/public>, Dec 2019.
- [12] Albert Einstein. Die feldgleichungen der gravitation. *Sitzung der physikalische-mathematischen Klasse*, 25:844–847, 1915.
- [13] Hermann Bondi. Plane gravitational waves in general relativity. *Nature*, 179 (4569):1072–1073, 1957.
- [14] Odylio Denys Aguiar. Past, present and future of the resonant-mass gravitational wave detectors. *Research in Astronomy and Astrophysics*, 11(1): 1, 2011.
- [15] Joseph H Taylor and Joel M Weisberg. A new test of general relativity-gravitational radiation and the binary pulsar psr 1913+ 16. *The Astrophysical Journal*, 253:908–920, 1982.
- [16] Ron Cowen. Gravitational waves discovery now officially dead. *Nature News*.
- [17] BP Abbott, R Abbott, TD Abbott, S Abraham, F Acernese, K Ackley, C Adams, RX Adhikari, VB Adya, C Affeldt, et al. Gwtc-1: a gravitational-wave transient catalog of compact binary mergers observed by ligo and virgo during the first and second observing runs. *Physical Review X*, 9(3):031040, 2019.
- [18] Charles W. Misner, K.S. Thorne, and J.A. Wheeler. *Gravitation*. W. H. Freeman, San Francisco, 1973. ISBN 978-0-7167-0344-0, 978-0-691-17779-3.
- [19] Sean M Carroll. *Spacetime and geometry*. Cambridge University Press, 2019.
- [20] James B Hartle. *Gravity: An introduction to Einsteins general relativity*. American Association of Physics Teachers, 2003.
- [21] Bernard Schutz. *A first course in general relativity*. Cambridge university press, 2009.
- [22] Bangalore Suryanarayana Sathyaprakash and Bernard F Schutz. Physics, astrophysics and cosmology with gravitational waves. *Living reviews in relativity*, 12(1):2, 2009.
- [23] Jolien DE Creighton and Warren G Anderson. *Gravitational-wave physics and astronomy: An introduction to theory, experiment and data analysis*. John Wiley & Sons, 2012.

- [24] Duncan A Brown. *Searching for gravitational radiation from black hole machos in the galactic halo*. The University of Wisconsin-Milwaukee, 2004.
- [25] Luc Blanchet, Thibault Damour, Bala R Iyer, Clifford M Will, and Alan G Wiseman. Gravitational-radiation damping of compact binary systems to second post-newtonian order. *Physical Review Letters*, 74(18):3515, 1995.
- [26] LIGO Scientific Collaboration, Virgo Collaboration, 1M2H Collaboration, Dark Energy Camera GW-EM Collaboration, DES Collaboration, DLT40 Collaboration, Las Cumbres Observatory Collaboration, VINROUGE Collaboration, MASTER Collaboration, et al. A gravitational-wave standard siren measurement of the hubble constant. *Nature*, 551(7678):85–88, 2017.
- [27] BP Abbott et al. Tests of general relativity with gw150914. *Phys Rev Lett*, 116: 221101, 2016.
- [28] BP Abbott, R Abbott, TD Abbott, S Abraham, F Acernese, K Ackley, C Adams, RX Adhikari, VB Adya, C Affeldt, et al. Tests of general relativity with the binary black hole signals from the ligo-virgo catalog gwtc-1. *Physical Review D*, 100(10):104036, 2019.
- [29] Benjamin P Abbott, Richard Abbott, TD Abbott, F Acernese, K Ackley, C Adams, T Adams, P Addresso, Rana X Adhikari, Vaishali B Adya, et al. Gw170817: Measurements of neutron star radii and equation of state. *Physical review letters*, 121(16):161101, 2018.
- [30] BP Abbott, R Abbott, TD Abbott, S Abraham, F Acernese, K Ackley, C Adams, RX Adhikari, VB Adya, C Affeldt, et al. Binary black hole population properties inferred from the first and second observing runs of advanced ligo and advanced virgo. *The Astrophysical Journal Letters*, 882(2): L24, 2019.
- [31] Chris L Fryer and Kimberly CB New. Gravitational waves from gravitational collapse. *Living Reviews in Relativity*, 14(1):1, 2011.
- [32] Salvatore Capozziello, Mariafelicia De Laurentis, Francesco De Paolis, G Inghossa, and Achille Nucita. Gravitational waves from hyperbolic encounters. *Modern Physics Letters A*, 23(02):99–107, 2008.
- [33] J Abadie, BP Abbott, R Abbott, R Adhikari, P Ajith, B Allen, G Allen, E Amador Ceron, RS Amin, SB Anderson, et al. Search for gravitational waves associated with the august 2006 timing glitch of the vela pulsar. *Physical Review D*, 83(4):042001, 2011.

- [34] J Aasi, J Abadie, BP Abbott, Richard Abbott, T Abbott, MR Abernathy, T Accadia, F Acernese, C Adams, T Adams, et al. Constraints on cosmic strings from the ligo-virgo gravitational-wave detectors. *Physical Review Letters*, 112(13):131101, 2014.
- [35] Patrick J Sutton. A rule of thumb for the detectability of gravitational-wave bursts. *arXiv preprint arXiv:1304.0210*, 2013.
- [36] Patrick R Brady, Teviet Creighton, Curt Cutler, and Bernard F Schutz. Searching for periodic sources with ligo. *Physical Review D*, 57(4):2101, 1998.
- [37] Keith Riles. Recent searches for continuous gravitational waves. *Modern Physics Letters A*, 32(39):1730035, 2017.
- [38] Bruce Allen and Joseph D Romano. Detecting a stochastic background of gravitational radiation: Signal processing strategies and sensitivities. *Physical Review D*, 59(10):102001, 1999.
- [39] BP Abbott, R Abbott, TD Abbott, S Abraham, F Acernese, K Ackley, C Adams, VB Adya, C Affeldt, et al. Search for the isotropic stochastic background using data from advanced ligos second observing run. *Physical Review D*, 100(6):061101, 2019.
- [40] BP Abbott, R Abbott, TD Abbott, S Abraham, F Acernese, K Ackley, C Adams, RX Adhikari, VB Adya, C Affeldt, et al. Directional limits on persistent gravitational waves using data from advanced ligos first two observing runs. *Physical Review D*, 100(6):062001, 2019.
- [41] Rainier Weiss. Quarterly progress report: Electromagnetically coupled broadband gravitational antenna. <https://dcc.ligo.org/LIGO-P720002/public>, 1972.
- [42] Junaid Aasi, BP Abbott, Richard Abbott, Thomas Abbott, MR Abernathy, Kendall Ackley, Carl Adams, Thomas Adams, Paolo Addresso, RX Adhikari, et al. Advanced ligo. *Classical and quantum gravity*, 32(7):074001, 2015.
- [43] Benjamin P Abbott, R Abbott, TD Abbott, MR Abernathy, F Acernese, K Ackley, C Adams, T Adams, P Addresso, RX Adhikari, et al. Gw150914: The advanced ligo detectors in the era of first discoveries. *Physical review letters*, 116(13):131103, 2016.
- [44] Bernard F Schutz. Networks of gravitational wave detectors and three figures of merit. *Classical and Quantum Gravity*, 28(12):125023, 2011.
- [45] Ray W Klebesadel, Ian B Strong, and Roy A Olson. Observations of gamma-ray bursts of cosmic origin. *The Astrophysical Journal*, 182:L85, 1973.

- [46] Gerald J Fishman, Charles A Meegan, Robert B Wilson, Martin N Brock, John M Horack, Chryssa Kouveliotou, Sethanne Howard, William S Paciesas, Michael S Briggs, Geoffrey N Pendleton, et al. The first batse gamma-ray burst catalog. *The Astrophysical Journal Supplement Series*, 92:229–283, 1994.
- [47] Tsvi Piran, Ramesh Narayan, et al. Spectra and light curves of gamma-ray burst afterglows. *The Astrophysical Journal Letters*, 497(1):L17, 1998.
- [48] Re'em Sari, Tsvi Piran, and Jules Halpern. Jets in grbs. *arXiv preprint astro-ph/9903339*, 1999.
- [49] Yi-Ping Qin, Guang-Zhong Xie, Sui-Jian Xue, En-Wei Liang, Xue-Tang Zheng, and Dong-Cheng Mei. The hardness-duration correlation in the two classes of gamma-ray bursts. *Publications of the Astronomical Society of Japan*, 52(5):759–761, 2000.
- [50] D Band, J Matteson, L Ford, B Schaefer, D Palmer, B Teegarden, T Cline, M Briggs, W Paciesas, G Pendleton, et al. Batse observations of gamma-ray burst spectra. i-spectral diversity. *The Astrophysical Journal*, 413:281–292, 1993.
- [51] Tsvi Piran. Gamma-ray bursts and the fireball model. *Physics Reports*, 314(6):575–667, 1999.
- [52] SE Woosley, Ronald G Eastman, and Brian P Schmidt. Gamma-ray bursts and type ic supernova sn 1998bw. *The Astrophysical Journal*, 516(2):788, 1999.
- [53] SE Woosley. Gamma-ray bursts from stellar mass accretion disks around black holes. *The Astrophysical Journal*, 405:273–277, 1993.
- [54] Joshua S Bloom, JX Prochaska, D Pooley, CH Blake, RJ Foley, Saurabh Jha, E Ramirez-Ruiz, J Granot, AV Filippenko, Steinn Sigurdsson, et al. Closing in on a short-hard burst progenitor: constraints from early-time optical imaging and spectroscopy of a possible host galaxy of grb 050509b. *The Astrophysical Journal*, 638(1):354, 2006.
- [55] Edo Berger. Short-duration gamma-ray bursts. *Annual review of Astronomy and Astrophysics*, 52:43–105, 2014.
- [56] Brian D Metzger. Kilonovae. *Living reviews in relativity*, 20(1):3, 2017.
- [57] A Goldstein, P Veres, E Burns, MS Briggs, R Hamburg, D Kocevski, CA Wilson-Hodge, RD Preece, S Poolakkil, OJ Roberts, et al. An ordinary short gamma-ray burst with extraordinary implications: Fermi-gbm detection of grb 170817a. *The Astrophysical Journal Letters*, 848(2):L14, 2017.

- [58] G Ghirlanda, OS Salafia, Z Paragi, M Giroletti, J Yang, B Marcote, J Blanchard, Iván Agudo, T An, MG Bernardini, et al. Compact radio emission indicates a structured jet was produced by a binary neutron star merger. *Science*, 363(6430):968–971, 2019.
- [59] KP Mooley, E Nakar, K Hotokezaka, G Hallinan, A Corsi, DA Frail, A Horesh, T Murphy, E Lenc, DL Kaplan, et al. A mildly relativistic wide-angle outflow in the neutron-star merger event gw170817. *Nature*, 554(7691):207, 2018.
- [60] Eleanora Troja, Hendrik Van Eerten, G Ryan, R Ricci, J Michael Burgess, MH Wieringa, L Piro, SB Cenko, and T Sakamoto. A year in the life of gw 170817: the rise and fall of a structured jet from a binary neutron star merger. *Monthly Notices of the Royal Astronomical Society*, 489(2):1919–1926, 2019.
- [61] Daniel Kasen, Brian Metzger, Jennifer Barnes, Eliot Quataert, and Enrico Ramirez-Ruiz. Origin of the heavy elements in binary neutron-star mergers from a gravitational-wave event. *Nature*, 551(7678):80–84, 2017.
- [62] Hsin-Yu Chen and Daniel E Holz. Gamma-ray-burst beaming and gravitational-wave observations. *Physical review letters*, 111(18):181101, 2013.
- [63] Daniel Williams, James A Clark, Andrew R Williamson, and Ik Siong Heng. Constraints on short, hard gamma-ray burst beaming angles from gravitational wave observations. *The Astrophysical Journal*, 858(2):79, 2018.
- [64] Warren G Anderson, Patrick R Brady, Jolien DE Creighton, and Eanna E Flanagan. Excess power statistic for detection of burst sources of gravitational radiation. *Physical Review D*, 63(4):042003, 2001.
- [65] J Abadie, BP Abbott, R Abbott, T Accadia, F Acernese, R Adhikari, P Ajith, B Allen, G Allen, E Amador Ceron, et al. Search for gravitational-wave inspiral signals associated with short gamma-ray bursts during ligo’s fifth and virgo’s first science run. *The Astrophysical Journal*, 715(2):1453, 2010.
- [66] Michał Was, Patrick J Sutton, Gareth Jones, and Isabel Leonor. Performance of an externally triggered gravitational-wave burst search. *Physical Review D*, 86(2):022003, 2012.
- [67] Michał Was. *Searching for gravitational waves associated with gamma-ray bursts in 2009-2010 LIGO-Virgo data*. PhD thesis, Paris, U. XI, 2011.
- [68] Shourov Chatterji, Albert Lazzarini, Leo Stein, Patrick J Sutton, Antony Searle, and Massimo Tinto. Coherent network analysis technique for discriminating gravitational-wave bursts from instrumental noise. *Physical Review D*, 74(8):082005, 2006.

- [69] Rahul Biswas, Patrick R Brady, Jolien DE Creighton, and Stephen Fairhurst. The loudest event statistic: general formulation, properties and applications. *Classical and Quantum Gravity*, 26(17):175009, 2009.
- [70] Ian W Harry and Stephen Fairhurst. Targeted coherent search for gravitational waves from compact binary coalescences. *Physical Review D*, 83(8):084002, 2011.
- [71] Andrew R Williamson, C Biwer, Stephen Fairhurst, IW Harry, E Macdonald, Duncan Macleod, and Valeriu Predoi. Improved methods for detecting gravitational waves associated with short gamma-ray bursts. *Physical Review D*, 90(12):122004, 2014.
- [72] Amy Lien, Takanori Sakamoto, Scott D Barthelmy, Wayne H Baumgartner, John K Cannizzo, Kevin Chen, Nicholas R Collins, Jay R Cummings, Neil Gehrels, Hans A Krimm, et al. The third swift burst alert telescope gamma-ray burst catalog. *The Astrophysical Journal*, 829(1):7, 2016.
- [73] Swift grb archive. http://swift.gsfc.nasa.gov/archive/grb_table/.
- [74] David Gruber, Adam Goldstein, Victoria Weller von Ahlefeld, P Narayana Bhat, Elisabetta Bissaldi, Michael S Briggs, Dave Byrne, William H Cleveland, Valerie Connaughton, Roland Diehl, et al. The fermi gbm gamma-ray burst spectral catalog: four years of data. *The Astrophysical Journal Supplement Series*, 211(1):12, 2014.
- [75] Andreas Von Kienlin, Charles A Meegan, William S Paciesas, PN Bhat, Elisabetta Bissaldi, Michael S Briggs, J Michael Burgess, David Byrne, Vandiver Chaplin, William Cleveland, et al. The second fermi gbm gamma-ray burst catalog: the first four years. *The Astrophysical Journal Supplement Series*, 211(1):13, 2014.
- [76] P Narayana Bhat, Charles A Meegan, Andreas von Kienlin, William S Paciesas, Michael S Briggs, J Michael Burgess, Eric Burns, Vandiver Chaplin, William H Cleveland, Andrew C Collazzi, et al. The third fermi gbm gamma-ray burst catalog: the first six years. *The Astrophysical Journal Supplement Series*, 223(2):28, 2016.
- [77] K Hurley, T Cline, I Mitrofanov, E Mazets, S Golenetskii, F Frontera, E Montanari, C Guidorzi, and M Feroci. The current performance of the third interplanetary network. In *AIP Conference Proceedings*, volume 662, pages 473–476. American Institute of Physics, 2003.
- [78] Robert R Coyne. *LIGO GRB searches in the aLIGO Era: An Optimized Burst Database and a New Method for Detecting Intermediate-Duration GWs*. PhD thesis, The George Washington University, 2015.

- [79] V Connaughton, MS Briggs, A Goldstein, CA Meegan, WS Paciesas, RD Preece, CA Wilson-Hodge, MH Gibby, J Greiner, D Gruber, et al. Localization of gamma-ray bursts using the fermi gamma-ray burst monitor. *The Astrophysical Journal Supplement Series*, 216(2):32, 2015.
- [80] V Predoi, Kevin Hurley, LIGO Scientific Collaboration, Virgo Collaboration, et al. Search for gravitational waves associated with the interplanetary network short gamma ray bursts. In *Journal of Physics: Conference Series*, volume 363, page 012034. IOP Publishing, 2012.
- [81] J Aasi, BP Abbott, Rich Abbott, Thomas Abbott, Matthew Robert Abernathy, F Acernese, Kendall Ackley, Carl Adams, Thomas Adams, Paolo Addesso, et al. Methods and results of a search for gravitational waves associated with gamma-ray bursts using the geo 600, ligo, and virgo detectors. *Physical Review D*, 89(12):122004, 2014.
- [82] <http://www.cs.wisc.edu/condor/>.
- [83] D. et al. Xu. Gcn circ. 20458. 2017.
- [84] de Ugarte Postigo et al. Gcn circ. 20584. 2017.
- [85] Z. et al. Cano. Gcn circ. 21059. 2017.
- [86] de Ugarte Postigo et al. Gcn circ. 21298. 2017.
- [87] de Ugarte Postigo et al. Gcn circ. 21359. 2017.
- [88] Chris Pankow, Katerina Chatziioannou, Eve A Chase, Tyson B Littenberg, Matthew Evans, Jessica McIver, Neil J Cornish, Carl-Johan Haster, Jonah Kanner, Vivien Raymond, et al. Mitigation of the instrumental noise transient in gravitational-wave data surrounding gw170817. *Physical Review D*, 98(8):084016, 2018.
- [89] Derek Davis, Thomas Massinger, Andrew Lundgren, Jennifer C Driggers, Alex L Urban, and Laura Nuttall. Improving the sensitivity of advanced ligo using noise subtraction. *Classical and Quantum Gravity*, 36(5):055011, 2019.
- [90] LIGO Virgo Collaboration et al. Ligo/virgo public alerts user guide. *URL* <https://emfollow.docs.ligo.org/userguide>, 2020.
- [91] <https://gracedb.ligo.org/>.
- [92] Benjamin P Abbott, R Abbott, TD Abbott, S Abraham, F Acernese, K Ackley, C Adams, RX Adhikari, VB Adya, C Affeldt, et al. Low-latency gravitational-wave alerts for multimessenger astronomy during the second advanced ligo and virgo observing run. *The Astrophysical Journal*, 875(2):161, 2019.

- [93] Peter WA Roming, T Scott Koch, Samantha R Oates, Blair L Porterfield, Amanda J Bayless, Alice A Breeveld, Caryl Gronwall, NPM Kuin, Mat J Page, Massimiliano De Pasquale, et al. A large catalog of homogeneous ultra-violet/optical grb afterglows: Temporal and spectral evolution. *The Astrophysical Journal Supplement Series*, 228(2):13, 2017.
- [94] DA Kann, S Klose, B Zhang, Daniele Malesani, E Nakar, A Pozanenko, AC Wilson, NR Butler, Pall Jakobsson, S Schulze, et al. The afterglows of swift-era gamma-ray bursts. i. comparing pre-swift and swift-era long/soft (type ii) grb optical afterglows. *The Astrophysical Journal*, 720(2):1513, 2010.
- [95] Michael Patel and Ryan Fisher. Generating a template bank for use in medium latency pygrb searches. 2020.
- [96] Benjamin P Abbott, Rich Abbott, Thomas D Abbott, Sheelu Abraham, Fausto Acernese, Kendall Ackley, Carl Adams, Vaishali B Adya, Christoph Affeldt, Michalis Agathos, et al. A guide to ligo–virgo detector noise and extraction of transient gravitational-wave signals. *Classical and Quantum Gravity*, 37(5):055002, 2020.
- [97] A Effler, RMS Schofield, VV Frolov, G González, K Kawabe, JR Smith, J Birch, and R McCarthy. Environmental influences on the ligo gravitational wave detectors during the 6th science run. *Classical and Quantum Gravity*, 32(3):035017, 2015.
- [98] Robert Schofield. aligo pem system upgrade.
<https://dcc.ligo.org/LIGO-T1200221/public>, May 2012.
- [99] Tobin T Fricke, Nicolás D Smith-Lefebvre, Richard Abbott, Rana Adhikari, Katherine L Dooley, Matthew Evans, Peter Fritschel, Valery V Frolov, Keita Kawabe, Jeffrey S Kissel, et al. Dc readout experiment in enhanced ligo. *Classical and Quantum Gravity*, 29(6):065005, 2012.
- [100] Jordan Palamos. Pem injection report - rf coupling.
<https://alog.ligo-wa.caltech.edu/aLOG/index.php?callRep=23252>, 2015.
- [101] <https://www.radixon.com/index.html>.
- [102] <https://www.ntia.doc.gov/files/ntia/publications/2003-allochrt.pdf>.
- [103] Michael Zevin, Scott Coughlin, Sara Bahaadini, Emre Besler, Neda Rohani, Sarah Allen, Miriam Cabero, Kevin Crowston, Aggelos K Katsaggelos, Shane L Larson, et al. Gravity spy: integrating advanced ligo detector characterization, machine learning, and citizen science. *Classical and Quantum Gravity*, 34(6):064003, 2017.

- [104] <https://signalhound.com/>.
- [105] J. R. et al. Cummings. Gen circ. 18421. 2015.
- [106] Robert Schofield. Pem vetting report for gw170817.
<https://dcc.ligo.org/LIGO-T1800508/public>, Dec 2019.
- [107] Shourov Chatterji, Lindy Blackburn, Gregory Martin, and Erik Katsavounidis. Multiresolution techniques for the detection of gravitational-wave bursts. *Classical and Quantum Gravity*, 21(20):S1809, 2004.
- [108] Devendraa Siingh, AK Singh, RP Patel, Rajesh Singh, RP Singh, B Veenadhari, and Madhuparna Mukherjee. Thunderstorms, lightning, sprites and magnetospheric whistler-mode radio waves. *Surveys in geophysics*, 29(6): 499–551, 2008.
- [109] Alec T Habig, Nov 2015. Personal Communication.
- [110] Bartol neutron monitors. <http://www.bartol.udel.edu/gp/neutronm/>.
- [111] <https://spaceweather.com/>.